Dispersion Management and Action Cross Section Quantifications for Three-Photon Microscopy of Cardiac Organoids

Lewis Williamson

Submitted in fulfilment of the requirements for the

Degree of Doctor of Philosophy

School of Physics and Astronomy

College of Science and Engineering

June 2026

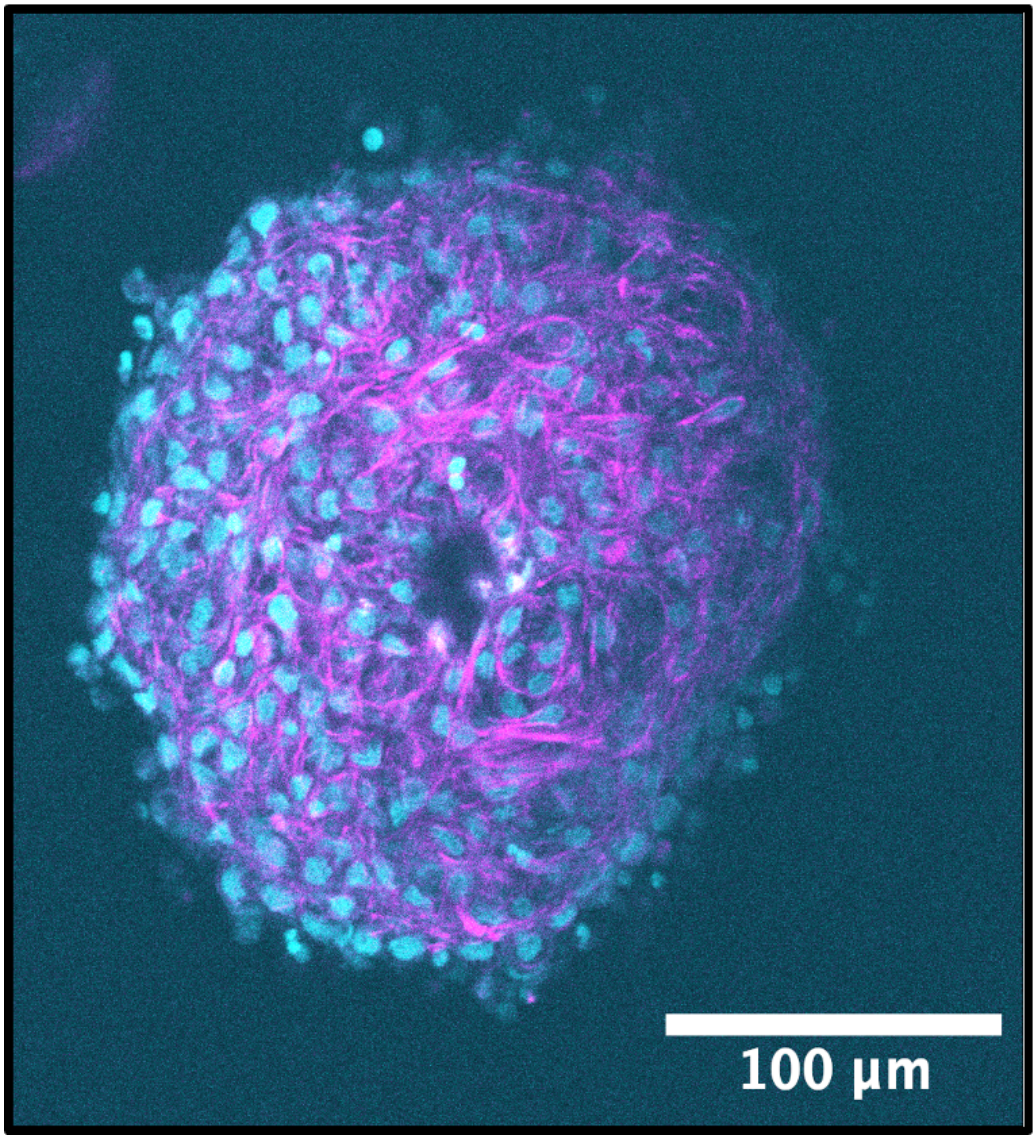

Figure 1: Cleared spheroid with approximately 3000 cells. Imaged with a combination of two and three photon microscopy at 1350nm, Cyan: DAPI stained cell membrane, Magenta: SHG signal from collegian. The structure is imaged to a depth of 260µm throughout the entire FOV of the spheroid.

Abstract

Achieving high-contrast, high-resolution imaging at depth is the principal goal of any multiphoton microscopy system. To advance these capabilities, three-photon microscopy has been developed, exploiting longer excitation wavelengths and three-photon absorption—a higher-order nonlinear excitation mechanism. This approach enables deeper imaging with an improved signal-to-background ratio (SBR) at greater depths. However, the higher-order nonlinearity and longer excitation wavelengths impose constraints on the illumination source, necessitating the use of a laser system capable of producing non-standard wavelengths. Consequently, a pump laser and optical parametric amplifier (OPA) are required to generate infrared wavelengths with short pulse durations, with dispersion compensation provided by a separate pulse compressor.

Within a custom-built two-photon microscope, where a number of highly dispersive elements that significantly affect pulse duration are used. To address this, direct measurement of the pulse duration has been achieved using a novel intensity-only autocorrelator in combination with a custom-built prism compressor. This setup enables precise characterisation of ultrashort pulses at the focal plane of the microscope. Measurements across a range of pre-compensation levels applied via the prism compressor reveal the relationship between dispersion management and temporal pulse compression finding the shortest pulse duration, closely matching the

theoretical limit of our Ti:Sa laser source of 139fs.

A custom-built two- and three-photon microscope has been developed and fully characterised in both temporal and spatial domains. The system achieved a spatial resolution of 0.93, 0.89, and 3.44µm along the X, Y, and Z axes respectively at 1300 nm. Temporal characterisation has also been performed, with dispersion management optimised across a range of suitable wavelengths, and the required level of pre-compensation has been determined. For wavelengths of 1300nm a pulse duration of 49fs has been formed and measured at the focal spot of the microscope, from our OPA. A direct measurement of two and three photon absorption has been taken by increasing the illumination power over a sample, taking the logarithmic of measured intensity and applied power.

Organoids represent an emerging area within biomedical research, offering valuable models for drug testing and holding potential clinical applications in tissue growth and repair. Cardiac and heart organoids were supplied, with the heart organoids comprising a more diverse range of cell types. Both cleared and uncleared samples of each tissue type were examined, with all four imaged to a depth of approximately 500 µm from the cleared samples using our custom multiphoton system. These images provided collaborators with essential insights into the structural composition of the cardiac and heart organoids, informing subsequent culturing methods. Quantitatively, the effective attenuation length (EAL) was calculated for the uncleared cardiac and heart organoids, yielding values of 272 µm and 303.5 µm, respectively.

Using the in-depth characterisation of our system, the efficacies of three fluorescent dyes; Cy5 (two photon absorption), DAPI, and fluorescein (three photon absorption) in producing multiphoton interactions were measured. The action cross section was determined using the technique outlined by LaViollette *et al.* [1]. Employing

custom optical parametric amplifier (OPA) interactions to narrow the spectral bandwidth of our laser source, measurements were conducted within a photon-counting regime. Despite certain errors associated with this regime, quantitative analysis was achieved for all three dyes across the wavelength range of 1150–1350 nm. When compared with the limited published data, our results show comparable two-photon interaction values for Cy5 and fluorescein, along with a novel finding for DAPI within the near-infrared (NIR) wavelength range.

Contributions

The following is a summary of the scientific contribution that is made in each of my chapters.

Chapter 1.5

A novel design for a pulse compressor is introduced here, adapting a design from Durst et.al.

Chapter 2.4

Three photon is an emerging technique in microscopy. Presented here is a home-built three photon setup that employs a novel pulse shaping regime. Detailed also is the technique in which our commercial OPA has been spectrally tuned in both wavelength and spectral bandwidth.

Chapter 3.6

Contributions to the field of cardiac Organoids have been made by imaging cardiac and heart organoids and drawing comparisons between cleared and uncleared variants.

Chapter 4.5

The action cross section of three dyes is shown, providing data for DAPI with three photon wavelengths. This is corroborated with results in two photon absorption in Cy5 and Flourescene at three photon wavelengths, finding them close to published data.

Declaration

I declare that all work described in this Thesis which is not my own is appropriately identified and attributed to the respective authors. Furthermore, any material that has previously been submitted and approved for the award of a degree by this or any other University has been acknowledged.

The work that I present in this thesis is my own with the exception of the following:

1. In Chapter 1.6 my work has been centered around a pre-existing setup created by fellow PGR Giedre Astrauskaite's. My work does not extended to that of the remote focusing setups construction.

2. In Chapter 2.4 I have characterised the three photon microscope that was built with Dr. Ryo Kinegawa and I. The characterisation of the setup was done solely by me.

3. In Chapter 3.6 spheroid and organoid preparation was conducted with help of Godfrey Smiths team in the school of Cardiovascular and metabolic health, particularity Sasha Forbes (PGR). The data showcased here was acquired with the assistance of Ahmed Elnageh (PGR).

4. In Chapter 4.5 This experiment was solely conducted by myself with exception

of the preparation of the dyes which was done with the assistance of Sasha Forbes (PGR).

Acknowledgements

I would like to express my sincere gratitude to my supervisor, Dr Caroline Mullenbroich, for entrusting me with this role and for her guidance and support throughout, which have been invaluable and will continue to serve me well for years to come. I also thank Dr Jonny Taylor, Prof. Andy Harvey, Dr Johannes Courtial, Prof. Matteo Clerici, Dr Leonardo Sacconi, Dr Pedro Miguel Parreira, and Prof. Godfrey Smith for their advice and insights along the way.

I am also deeply grateful to my partner, Ellie, and to my parents and siblings for their continued encouragement and support, which have made my achievements possible. I love you all.

Finally, I would like to thank everyone I met during this journey, including my Fortnite and golfing friends Maik, Andrew, Joel and Conall, as well as the other members of the ICG and my office and lab friends, for the help and the laughs.

This work was supported by UK Research and Innovation (UKRI) under grant number 2813291.

Conference Contributions

Oral Presentations

"Optimisation of 3-photon microscopy for deep imaging in cardiac spheroid"

Microscience Microscopy Congress - Manchester England, July 2025

"Remote Focusing via Dispersion Compensation in a Temporally Focused 2-Photon Microscope"

Photon - Swansea Wales, September 2024

"Spatial and Temporal Methods for Remote Focusing in Multi-Photon Microscopy"

Scottish Universities Physics Alliance Annual Gathering - Glasgow Scotland, May 2024

Poster Presentations

"Imaging Cardiac Organoids with 3-Photon Microscopy"
Glasgow Imaging Network - Glasgow Scotland, April 2025

"Characterisation of a custom-built 3-photon microscope"
Scottish Microscopy Symposium - Glasgow Scotland, November 2024

"Using in-focus autocorrelation to directly measure dispersion-compensation induced focal shift in a temporal focusing setup"
Focus on Microscopy - Genova Italy, April 2024

"Inline Autocorrelation Leads to Direct Measurement of Pulse Duration in the Sample Plane"
Glasgow Imaging Network - Glasgow Scotland, December 2023

"Measuring and Managing Dispersion in Multiphoton Microscopy at the Sample"
Scottish Microscopy Symposium - Dundee Scotland, November 2024 (Prize)

"Measuring and Managing Dispersion in Multi Photon Microscopy"
NOTICE - Glasgow Scotland, April 2023

List of Tables

List of Figures

Contents

1. Introduction

Since multiphoton microscopy can be a *bit* of a pain it is common to offer the research motivation behind it by explaining the improvements over its predecessor the confocal system.

1.1 Confocal Microscopy

Confocal microscopy is a single-photon fluorescence imaging technique in which excitation is achieved through the absorption of a single photon by a fluorophore [2]. Fluorescence emission is generated and collected through the same objective lens used for excitation. Inclusion of a spatial pinhole placed conjugate to the focal plane selectively transmits in-focus fluorescence whilst rejecting out-of-focus signal. This spatial filtering significantly improves optical sectioning capability and image contrast when compared with widefield fluorescence microscopy.

As shown in Figure (1.2) a continuous-wave laser source is focused to a diffraction-limited spot within the sample and raster scanned across the imaging plane to construct an image sequentially point-by-point. The detected fluorescence intensity at each scan position is measured using a sensitive detector, commonly a photomultiplier tube (PMT) [3]. Although confocal microscopy provides high lateral resolution and excellent image contrast in thin or weakly scattering samples, the use of single-

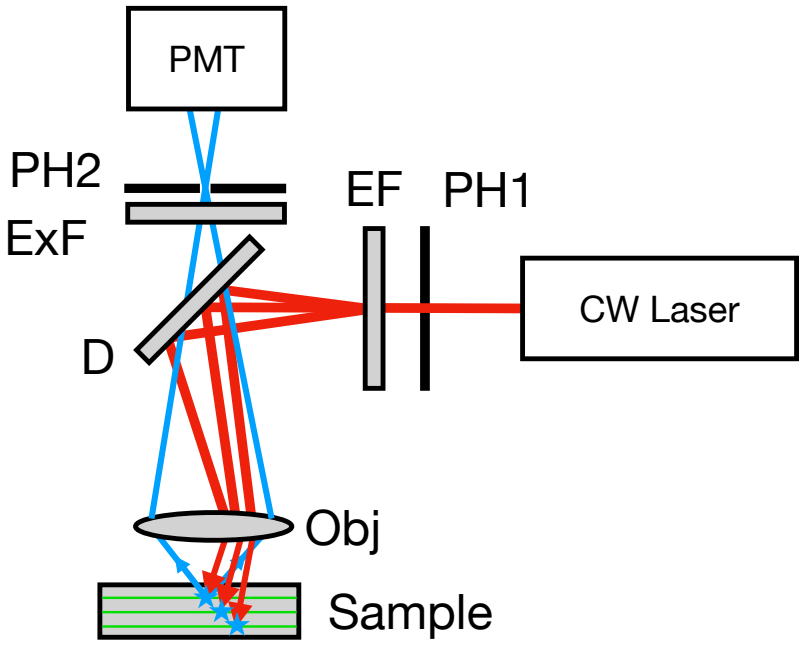

Figure 1.2: Schematic diagram of a confocal microscopy system. A laser is spatially filtered through pin hole 1 (PH1) and directed by a dichroic mirror (D) through the objective lens (Obj) to form a tightly focused excitation spot within the sample. Fluorescence emitted from the focal volume is collected by the same objective, transmitted through the dichroic mirror, and spatially filtered using a confocal pinhole (PH2) before detection by a photomultiplier tube (PMT). The excitation filter (ExF) and emission filter (EF) provide spectral isolation of the excitation and fluorescence signals respectively

photon excitation results in fluorescence generation throughout the excitation cone both above and below the focal plane. Consequently, this technique is associated with increased photobleaching and photodamage outside the imaging region, particularly during prolonged imaging or at elevated excitation powers. In addition, visible excitation wavelengths undergo strong scattering within biological tissue, limiting penetration depth and reducing imaging performance in thick or highly scattering specimens[4, 5].

1.2 Multiphoton Microscopy

1.2.1 Multiphoton Absorption

Multiphoton microscopy overcomes these limitations by confining excitation to the focal volume [6]. Unlike in confocal microscopy, no out-of-focus fluorescence is generated, so pinhole-based rejection is unnecessary. This is achieved through the mechanism of multiphoton absorption, in which two or more photons are absorbed almost simultaneously by the same fluorophore, resulting in the emission of a single photon. Shown in Figure. 1.3, this process can occur through two-photon or three-photon absorption in addition to the single-photon case. Each mechanism excites an electron to a higher energy level, from which it can decay radiatively to produce fluorescence [7]. Generally, the emitted photon is identical regardless of the excitation mechanism. In all cases, the electron undergoes non-radiative relaxation to the lowest vibrational sublevel of the excited state before photon emission.

A distinctive feature of multiphoton excitation is the presence of short-lived *virtual states* that the electron transiently occupies between photon absorption events. These are not true eigenstates of the system and do not correspond to stable solutions of the Schrödinger equation. Instead, they act as bridges that allow the electron to reach a real excited state if a sufficient number of photons arrive within a very short time window [8]. The maximum lifetime of such a virtual state can be estimated from the energy–time uncertainty relation:

$$\Delta t \approx \frac{\hbar}{\Delta E} \tag{1.1}$$

where $\hbar$ is the reduced Planck constant and ΔE is the energy difference between states. This typically corresponds to lifetimes on the order of only a few femtoseconds

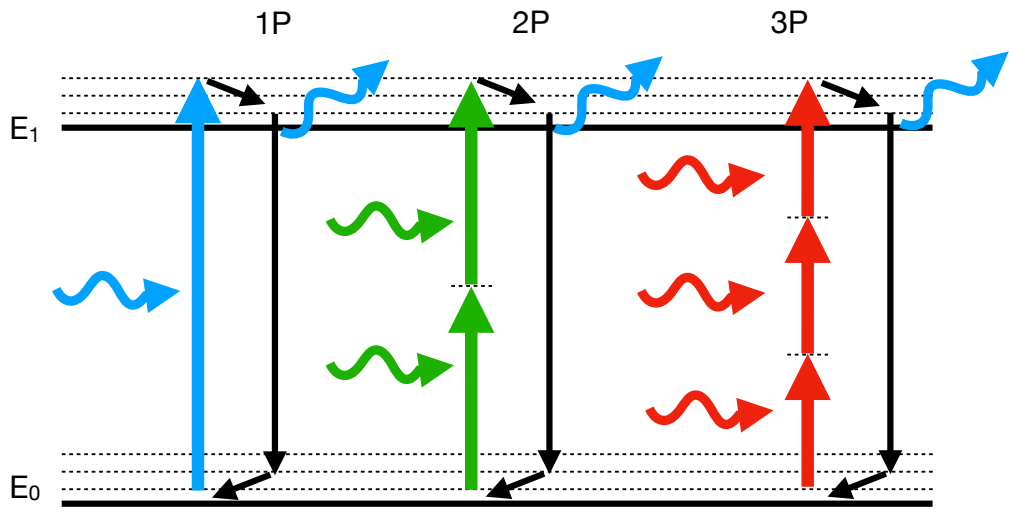

Figure 1.3: Jablonski diagram illustrating single-photon (blue), two-photon (green), and three-photon (red) excitation processes. In each case, absorption promotes the fluorophore from the ground singlet state to an excited electronic state through the simultaneous absorption of one, two, or three photons respectively. Following excitation, rapid non-radiative vibrational relaxation and internal conversion occur prior to radiative decay via fluorescence emission back to the ground state. Multi-photon excitation utilises lower-energy, longer-wavelength photons and requires near-simultaneous photon absorption within the focal volume, resulting in intrinsic optical sectioning and reduced out-of-focus photodamage.

(1–3 fs) [9].

This ultrashort temporal window highlights the requirement for a high photon flux to drive multiphoton absorption. While in principle such densities could be achieved with continuous-wave (CW) lasers, pulsed laser systems are far more efficient. They provide high peak powers while maintaining relatively low average powers, reducing photodamage to the sample, discussed further in section 1.3.

The confinement of excitation to the focal plane is the central advantage of multiphoton microscopy. It enables intrinsic optical sectioning, reduces photodamage outside the focal volume, and permits imaging deeper within scattering tissue com-

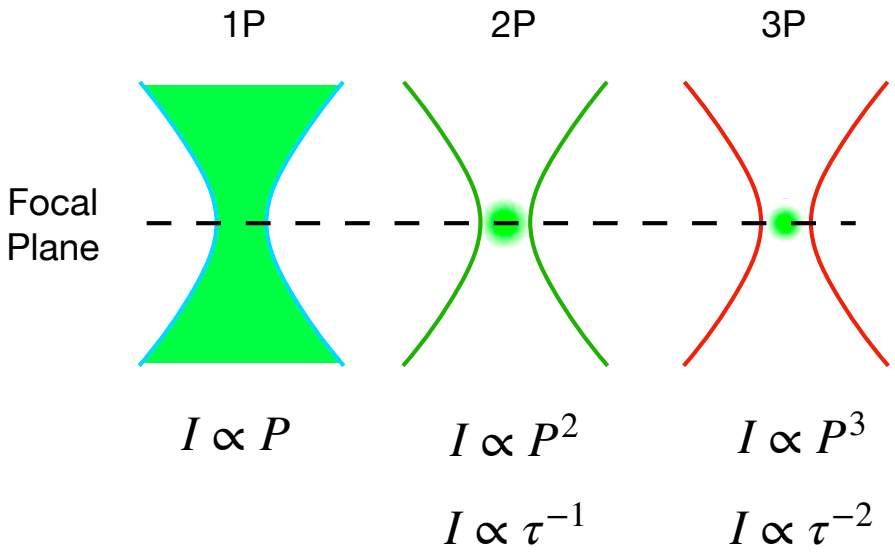

Figure 1.4: Comparison of focal excitation volumes for single-, two-, and three-photon excitation (left to right). The dependence on pulse duration and applied power is shown. In the single-photon case there is a linear relationship between excitation intensity and fluorescence, with no requirement for pulsed excitation. The three-photon excitation volume is shown as an idealised case; in practice, higher power requirements broaden this volume.

pared to single-photon techniques, due to its use of longer excitation wavelengths [4, 5, 9].

A simplified version factors that contribute to the generation of fluorescent signal in multiphoton absorption can be expressed as:

$$\langle F(t) \rangle \propto \frac{\sigma_n P^n}{\tau^{(n-1)}} \tag{1.2}$$

where τ represents the pulse duration of the laser pulse used and P is the applied power. σ_n represents the cross sectional area of the fluorophore used, a quantity that essentially determines how efficiently n number of photons can be absorbed by a fluorophore. This is a process/order dependent parameter that is discussed further

in Chapter 4.5.

1.2.2 Microscope Design

A basic layout of a multiphoton microscope is shown in Figure 1.5. The essential components enable the laser beam to be raster-scanned across the sample, with an image reconstructed from the collected fluorescence at each pixel. The size and magnification of the image are determined by the angular deviation of the galvanometer mirrors, which must be matched to the specified pixel resolution. Under this mode of operation, the amount of time each pixel is illuminated for is defined as the *dwell time*. In three-photon microscopy, the dwell time is typically on the order of 1 µs, although it can vary depending on the repetition rate of the excitation source and the fluorescence properties of the sample.

The choice of scanning strategy introduces trade-offs between imaging speed, field of view (FOV), and signal-to-noise ratio. Galvanometer-based scanners are widely used for flexible frame scanning, offering good spatial resolution with moderate acquisition speeds. Resonant galvanometers enable higher frame rates at the expense of reduced dwell time per pixel, which can compromise sensitivity in weakly fluorescent samples. More generally, there is a fundamental trade-off: larger fields of view and faster frame rates both reduce the time available to integrate fluorescence at each pixel. Line scanning, where the laser illuminates an entire line sequentially, offers faster acquisition than full-frame scanning but reduces the degree of optical sectioning.

Detection is most commonly achieved using a photomultiplier tube (PMT) coupled to a transimpedance amplifier. Fluorescence photons collected by the micro-

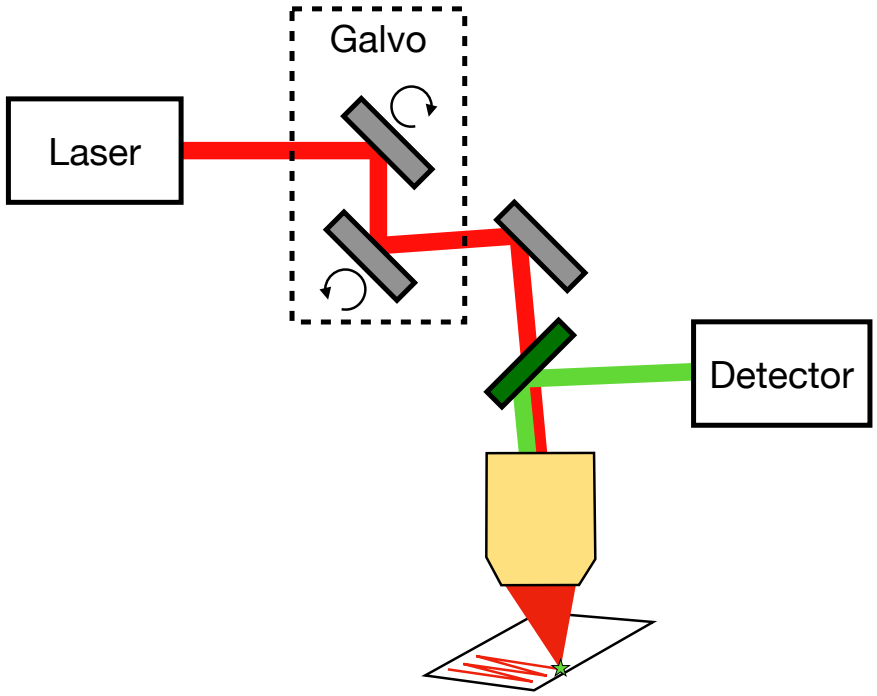

Figure 1.5: Simplified schematic (not to scale) of a multiphoton microscope. The laser beam, directed by a pair of galvanometer mirrors (galvos), passes through a dichroic mirror before illuminating the sample. The resulting backscattered fluorescence is redirected by the dichroic and collected by a fast detector.

scope are converted into photoelectrons at the PMT photocathode and subsequently multiplied through a series of dynodes, producing a current proportional to the incident light intensity [10]. This current is then converted into a voltage signal and amplified by the transimpedance amplifier for digitisation and image reconstruction.

The sensitivity of the detection system can be adjusted by varying the bias voltage applied to the PMT. Increasing the bias voltage increases the detector gain, allowing weaker fluorescence signals to be measured. However, this also amplifies detector noise, resulting in a trade-off between sensitivity and signal-to-noise ratio.

Detector performance is strongly influenced by quantum efficiency, which determines the fraction of incident photons that are converted into detectable electrons. More advanced detectors, such as gallium arsenide phosphide (GaAsP) PMTs and hybrid detectors, provide higher quantum efficiency and lower noise than conventional PMTs [11]. As a result, they offer improved sensitivity for photon-limited applications, making them particularly well suited to deep-tissue and three-photon microscopy where fluorescence signals are often extremely weak.

In addition to sensitivity, spectral separation of the emitted fluorescence is a crucial element of microscope design. Dichroic mirrors and bandpass filters are used to split the emission into different wavelength channels, allowing simultaneous imaging of multiple fluorophores. The efficiency of this process is critical in multiphoton imaging, where signal levels are often low and cross-talk between detection channels can obscure quantitative measurements.

1.2.3 Resolution Limit

All real optical systems are subject to diffraction, which arises when light passes through a finite aperture such as a lens. Diffraction prevents the focal spot from being a perfect point, instead broadening it both laterally and axially. This phenomenon was first described by Ernst Abbe [12], who derived an expression for the diffraction-limited resolution of an optical microscope:

$$d = \frac{\lambda}{2n \sin(\theta)} = \frac{\lambda}{2\mathrm{NA}} \tag{1.3}$$

where d is the smallest resolvable feature for an illumination wavelength λ, refractive index n, and angle θ, representing the half-angle of the geometric focal cone of

the imaging lens. The numerical aperture (NA) is defined as $\mathrm{NA} = n \sin\theta$. Improving resolution therefore requires maximising the NA of the objective lens. Modern microscope objectives are designed to achieve high NA while balancing aberrations that arise from complex lens geometries.

In multiphoton excitation, the PSF is further shaped by nonlinear effects: the probability of excitation scales with the intensity raised to the number of photons absorbed (I^n). This results in a theoretically enhanced confinement of the excitation volume, particularly in the axial direction but is then curtailed with an increase in required power. The effective PSF also depends on the excitation wavelength: shorter wavelengths produce smaller focal spots, while longer wavelengths reduce scattering and improve imaging depth.

For 2 photon processes, the point spread function (PSF) can be estimated using the approximation given by Zipfel [5]:

$$\omega_{x,y} = \begin{cases} \dfrac{0.320\lambda}{\sqrt{2}\mathrm{NA}} & \mathrm{NA} \leq 0.7 \\ \\ \dfrac{0.325\lambda}{\sqrt{2}\mathrm{NA}^{0.91}} & \mathrm{NA} \geq 0.7 \end{cases} \qquad \omega_z = \frac{0.5432\lambda}{\sqrt{2}} \left[\frac{1}{n - \sqrt{n^2 - \mathrm{NA}^2}} \right] \tag{1.4}$$

This approximation describes the $1/e$ values for the lateral ($\omega_{x,y}$) and axial (ω_z) resolution limits. Converting these into full-width at half-maximum (FWHM) a factor of $2\sqrt{2}$ is applied. These values define the approximate dimensions of the PSF, which describes the intensity distribution of light at the focal spot. While the Zipfel approximation provides analytical estimates for a diffraction-limited system, the PSF can also be calculated numerically as the Fourier transform of the beam

profile at the back aperture of the objective. The theoretical PSF is typically an Airy disk, resembling a Gaussian distribution with side lobes. This is since the focal volume can be thought of as the Fourier transform of the beam at the entrence pupil of the objective lens.

In practical imaging, the PSF is broadened by scattering and aberrations within biological tissue. Immersion media, such as water or oil, are selected to match the refractive index of the sample and reduce spherical aberration. Pulse duration also affects the effective PSF: shorter femtosecond pulses maximise the probability of multiphoton excitation at the focal spot without increasing out-of-focus excitation [13].

Experimental validation of the PSF is commonly performed using sub-resolution fluorescent beads, allowing measurement of the effective FWHM and comparison with theoretical predictions [14]. This step accounts for real-world effects such as lens aberrations, scattering, and beam misalignment.

It is important to note that increasing excitation power can cause broadening of the smallest resolvable structures since the probability of generating multiphoton signal increases with power [15]. This is particularly relevant in three-photon microscopy, where higher powers are required to generate sufficient signal. Understanding the interplay between diffraction, nonlinear excitation, pulse duration, and tissue-induced aberrations is critical for predicting practical resolution in multiphoton microscopy, guiding the selection of excitation wavelength, objective lens, and imaging depth for a given experiment.

1.3 Pulsed Lasers

Pulsed lasers are essential in multiphoton microscopy [16] to achieve the peak powers required for nonlinear absorption while avoiding photodamage to biological samples. High peak powers can be delivered in short bursts while keeping the average intensity low [17]. Figure 1.6 shows a schematic of the temporal energy output of a pulsed laser (not to scale).

Pulsed lasers have been shown to range into the attosecond (as, 1×10^{-18} s) regime [18], although in this work and multiphoton microscopy in general, we primarily use femtosecond (fs, 1×10^{-15} s) pulses. The repetition rate of these pulses is generally between 1–100 MHz.

As an example, a 50 fs, 10 mW (average), 1 MHz beam with a Sech^2 pulse shape produces pulses with an instantaneous power of approximately 176 kW and a pulse energy of 10 nJ. This illustrates how a relatively low average power beam can generate nonlinear effects without damaging the sample.

Several methods exist to generate ultrashort pulses. The most commonly used in multiphoton microscopy is *mode-locking*, due to its ability to produce very short pulse durations [19]. In mode-locked lasers, the cavity supports multiple standing waves (modes), whose interference leads to the formation of pulses in time. The repetition rate of these pulses is determined by the cavity length.

Previously the Ti:Sapphire laser was commonly used in multiphoton imaging - providentially 2 photon imaging [20]. whose output wavelength can be tuned between approximately 650–1100 nm by adding dispersive elements to the cavity, although this can affect output power. Commonly used dyes require higher wavelength excitation in order to excite three photon fluorescence, typically in the ranges of 1300 & 1700nm.

High powered ytterbium-doped fibre lasers are commonly used in three photon

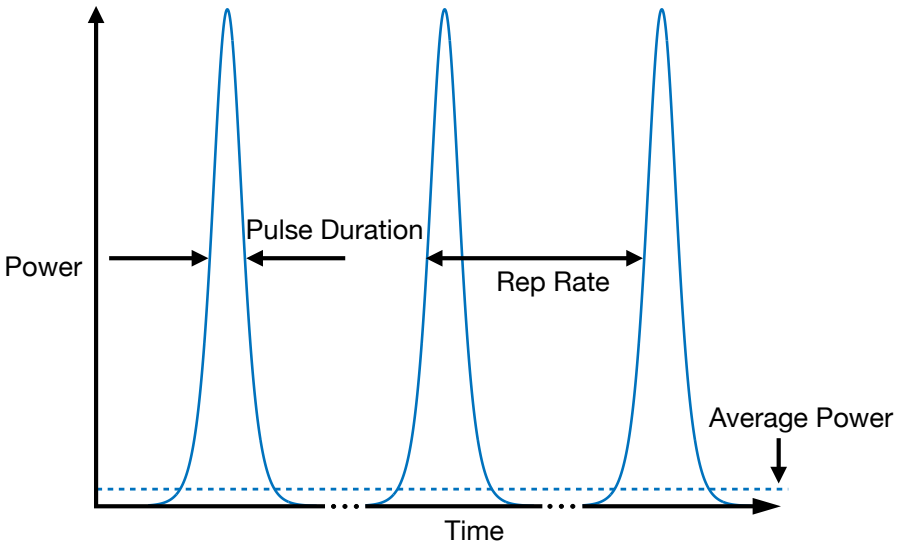

Figure 1.6: Time-dependent behaviour of pulsed lasers (not to scale). The repetition rate determines how often pulses are emitted (Hz), while the pulse duration defines the temporal length of each pulse.

microscopy as the pump source, due to their ability to generate high powered pulsed output. When other wavelengths are required, the output can be converted using an optical parametric amplifier (OPA) or an optical parametric oscillator (OPO), as discussed in Section 3.2. The fairly recent developments in high powered fibre laser sources have led to the realisation of three photon imaging, providing high pulse energy with short pulse duration [21].

In multiphoton microscopy, several types of pulsed lasers are commonly used. Ti:Sapphire lasers are widely employed because they provide tunable femtosecond pulses between 650 and 1100 nm, suitable for both two- and three-photon excitation. Ytterbium-doped fiber lasers typically emit around 1030–1060 nm with high repetition rates, offering advantages for deeper imaging due to reduced scattering. To further extend the wavelength range, optical parametric amplifiers or oscillators can be used, producing infrared output up to approximately 1.3 µm for two-photon

or 1.7 µm for three-photon excitation, which allows flexible excitation of different fluorophores.

The efficiency of multiphoton excitation is strongly influenced by the characteristics of the pulses. Shorter pulse durations produce higher peak intensities, increasing the probability of nonlinear absorption. The repetition rate of the pulses determines the number of excitation events per second, which must be balanced to optimise signal accumulation while avoiding photodamage. The temporal shape of the pulses, for example Gaussian or Sech^2, also affects the peak power and consequently the efficiency of multiphoton excitation.

1.4 Bandwidth Duration Limit

The connection between temporal and frequency domains is formalised by the Fourier transform, which dictates the limit in which the frequency components of a pulse cannot vary independently of its temporal profile [22]. This relationship can be expressed via the bandwidth–duration product:

$$\Delta\omega_p \Delta\tau_p \geq 2\pi c_B \tag{1.5}$$

Here, $\Delta\omega_p$ represents the optical bandwidth and $\Delta\tau_p$ the pulse duration. The constant c_B depends on the pulse shape, with $c_B = 0.441$ for a Gaussian pulse and $c_B = 0.315$ for a Sech^2 pulse [22].

This relation implies several important rules for laser pulse design. First, there is a minimum achievable pulse duration for any given frequency bandwidth. Second, achieving shorter temporal pulses requires a broader frequency spectrum, whereas narrow spectral bandwidths necessarily lead to longer pulse durations.

For multiphoton microscopy, shorter pulse durations are essential because they

maximise the instantaneous intensity at the focal point, which increases the probability of nonlinear absorption and ensures that excitation occurs before the virtual state of the fluorophore decays.

Beyond the general bandwidth–duration relation, we can approximate the temporal pulse profile using the measured spectrum of a pulsed laser, $S(\lambda)$. This spectrum represents the resonant modes within the laser cavity and can be converted into frequency space via:

$$S(\omega) = S\left(\frac{2\pi c}{\lambda}\right), \tag{1.6}$$

In frequency space, the amplitude of the electric field can be obtained from the intensity using $\mathrm{I} = |E|^2$. Assuming negligible phase shifts, the electric field can be expressed as:

$$\tilde{E}(\omega) = \sqrt{S(\omega)}\, e^{i\phi(\omega)} \tag{1.7}$$

Applying the inverse Fourier transform to the electric field $\tilde{E}$:

$$E(t) = \frac{1}{2\pi} \int_{-\infty}^{\infty} \tilde{E}(\omega)\, e^{-i\omega t}\, d\omega, \tag{1.8}$$

yields an approximation for the temporal field of the laser pulse:

$$E(t) \approx \sum_{j=1}^{N} \sqrt{S(\omega_j)}\, \cos\big(\omega_j t\big) \tag{1.9}$$

Using this method with measured data from the Axon 1064-TPC laser (1064 nm, pulse duration < 150 fs, 80 MHz), we can reconstruct the temporal behaviour of the pulse. Figure 1.7 shows the normalised intensity profile obtained by squaring the

electric field.

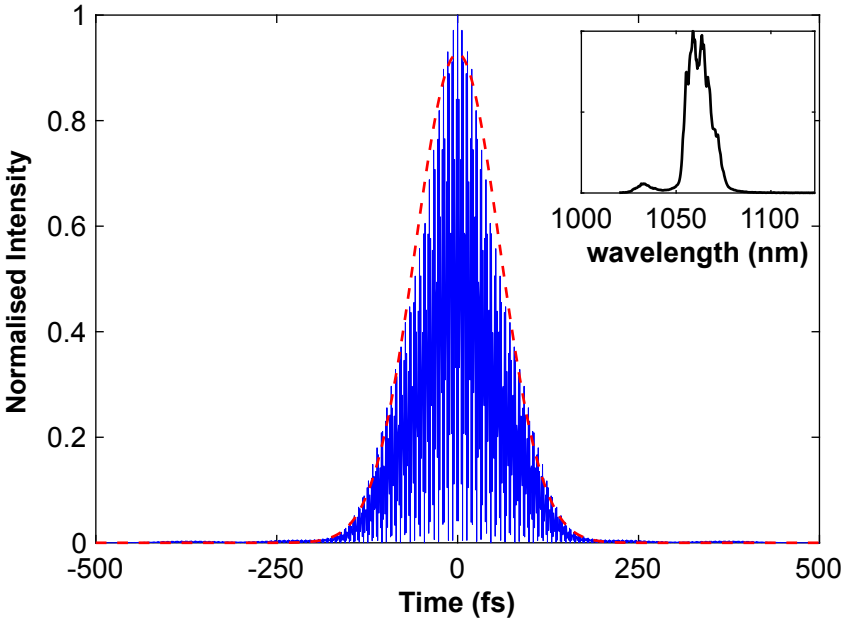

Figure 1.7: Bandpass example: the normalised spectrum (inset) of the Axon-1064 TPC was measured using an Optics HR4000CG-UV-NIR spectrometer and analysed using Equation 1.9. The raw absolute intensity is shown in blue, with a Sech^2 fit of the peak values in red generated via least squares in MATLAB. This yields an approximate bandpass-limited pulse duration of $\tau_p \approx 132$ fs.

Analysis of the spectrum in Figure 1.7 gives a spectral bandwidth $\Delta\lambda$ of 13 nm via a Gaussian fit, corresponding to a minimum pulse duration of 92 fs for a Sech^2 temporal profile. Comparing this value to the 132 fs obtained from the temporal reconstruction reveals a discrepancy of approximately 40 fs. This difference can be attributed to several factors. First, Equation 1.5 assumes an ideal Gaussian spectrum, whereas the measured spectrum more closely resembles a top-hat function, which alters the effective bandwidth–duration relationship. Second, oversampling or numerical approximations in the temporal reconstruction may introduce additional deviations. Despite these differences, the reconstructed pulse remains consistent with the requirements for effective multiphoton excitation, demonstrating that the pulse

duration is sufficiently short to achieve high peak intensities at the focus.

1.5 Optical – Temporal Dispersion

Unlike single-mode continuous wave (CW) lasers, pulsed lasers emit over a relatively wide spectral bandwidth. When propagating through optical media, this spectral variation becomes significant because the refractive index is wavelength dependent, $n(\lambda)$. Different spectral components therefore travel at different velocities, causing a relative delay between them and resulting in an overall elongation of the pulse. This temporal broadening can reduce the peak intensity at the focal point, which is critical in multiphoton microscopy where short, high-intensity pulses are required to excite virtual states before they decay.

To formalise this elongation, we begin with the expression for a laser pulse propagating in free space:

$$E(z,t) = A(t)e^{\,i(kz-\omega_0 t+\phi(t))} \tag{1.10}$$

where $A(t)$ is the pulse envelope, which can take forms such as Gaussian, Lorentzian, or Sech^2.

In a more realistic scenario, where the pulse propagates through a medium, the frequency-dependent propagation constant $k(\omega)$ is introduced:

$$k(\omega) = \frac{n(\omega)\,\omega}{c} \tag{1.11}$$

Expanding $k(\omega)$ about a carrier frequency ω_0 gives:

$$k(\omega) = k_0 + k'(\omega-\omega_0) + \frac{k''}{2}(\omega-\omega_0)^2 + \frac{k'''}{6}(\omega-\omega_0)^3 + \cdots \tag{1.12}$$

For a propagation length L, the spectral phase is $\phi(\omega) = k(\omega)L$.

The per-length dispersion coefficients are expressed as:

$$\begin{aligned} k_0 &= \frac{\partial^0 k}{\partial \omega^0} = k \qquad & k' &= \frac{\partial k}{\partial \omega} = \frac{1}{v_g} \\ k'' &= \frac{\partial^2 k}{\partial \omega^2} = \frac{\partial}{\partial \omega}\left(\frac{1}{v_g}\right) & k''' &= \frac{\partial^3 k}{\partial \omega^3} = \frac{\partial^2}{\partial \omega^2}\left(\frac{1}{v_g}\right) \end{aligned} \tag{1.13}$$

Here, k'' is the group velocity dispersion (GVD), describing the variation of group velocity with frequency per unit length. As different spectral components of the pulse travel at slightly different speeds, higher-frequency components may lag or lead lower-frequency components depending on the sign of the dispersion, leading to temporal broadening. Using this spectral phase, the zeroth-, first-, second-, and third-order terms of pulse propagation can be expressed as:

$$\phi_0(\omega) = k_0 L, \quad \tau_g = \frac{L}{v_g}, \quad \text{GDD} = k'' L = \frac{d^2\phi}{d\omega^2}, \quad \text{TOD} = k''' L = \frac{d^3\phi}{d\omega^3} \tag{1.14}$$

In this expression, $\phi_0(\omega)$ represents a constant phase shift, which generally has no observable effect but is included for completeness. The first-order term τ_g describes a uniform time delay of the pulse after travelling a distance L. The second-order term, group delay dispersion (GDD), in units of s^2, quantifies the evolution of the spectral phase with propagation and is primarily responsible for pulse broadening. The third-order term, third-order dispersion (TOD), in units of s^3, is the derivative of GDD and can introduce asymmetry in the pulse, creating tailing on one side depending on the sign of the chirp.

In practice, GDD and TOD arise from a variety of optical elements, including lenses, objectives, mirrors, beam splitters, and even air for very short pulses. TOD becomes particularly significant for very short pulses (< 50 fs) because their broader

spectral width experiences larger variations in refractive index across the spectrum [23]. This phase difference between spectral components modifies the group velocity of the pulse as it propagates through the medium, resulting in temporal broadening and potential asymmetry. Understanding and managing this dispersion is critical to ensure that pulses maintain sufficient peak intensity for efficient multiphoton excitation.

For a pulse of duration $\Delta\tau_0$ that is altered by some amount of GDD we can characterise the temporal elongation that it experiences, assuming a Sech^2 pulse shape using the equation:

$$\Delta\tau = \Delta\tau_0\sqrt{1+\left(\frac{2\ln(1+\sqrt{2})\,\text{GDD}}{\Delta\tau_0^2}\right)^2} \tag{1.15}$$

where $\Delta\tau$ is the resulting pulse duration and GDD is the amount of dispersion undergone, measured in fs^2. This relation can also be used to determine the amount of dispersion undergone from changes in pulse duration.

To illustrate the importance of dispersion management in a practical microscopy context, Figure 1.8 shows the elongation that both a 150fs and 50fs pulse under relatively low amounts of GDD, a typical microscope will be around 10kfs^2.

To add some context to how this effects the signal generation in multiphoton microscopy we can consider the following relation:

$$F \propto \left(\frac{\tau_0}{\tau}\right)^{n-1} \tag{1.16}$$

Where n is the order of the process, τ is the bandwidth limited pulse, τ_0 is the elongated pulse and F is the fluorescent yield. For the 150fs pulse being broadened

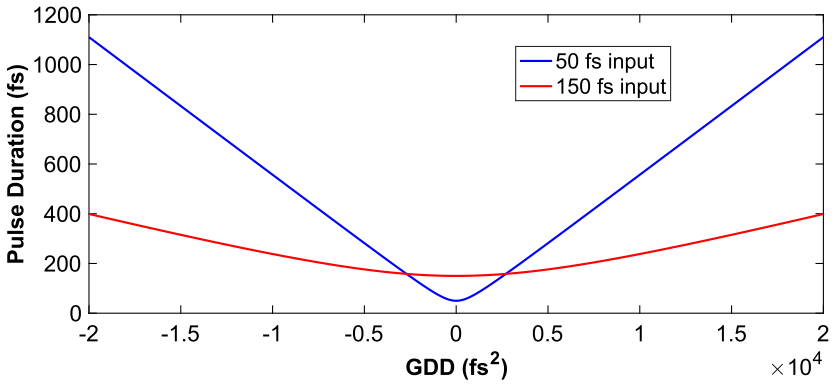

Figure 1.8: Example of pulse elongation with both positive and negative GDD. Here the initially bandpass limited 50fs pulse is dispersed to a higher degree, when compared to the 150fs pusle, due to its broader spectral bandwidth.

by 2kfs^2 of GDD (a typical low NA objective) we can consider the resulting loss of peak fluorescent signal given the order of the process:

- 2-photon (n = 2): ≈ 0.375, corresponding to a $\sim 62.5\%$ decrease in signal.
- 3-photon (n = 3): $\approx 0.375^2$, corresponding to a $\sim 86\%$ decrease in signal.

Without compensation, this broadening significantly reduces multiphoton excitation efficiency, this can drive an increase in applied power and can increase photodamage outside the focal plane, often damaging the sample being imaged / substrate. For shorter pulses, such as 50 fs or below, careful dispersion management becomes critical to preserve both peak intensity and multiphoton signal at the focus.

1.6 Management of Dispersion

Maintaining short pulse durations at the sample is critical for multiphoton microscopy, as high peak intensities are required to efficiently excite virtual states and

drive nonlinear absorption. Any uncorrected dispersion reduces the peak intensity at the focal point, decreasing excitation efficiency and degrading image quality [24].

Several optical strategies exist to manage dispersion in ultrafast laser systems. A common approach is pulse compression using prisms or gratings. In such setups, the spectral components of a pulse are spatially separated and then recombined, introducing negative GDD that pre-compensates for positive GDD accumulated along the optical path. This restores the pulse to near its original duration if the applied compensation is matched to the dispersion undergone.

The cylindrical lens configuration, illustrated in Figure 1.9, enables tunable dispersion control by introducing a variable optical path difference between spectral components through a single adjustable parameter. This pulse compressor design offers rapid and precise tuning of GDD with straightforward alignment and minimal beam distortion. In operation, the diffraction grating spatially separates the pulse spectrum, which is then focused onto a mirror by a closely coupled cylindrical lens. Small rotations of the cylindrical lens modify the relative path lengths of the dispersed frequency components, providing fine control of the overall dispersion.

Figure 1.10 shows the resulting pulse duration with changing angle, using the Coherent Chameleon Vision II laser operating at 800 nm, un-chirped, beam splitter (PBS105), quarter wave plate (Thorlabs AQWP05M-950), grating 600 lines per mm blaze at 750nm (Thorlabs GR25-0608), focusing lens 150mm (Thorlabs AC254-150-BML), cylindrical lens 200mm (Thorlabs LJ1653RM-B), silver mirror (Thorlabs PF10-03-F01). Pulse durations were measured using a commercial pulse measuring autocorrelator (APE TPE). The resulting GDD and pulse durations are shown in Figure 1.10, demonstrating that increasing negative GDD elongating the pulse duration.

Beyond conventional prism, grating, and cylindrical lens compressors, adaptive

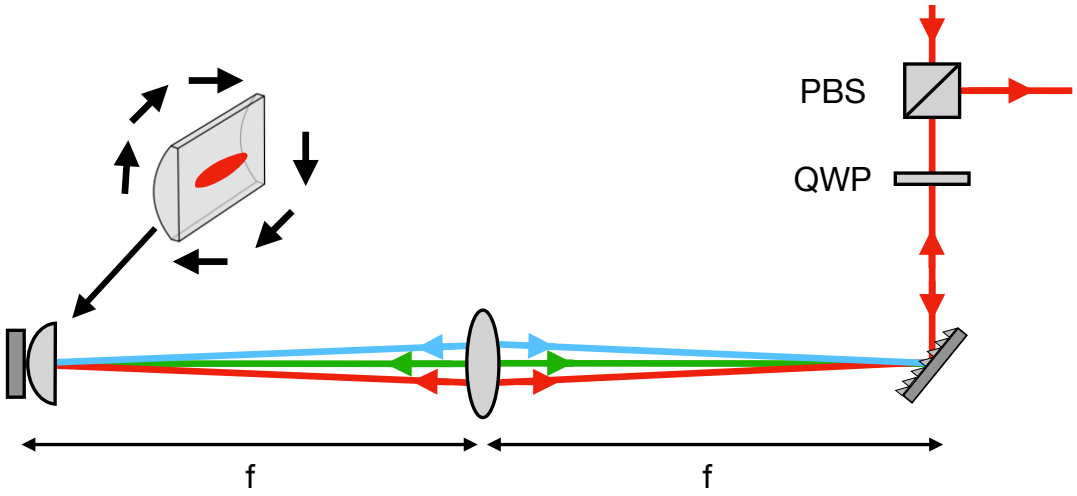

Figure 1.9: Rotating cylindrical lens compressor arrangement adapted from [25]. The dispersive grating separates spectral components, and the cylindrical lens introduces a controllable path difference, enabling tunable negative GDD. The polarising beam splitter (PBS) and quarter waveplate (QWP) combination allow the chirped pulse to exit. Errors in pulse duration and subsequently measured GDD are negligible. Errors of measured angle are taken as half the measurable increment.

optical methods provide flexible alternatives for dispersion management. Spatial light modulators (SLMs) can be programmed to apply arbitrary phase corrections across the spectral bandwidth [26], enabling simultaneous GDD and higher-order dispersion compensation. Similarly, techniques such as Multiphoton Intrapulse Interference Phase Scan (MIIPS) allow measurement and correction of both second- and higher-order spectral phase distortions, optimising the pulse shape at the focus in real time. These methods are particularly valuable in complex microscope setups with multiple dispersive elements or when ultrashort pulses ($<$50 fs) are required [27].

Overall, the choice of dispersion management method depends on the laser spectrum, optical path, and experimental flexibility. Prism compressors provide robust negative GDD over broad bandwidths, grating compressors allow precise tunabil-

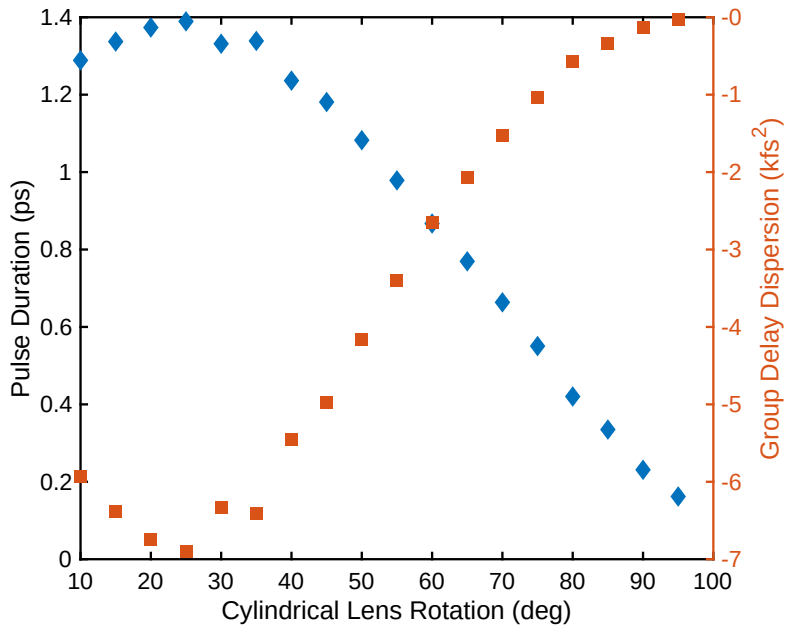

Figure 1.10: Measured pulse durations as a function of imposed GDD using the rotating pulse compressor, recorded with the APE-TPE autocorrelator.

ity, cylindrical lens setups offer convenient adjustment for fine-tuning, and adaptive methods like SLMs or MIIPS enable precise compensation in complex systems. Selecting an appropriate method ensures that ultrafast pulses reach the sample with minimal broadening, optimising multiphoton excitation.

2. Dispersion Management in Remote Focusing

This chapter describes work undertaken in collaboration with fellow postgraduate researcher Giedre Astrauskaite, focusing on the measurement and management of temporal dispersion in a two-photon microscopy system employing remote focusing.

The microscope in question incorporated a home-built remote focusing module which, while effective, introduced significant optical dispersion. The chapter outlines the use of autocorrelation techniques to characterise this dispersion. It then demonstrates how a home-built pulse compressor can be applied to restore the pulse to its shortest duration at the sample, thereby boosting the fluorescence signal.

2.1 Remote Focusing

Remote focusing [28] uses a secondary objective to rapidly shift the location of the focal spot. As illustrated in Figure 2.11, the setup consists of two optical arms. In the first arm, the beam passes through a quarter-wave plate (QWP) and two lenses before entering the first objective (Obj 1), which focuses it onto a mirror mounted on a fast actuator. The reflected beam then retraces its path through Obj 1 and the QWP, but its polarisation is now rotated by $\lambda/2$. This change in polarisation causes

the polarising beam splitter (PBS) to direct the beam into the second arm.

In the second arm, the beam is relayed via a 4f system—formed by the scan and tube lenses prior to the primary imaging objective (Obj 2). The 4f configuration ensures that focal lengths are matched, collimation is preserved, magnification remains constant, and aberrations are minimised.

By moving the mirror in the first arm, the focal plane of Obj 2 can be shifted without physically moving the objective or the sample [29]. This movement is typically achieved using a voice-coil actuator, which can oscillate a lightweight mirror at frequencies up to $\sim$1 kHz, enabling rapid refocusing in the primary objective.

Using this system remote focusing in multiphoton systems can be used to rapidly refocus the focal spot. There are many potential applications of this system for imaging fast biological processes [30, 31]. Here our aim is to perform functional imaging, tracing the action potential propagating transmurally [32] in heart tissue slices.

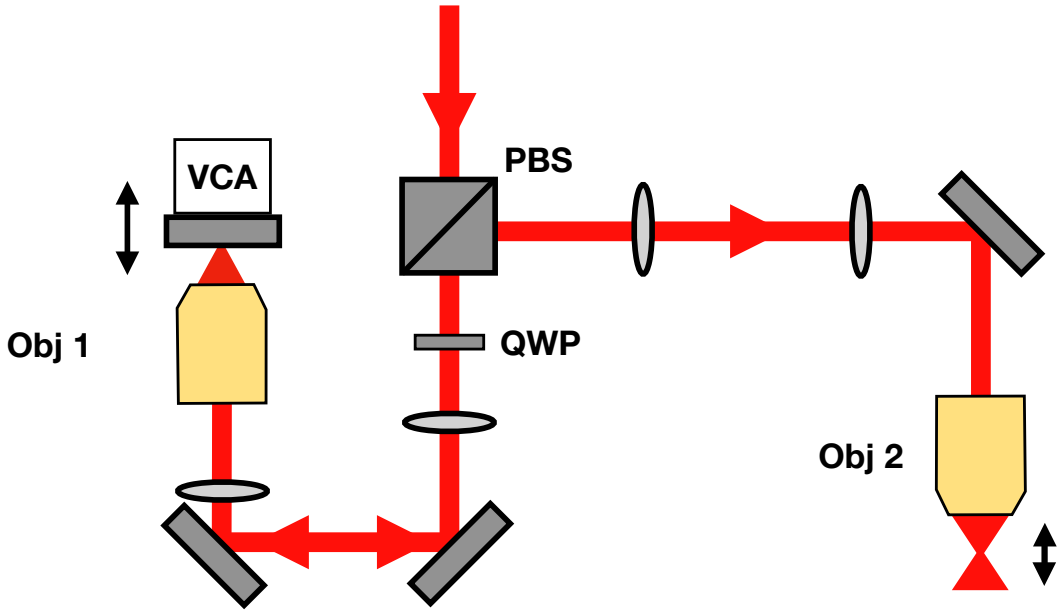

Figure 2.11: Principle of Remote Focusing, where QWP: PBS: Polarising Beam Splitter, Quarter Wave Plate and Obj: Microscope Objective, VCA: Voice Coil Actuator

2.2 Pulse Compression

As discussed earlier, temporal dispersion can significantly reduce generated fluorescence by temporally stretching the excitation pulse at the sample plane. To mitigate this effect, dispersion pre-compensation is essential. In our setup (Figure 2.1), the beam undergoes three passes through microscope objectives as well as multiple additional optical elements, including a beam splitter. The experimental configuration is shown in Figure 2.12. The laser source is a Coherent Chameleon Vision II (80 MHz, variable wavelength between 650-1100nm), followed by a Pockels cell (Conoptics 350-80 LA) for power modulation. The remote objective is a Nikon Plan Fluor 40×, NA 0.75 (air), and the primary objective is an Olympus XLUMPLFLN 20×, NA 1.0, 2 mm WD (water dipping). The beam path also includes a series of relay

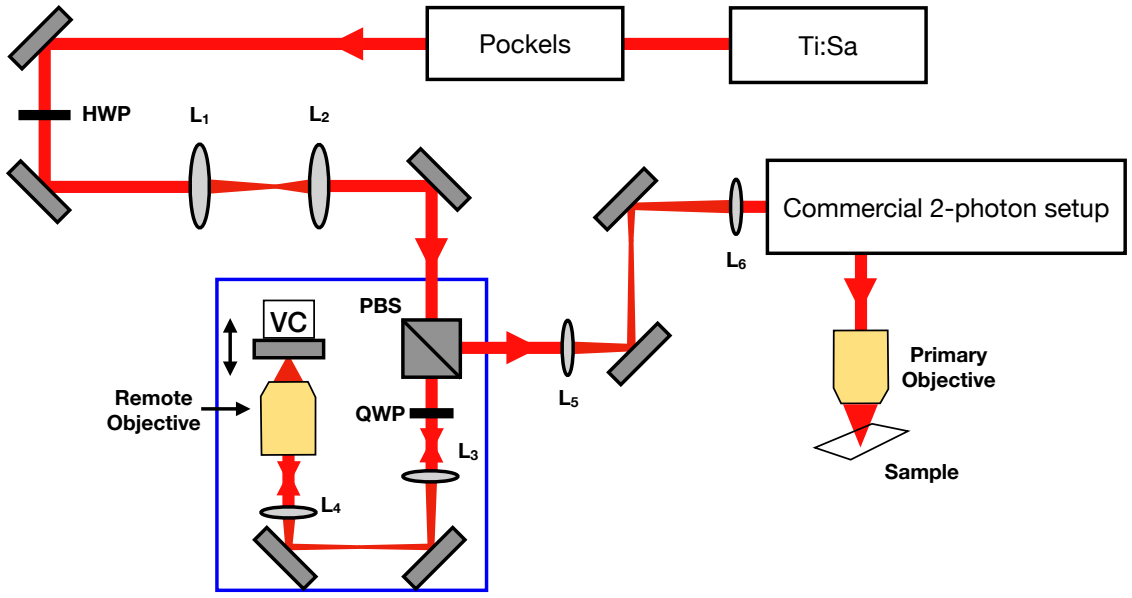

Figure 2.12: Experimental setup of multiphoton microscope with remote focusing system included (blue), where Ti:Sa: Titanium–Sapphire laser source, HWP: Half-wave plate

lenses (L1 = 50, mm, L2 = 100, mm, L3 = 125, mm, L4 = 200, mm, L5 = 175, mm, L6 = 100, mm). The commercial two-photon microscope is a Scientifica Hyper-Scope. After power modulation by the Pockels cell, the beam is expanded to overfill the back aperture of the remote objective, then resized before entering the Hyper-Scope—necessary because its internal scan and tube lenses are fixed.

From the optical layout alone, it is clear that the laser pulse will experience substantial temporal dispersion before reaching the sample. To address this, we take advantage of the built-in pre-compensation in the Coherent Chameleon Vision II, which can provide up to 22kfs^2 of dispersion compensation at 800 nm. The compensation from the laser was found to be insufficient for correcting the dispersion induced by the system, giving a net imbalance of compensation and precompensation leading to an overall temporal elongation. To negate this a system for measuring

and pre-compensating the pulse duration is required. To do so I designed and built a custom pulse compressor and an autocorrelator. These tools aim to allow us to directly measure the pulse duration at the sample plane and iteratively adjust pre-compensation to achieve the shortest possible pulse width at the sample.

2.2.1 Autocorrelation

To measure the duration of our laser pulse we turn to the technique known as autocorrelation. This name refers to the process wherein we use the pulse itself to measure itself, meaning that we create a convolution of the pulse [33]. More generally, autocorrelation is a mathematical operation used to quantify the similarity of a function with a delayed version of itself. In the context of ultrafast optics, the autocorrelation signal is generated by measuring the temporal overlap between a laser pulse and a time-delayed replica. Several autocorrelation methods exist, including second-harmonic generation (SHG) autocorrelation, interferometric autocorrelation, and polarization-gate autocorrelation, each offering different levels of temporal and phase information [34].

2.2.2 Intensity Only Autocorrelation

The intensity only autocorrelator has been chosen for pulse duration measurements, with a schematic of the system shown in figure 2.13. Here a Michelson interferometer is used: a beam splitter is used to make two copies of the pulse with a mirror used in each arm before recombining the beam, with half the original power focused onto a photodiode by a focusing lens. One of the mirrors in the interferometer is continuously actuated forwards and backwards reflecting the beam, generating a variable time delay between the arrival of each copy of the pulse at the photodiode.

In doing so a convolution is made possible via the pulse constantly overlapping itself backwards and forwards. Detection of the overlapping pulses is possible provided that the bandgap of the photodiode used is less than the wavelength used, allowing simultaneous absorption to trigger a signal - only when there is enough signal [35, 36].This can be formalised as:

$$h\nu < E_g < 2h\nu \tag{2.17}$$

where hν is the energy of the wavelength used and E_g is the photodiodes bandgap. Here the detector is therefore measuring multiphoton absorption rather than single photon absorption, creating a gating effect.

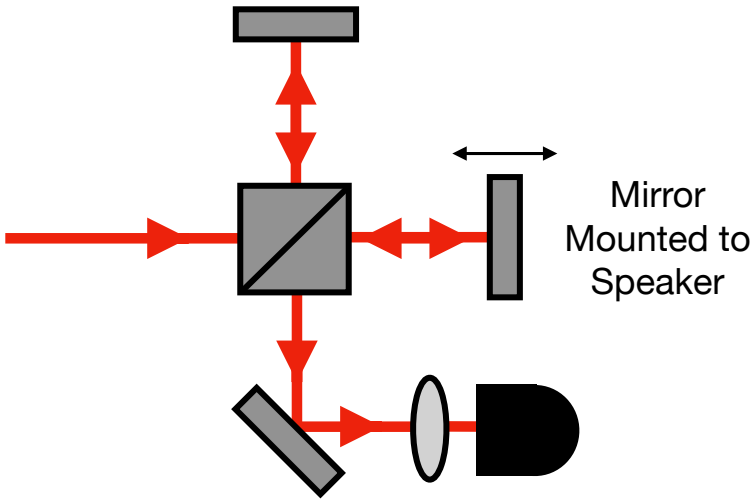

Figure 2.13: Intensity only autocorrelator, with a focusing lens used in conjunction with a visible light photodiode

An intensity-only autocorrelator using a two-photon absorption (TPA) detector measures the square of the instantaneous intensity at the detector.

Beginning with the electric field, E(t), of the laser pulse:

$$E(t) = \epsilon(t)e^{i\phi(t)}e^{i\omega_0 t} \tag{2.18}$$

where $\epsilon(t)$ describes the envelope / general function of the pulse, ϕ describes the phase at frequency ω_0 and t is time.

Considering that the intensity of the electric field is:

$$I(t) = |E(t)|^2, \tag{2.19}$$

where $E(t)$ is the electric field envelope of the pulse.

The pulse is split into two arms, one delayed by τ, giving the total intensity at the detector:

$$I_{\text{tot}}(t, \tau) = I(t) + I(t - \tau). \tag{2.20}$$

Considering we are measuring the two photon absorbance, this gives a dependency of intensity to generated signal as $S \propto I^2$, in accordance with two photon absorption. Therefore the square of the total intensity:

$$S(t) \propto \int_{-\infty}^{\infty} \left[I(t) + I(t - \tau)\right]^2 dt. \tag{2.21}$$

When $(\tau \to \infty)$ we can consider the normalised signal as:

$$S_B(t) = \int_{-\infty}^{\infty} I^2(t)\ dt + \int_{-\infty}^{\infty} I^2(t-\infty)\ dt = 2\int_{-\infty}^{\infty} I^2(t)\ dt \tag{2.22}$$

This term $S_B(t)$ can be considered the background of the measurement.

To determine the peak signal $S_P(t)$, we consider the case wherein we have a strong overlap ie $(\tau \to 0)$:

$$S_P(t) = \int_{-\infty}^{\infty} [I(t) + I(t)]^2\ dt = 4\int_{-\infty}^{\infty} I^2(t)\ dt \tag{2.23}$$

The peak expected signal-to-background ratio can then be given by:

$$\text{SBR} = \frac{S_P(t) + S_B(t)}{S_B(t)} = \frac{4\int_{-\infty}^{\infty} I^2(t)\ dt + 2\int_{-\infty}^{\infty} I^2(t)\ dt}{2\int_{-\infty}^{\infty} I^2(t)\ dt} = \frac{6}{2} = \frac{3}{1} \tag{2.24}$$

From this derivation we can determine a few key factors to consider when taking an autocorrelation of our laser pulse. The convolution $S(t)$ should have a SBR of around 3:1, importantly we should also consider the function shape 'envelope' of the pulse $\epsilon(t)$ as this will determine the de-convolution factor that we apply. The

industry standard for mode-locked pulses generated by Ti:Sa sources is assuming a sech^2 pulse shape [22], meaning that a deconvolution factor κ_ϵ will be applied:

$$\Delta\tau = \frac{\Delta S(t)}{\kappa_\epsilon} \tag{2.25}$$

where $\Delta S(t)$ is the FWHM of our measured trace, $\Delta\tau$ is the FWHM of the deconvolved pulse. For an intensity only autocorrelation and assuming a pulse with a sech^2 shape the deconvolution factor of $\kappa_\epsilon = 1.543$ [17] is applied.

The setup shown in figure 2.14 has been built and aligned, consisting of a beam splitter (Thorlabs BSW29R), and two silver mirrors (Thorlabs; PF10-03-P01, PF05-03-P01) with focusing lens Thorlabs (A230TM-B) used in conjunction with the Hamamatsu G1115 photodiode. Here the speaker is driven by a pair GW Instek AFG-225P and LEPY LP-2020A Amplifier with acquisition done with oscilloscope (Tektronix TDS 1001C-EDU). The speaker motion was used to periodically scan the delay arm. The oscilloscope was triggered synchronously with the speaker drive so that repeated scans were overlaid to produce a stable autocorrelation trace. By moving the stationary mirror shown in Figure 2.14 some known distance, two traces are measured with a known time delay between. This generates a timebase for the traces, given we can observe the relative time shift on the trace between measurements. An example trace is shown in Figure 2.15.

Next, we have extended the principle of intensity-only autocorrelation by measuring the pulse duration at the microscope sample. An adapted schematic of Figure 2.13 is shown in Figure 2.16. Here, the pulse pair is allowed to propagate through

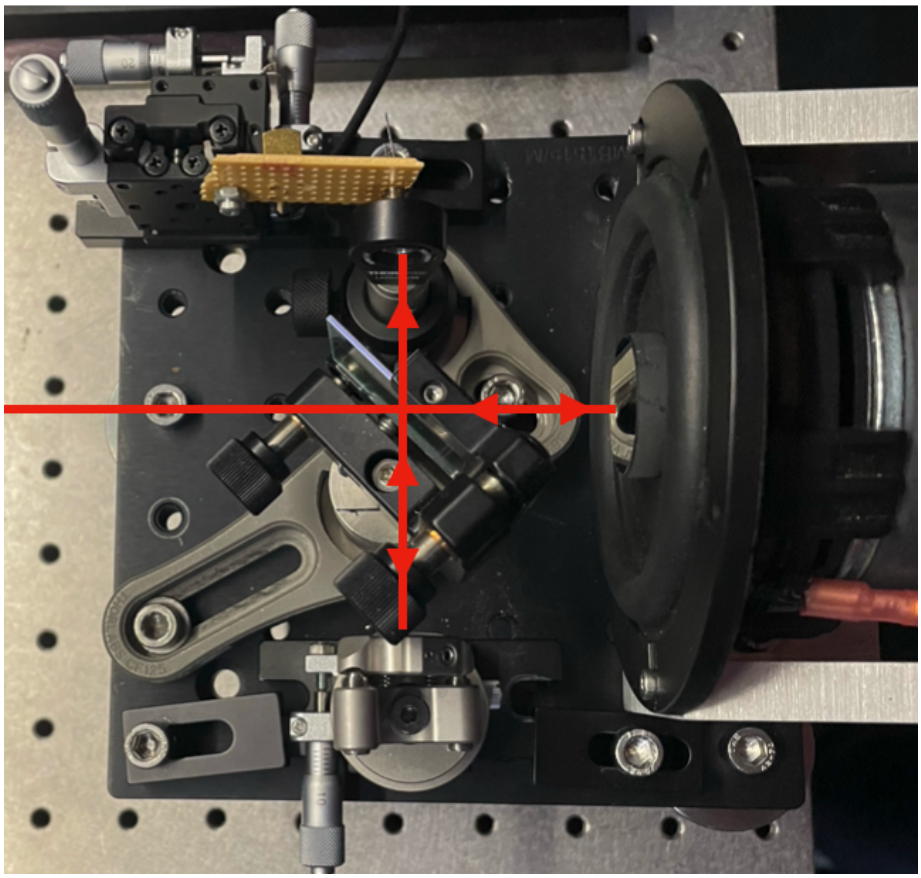

Figure 2.14: Autocorrelator setup, consisting of a simple Michelson interferometer

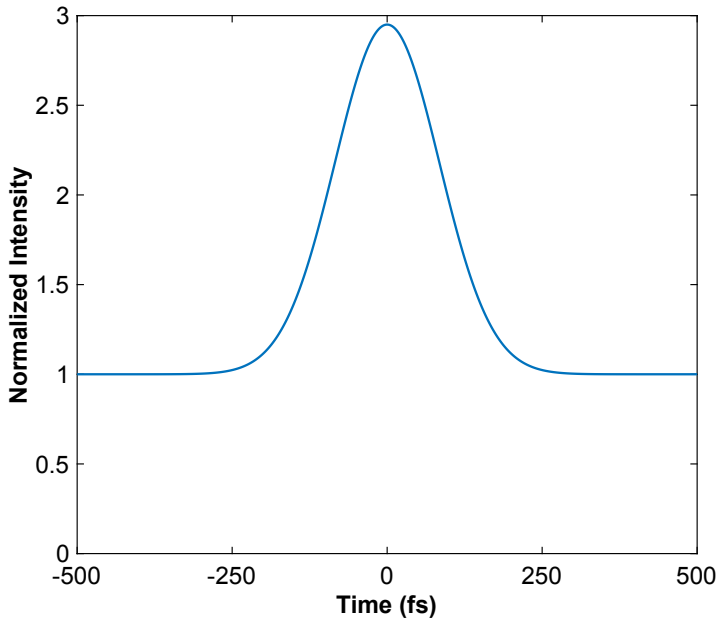

Figure 2.15: Autocorrelation trace of the Coherent Chameleon Vision II at 800nm with a measured fwhm = 218fs, (autocorrelation function fwhm = 218fs)

the microscope, using the microscope objective to focus onto the photodiode.

This system offers several advantages over measuring the pulse duration at arbitrary points within the microscope, as it allows the overall dispersion introduced by the microscope to influence the measured pulse duration. This technique therefore enables the direct measurement of the pulse duration actually experienced at the sample—a practice adopted in several systems where there is a need to determine the precise pulse duration at the focal plane [37, 38].

After taking the measurement of the pulse duration vs amount of GDD applied to the beam by the laser system alone it was then determined this was not enough precompensation to resolve the shortest pulse duration at the sample.

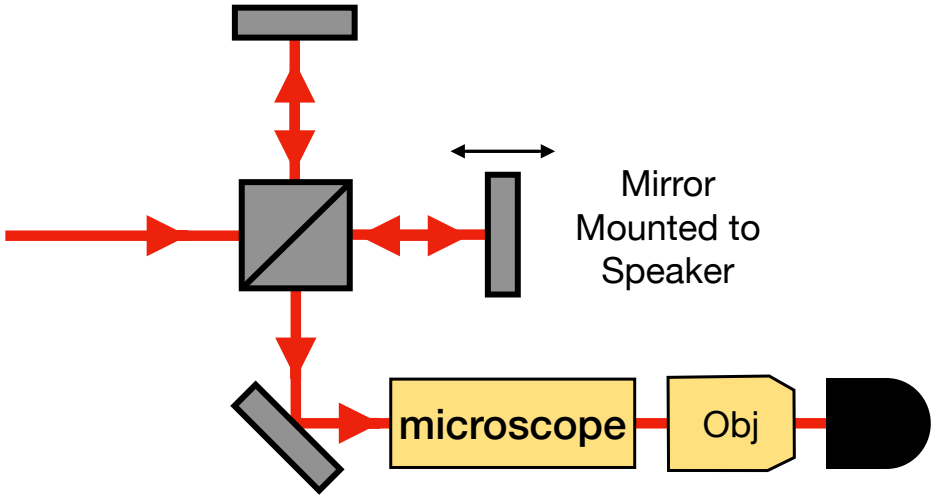

Figure 2.16: Inline Autocorrelator schematic

2.2.3 Single Prism Compressor

For a pulse compression solution I have opted to develop a single prism compressor, following a design developed by the Trebino Group [39], a development on the two prism design generated by Fork et al. [40]. Here the prism acts as a dispersive element that reverses the order of retardation imposed by bulk glass. While this causes a degree of magnification, the beam then undergoes the same process in reverse de-magnifying it. Shown in Figure 2.17 design has been chosen for its stability and simplicity. By changing the separation between the prism and the corner cube the total amount of negative GDD generated is altered, with the angle of the prism having the ability to adjust the central wavelength used in the setup. Additionally, small amounts of positive dispersion can be added through adjusting the insertion of the beam into the prism, shifting the prisms location in and out of the page as seen in Figure 2.17. Here the retroreflector returns the input beam perfectly antiparallel with respect to the input beam. Additionally, the path length within the retroreflector

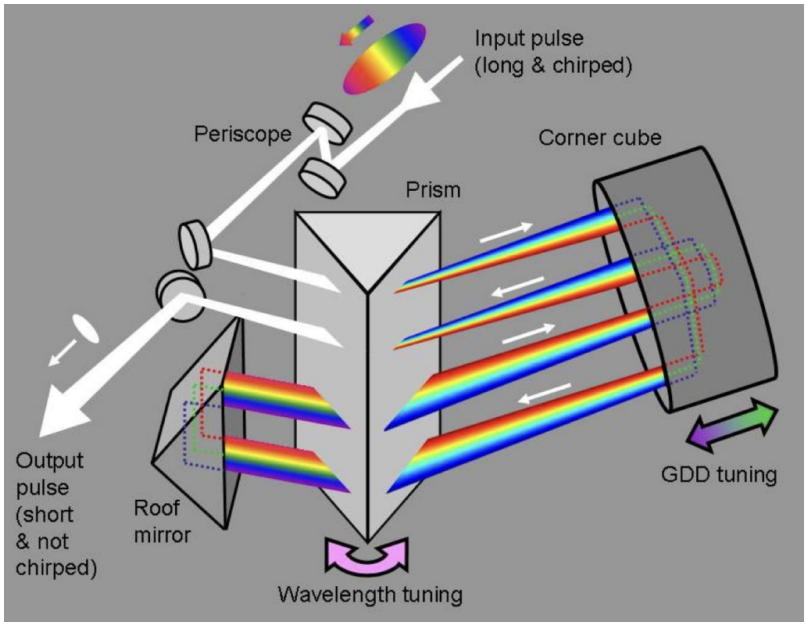

Figure 2.17: Single prism compressor, image taken from [39]

will be consistent irrespective of the input location of the beam.

A version of the single prism compressor has been built and is shown in Figure 2.18. This has been constructed using a 'D' shaped mirror (Thorlabs PFD10-03-P01), Mirror (Thorlabs PF10-03-P01), Roof Mirror (Thorlabs HRS1015-P01) Prism: N-SF11 based equilateral prism (thorlabs PS853), Retroreflector: Thorlabs HRR203-P01 and Stage: Translation stage with micrometer (Thorlabs LX10). Here retroreflector constructed of three perpendicular mirrors has been used where previously we used a prism retroreflector (Thorlabs PS976-B) - this was found to be problematic since the polarisation of light is altered by the retroreflector and in turn the refraction from the prism. Using this setup we can achieve a power throughput of around 60%, most losses occurring at the air prism interface. For a prism compressor this is a fairly high throughput although this could be improved further [41].

Using the basic setup described in Figure 2.19 I have measured the variation

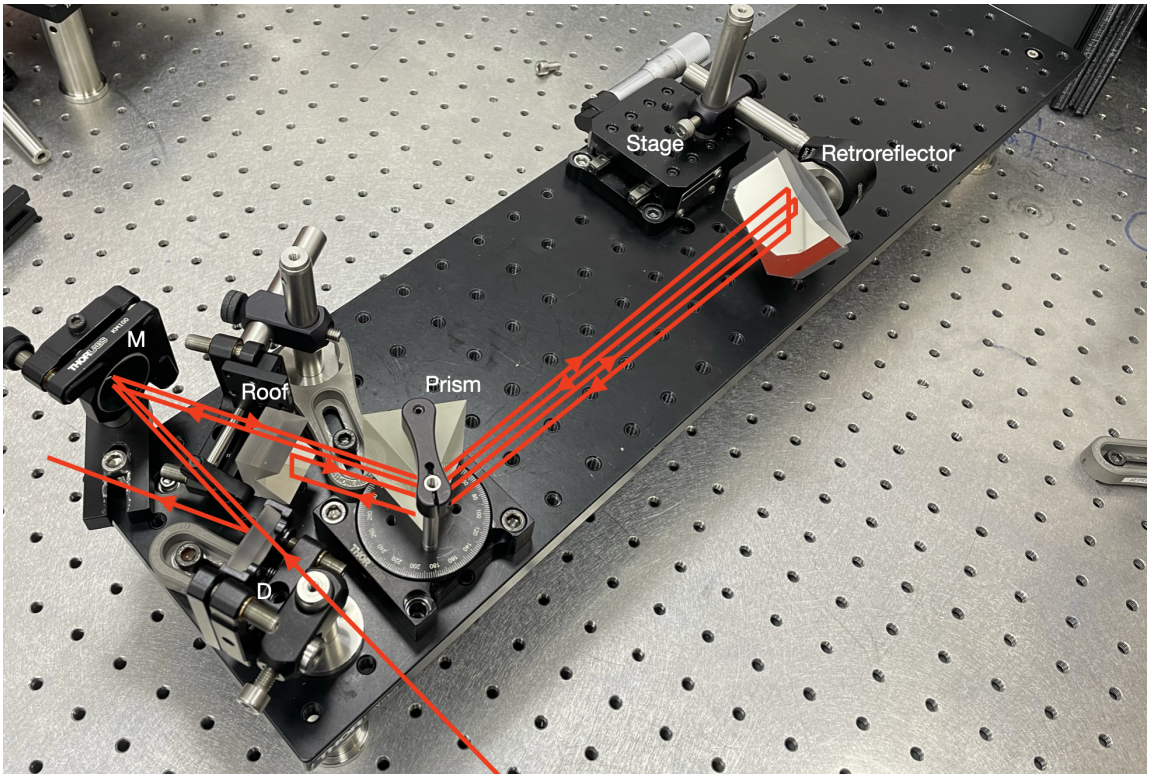

Figure 2.18: Single Prism Compressor, where D: 'D' shaped mirror , M: Mirror, Roof: Roof Mirror.

in pulse duration generated by the negative dispersion imposed on the beam with results shown in Figure 2.20. Here the laser is operated with 800nm and has no precompensation applied (achieved by selecting 0kfs^2 on the lasers software). Here it can be seen that the prism compressor is compensating for the pockels cell (+ any positive dispersion initially introduced by prism compressor) up until the separation of around $\approx$ 35cm, shown by the dip in pulse duration around this point. Following this the amount of induced GDD has also been calculated showing that both these factors amount to $\approx$ 9.5kfs^2

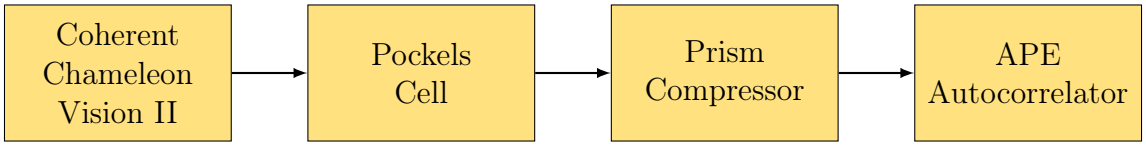

Figure 2.19: Setup used to measure variation in pulse duration using only the prism compressor.

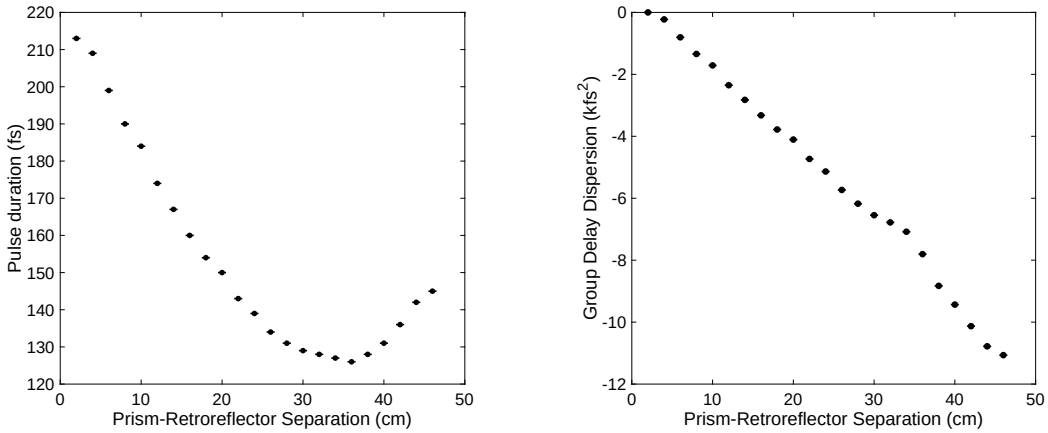

Figure 2.20: **A**: Pulse duration changes with retroreflector position as measured with the APE mini/TPE Autocorrelator. **B**: Estimation of imparted GDD with changing prism–retroreflector separation. Measured using the APE Mini TPA/PD shown in Figure 2.19. The error quoted by APE for the autocorrelator is negligible ($3.3\text{x}10^{-2}$fs).

2.3 Results

The autocorrelator and pulse compressor have been included in the setup for remote focusing as shown in Figure 2.21. Here the beam passes through both devices before the microscope. At the sample of the microscope the photodiode (Hamamatsu, G1115) is fixed in a 3D printed custom mount that is screwed into the sample stage of the microscope. Using this setup the pulse duration has been measured 50 times

for each position of retroreflector / prism separation. For this a custom MATLAB code that communicates with the oscilloscope allows for rapid acquisitions of this data.

A set of lenses has been included at the output of the compressor to re-collimate the beam. It was found that the output of the beam had a tendency to be divergent following the compressor. This was likely due to either the beam slightly clipping within the prism compressor, a possible change in path length between trips between the prism or a potential misalignment.

Results of pulse duration measurements for the setup are shown in Figure 2.22. This represents a minimum of 135fs at a prism-retroreflector separation of 44cm. Indicating a near bandwidth limited pulse. The compressor was therefore fixed at this separation for subsequent measurements at 800 nm using this optical configuration.

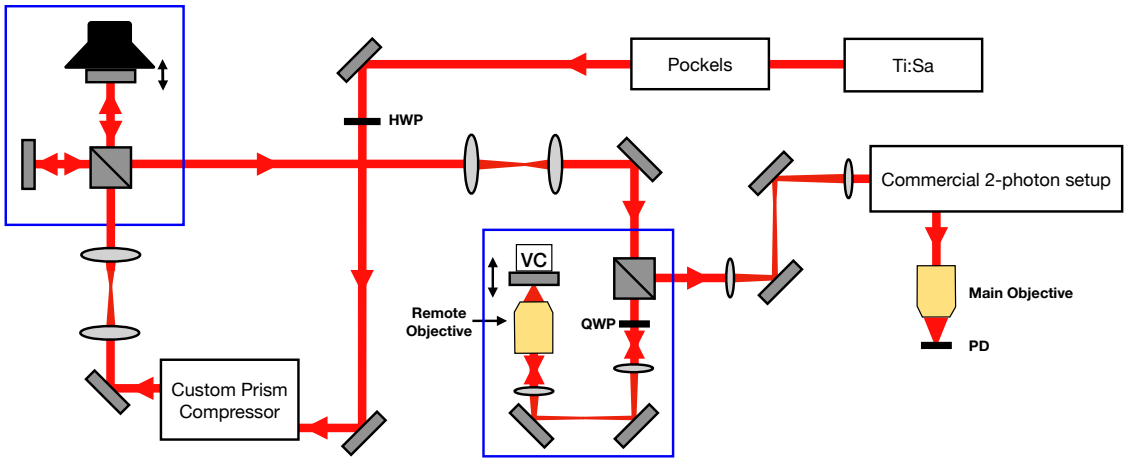

Figure 2.21: Remote focusing setup including the autocorrelator and pulse compressor.

In order to reassure we are in fact maximising the fluorescence gain with this measurement, multiphoton images of Fluorescein have been taken varying the pre-

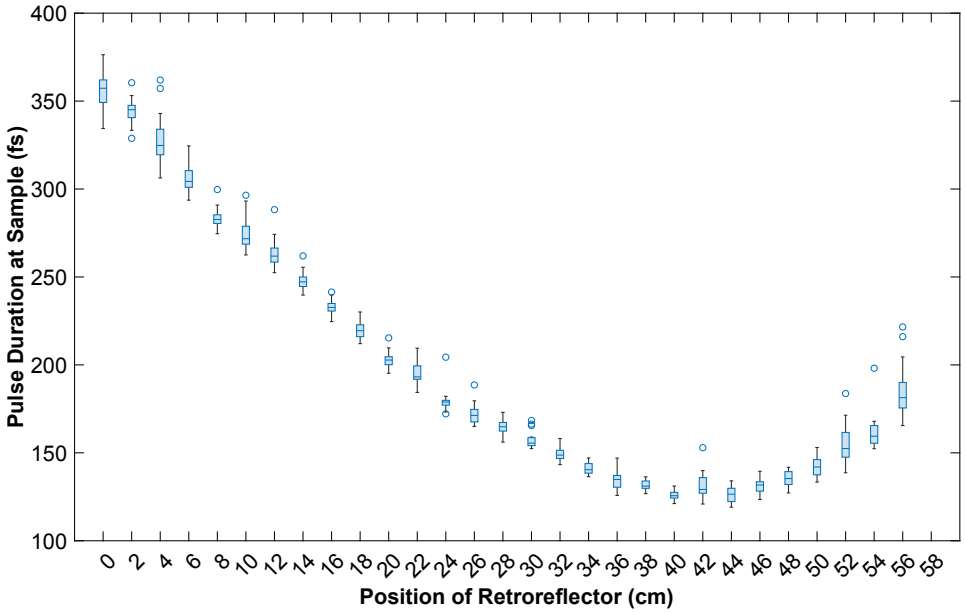

Figure 2.22: Pulse duration taken at sample with changing position of retroreflector. Here for each position 50 measurements have been taken with a box plot for each taken. The scattered data are outliers.

compensation applied. Here Fluorescein (Sigma Aldrich, 46960) has been dissolved in water with a concentration of 10 mg/100 ml deposited into a dish that the microscope objective is then dipped into. 2-Photon images were then taken of a 37x37 µm FOV with an average power of 8.91mW (measured using Thorlabs S121C). Precompensation was changed between images each measured value of precompensation 20 frames have been averaged with the mean grey value taken after subtracting background. Results are shown in Figure 2.23, where the error in mean peak fluorescence has been taken from the fwhm of the histogram of each image using the relation FWHM$=2\sqrt{2\ \ln 2} * \sigma$.

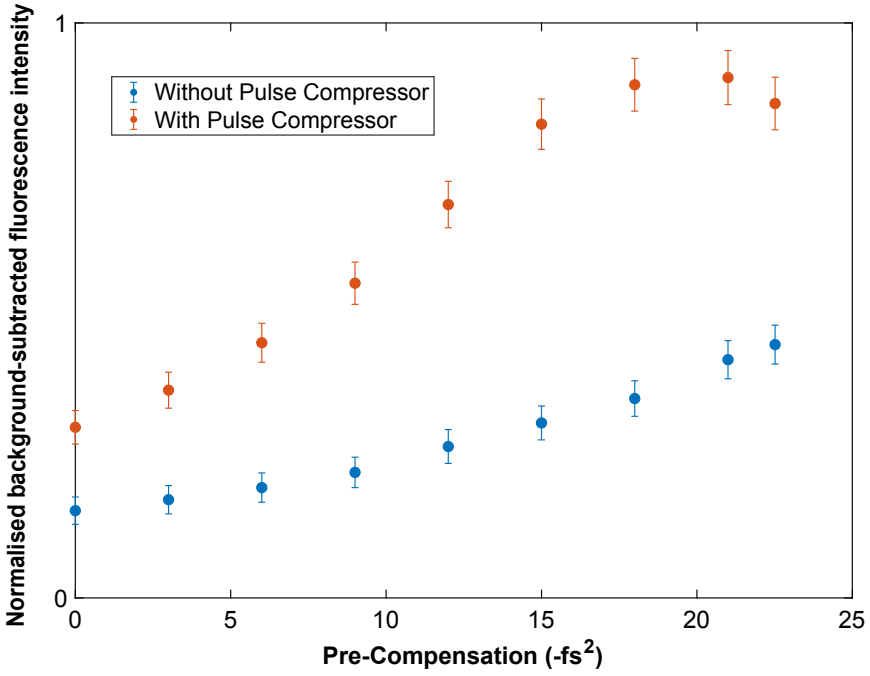

Figure 2.23: Normalised difference in mean measured grey value (subtracting background) of the fluorescence generated by a sample. Data has been taken with changes of the lasers precompensation with and without the custom pulse compressor included. A sample of fluorescein has been excited at 800nm using a constant average power of 8.91mW.

2.4 Discussion

Here I have successfully developed tools for pulse duration management, using a highly dispersive setup to act as a proof of concept. Intensity only autocorrelation offers a cost effective and robust approach to measuring pulse duration. The inclusion of the photodiode from Hamamatsu also allows the resolution of pulses at higher wavelengths up to around 1400nm, future proofing the setup to an extent. With the compartmentalised development of the autocorrelator and its respective software it can easily act independently moving to other setups, shown in future chapters.

The single prism compressor was chosen due to its simple design yet there does seem to be some small unresolved issues in its alignment. But with re-collimation this has been deemed negligible.

3. Three Photon Microscopy

The three photon microscope was built jointly by myself and Dr Ryo Kinegawa.

This chapter focuses on the characterisation of the home-built three-photon system outlining the key challenges that must be addressed to achieve three-photon imaging. Particular attention is given to the operation of the optical parametric amplifier used to generate longer wavelengths, including how its spectral output has been customised. Also discussed are methods for estimating the system's point spread function (PSF) and an example of biological imaging to illustrate system performance is presented.

3.1 Ultrafast Lasers for Three Photon Microscopy

The development of practical three-photon microscopy has been closely linked to advances in ultrafast solid-state laser technology. Early implementations of multiphoton microscopy were limited by the availability of laser systems capable of delivering the high peak powers required for nonlinear excitation while maintaining sufficient average power and stability for biological imaging [21, 42].

Recent progress in ytterbium-based solid-state lasers and fibre-seeded amplifier systems has enabled the generation of high-energy femtosecond pulses with aver-

age powers exceeding tens of watts. These systems provide excellent beam quality, long-term stability, and efficient pumping architectures, making them well suited for nonlinear imaging applications. In particular, the widespread adoption of Yb:KGW and Yb:YAG based laser platforms operating near 1030 nm has enabled efficient pumping of optical parametric amplifiers (OPAs), allowing access to the longer excitation wavelengths required for three-photon excitation.

An additional enabling factor has been the availability of adjustable repetition-rate laser systems. Unlike conventional two-photon microscopy, where repetition rates of 80MHz are common, three-photon excitation benefits from substantially lower repetition rates in the range of 1–4MHz. Reducing the repetition rate increases the pulse energy for a fixed average power, thereby substantially increasing the peak intensity required for efficient three-photon absorption while limiting excessive average power deposition in biological tissue. Consequently, many modern OPA-based systems operate at repetition rates close to 1 MHz after amplification [43].

However, these lower repetition rates also introduce practical limitations. Since fewer excitation pulses are delivered per unit time, imaging speed can become constrained and pixel dwell times must often be increased to ensure sufficient signal generation. In addition, the higher pulse energies associated with low repetition-rate systems can increase the likelihood of nonlinear photodamage, thermal accumulation, and optical component damage if dispersion compensation and beam alignment are not carefully optimised.

Modern ultrafast laser systems also provide improved dispersion control and pulse compression, enabling sub-100 fs pulse durations to be maintained at the sample plane. This is particularly important for three-photon microscopy, where excitation efficiency scales strongly with pulse duration and peak intensity. Together, these

developments in high-power ultrafast sources, repetition-rate control, and dispersion management have transformed three-photon microscopy from a specialist experimental technique into a practical tool for deep-tissue biological imaging.

3.2 Optical Parametric Amplification

As stated previously, longer wavelengths that are required for excitation of fluorophores generally have to be generated via parametric amplification. Here we use Optical Parametric Amplification (OPA) to generate the required wavelength.

Optical parametric amplification is a nonlinear optical process in which a high-energy pump photon and a lower-energy seed photon interact within a material exhibiting strong second-order ($\chi^{(2)}$) nonlinearity. Figure (3.24) illustrates how the pump photon transfers energy to the signal photon through a three-wave mixing process, resulting in the amplification of the signal and the simultaneous generation of a third photon, called the idler. The combined energy of the signal and idler equals that of the pump photon, ensuring energy conservation. In this way, the signal is amplified, and a corresponding idler photon is produced. Any change applied to the signal photon consequently affects the idler photon generated, following the relation given in Equation (3.26):

$$\frac{1}{\lambda_p} = \frac{1}{\lambda_s} + \frac{1}{\lambda_i} \tag{3.26}$$

Where λ_p is the pump wavelength (in this case 515nm (1030nm/2)), λ_s is the signal wavelength and λ_i is the idler wavelength. In our setup, the pump wavelength, λ_p, is fixed at 515 nm.

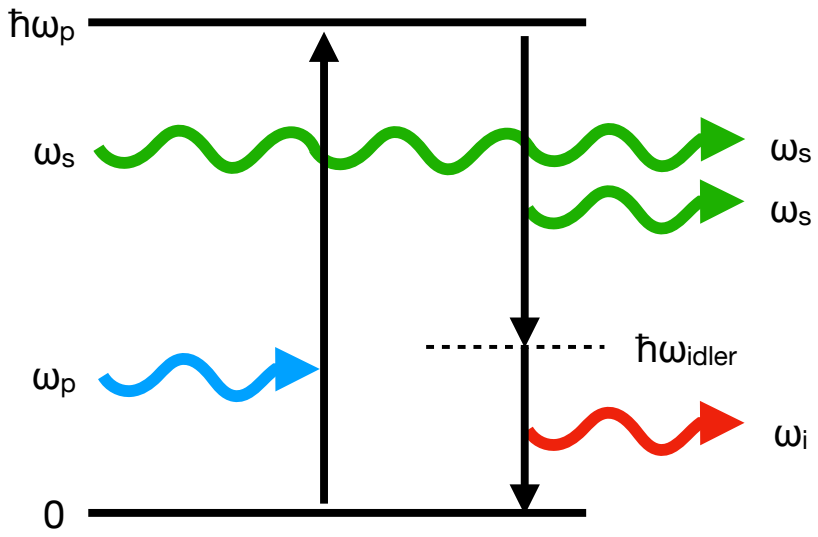

Figure 3.24: Jablonski diagram illustrating three-wave mixing, where pump and signal photons interact in a material exhibiting strong $\chi^{(2)}$ nonlinearity to generate the idler wavelength.

Adjustments to the spectral output and the output power of the OPA are mainly achieved by tuning three key parameters:

- The phase delay applied to the white light (WL) generated during the white light generation (WLG) stage.
- The temporal delay of the WLG beam.
- The phase-matching conditions at amplification stages 1 and 2.

These adjustments allow control over the central wavelength and bandwidth of the amplified signal. The main components and tuning stages of the Orpheus-F system are summarised in the flowchart shown in Figure (3.25).

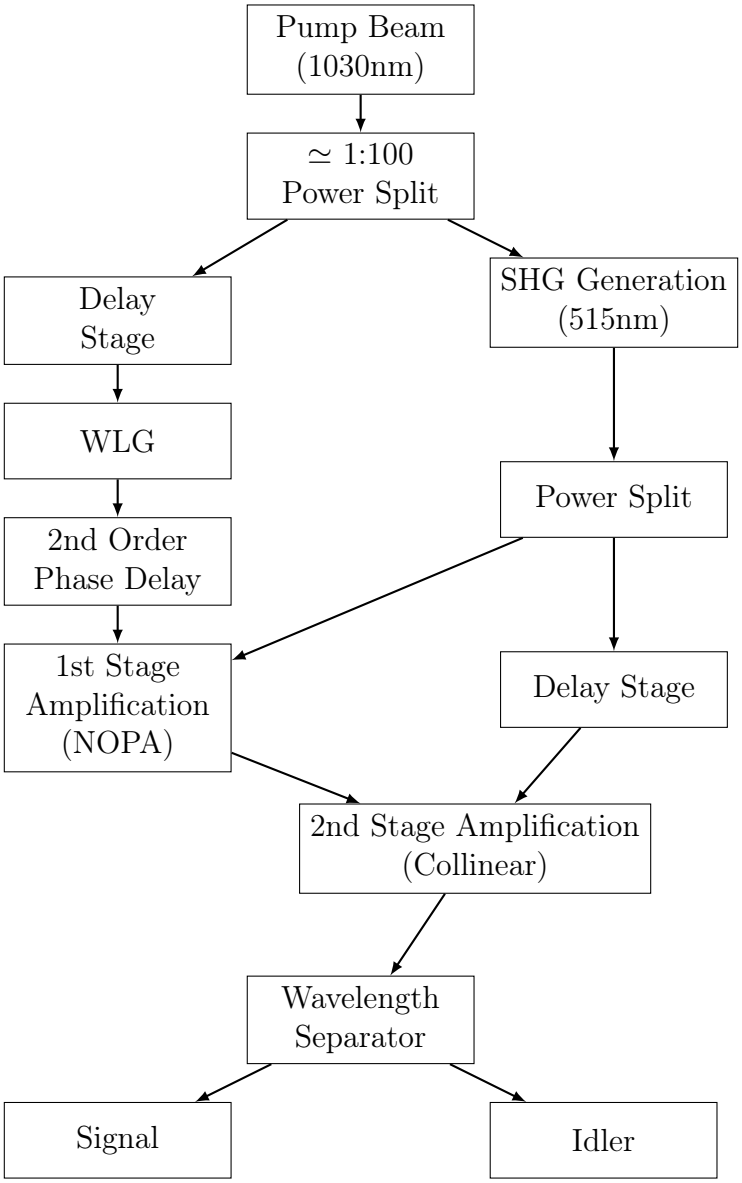

Figure 3.25: Flowchart of the operation of the Orpheus-F Optical Parametric Amplifier (OPA) from Light Conversion. The 1030 nm pump beam from the Light Conversion Carbide is split, with ∼1% applied to a white light generation (WLG) crystal (likely sapphire) to produce a broadband signal. Most of the pump energy is frequency-doubled to 515 nm (SHG), with ∼10% used in the first stage and the remainder sent to the second stage after a first-order phase delay. A second-order phase delay is applied to the white light beam before it overlaps with around ∼10% of the SHG beam in the first amplification stage. A delay stage is applied to the remainder of the SHG beam before overlapping the result of the 1st stage signal at the second amplification stage. The resulting Signal and Idler beams are then separated using dichroics.

First, the 1030nm, 270fs, 40W average power beam from the pump source is split, with approximately 1% of the total pulse energy (around 0.4µJ) directed to generate white light. A second-order phase delay—group delay dispersion (GDD)—is then imposed on the white light, effectively stretching its temporal profile and modifying its spatial overlap. This white light (WLG) beam is subsequently overlapped with the pump beam in the first amplification stage, where optical parametric amplification occurs.

In this first stage, non-collinear optical parametric amplification (NOPA) is employed. By introducing a small angle between the pump and seed beams (white light in this case), a broader spectral bandwidth can be amplified compared to collinear configurations. The use of a crystal with broad phase-matching characteristics further supports this bandwidth extension. This likely explains the design choice in the Orpheus-F system, which aims to produce spectrally broad pulses with short durations.

Additional dispersion can be introduced via a white light delay (WLD) stage, where the white light passes through material with higher GDD. This selectively stretches components of the white light, altering which spectral portions are amplified and thus shaping the bandwidth of the output.

The amplified beam is then passed into the second amplification stage, which typically uses a collinear configuration. Collinear OPA provides narrower spectral amplification but better spatial coherence. A delay stage is incorporated in the pump path here to optimise temporal overlap between the pump and seed beams in this second stage.

Finally, the Signal and Idler beams are separated using a wavelength separator (WS), which employs dichroics or bandpass filters to direct the outputs to their respective optical paths.

To adjust the spectral bandwidth of the OPA output, the primary method is to modify the white light delay (WLD) stage by selecting different dispersive materials. Our Orpheus-F system was supplied with three WLD substrates, each offering increasing levels of group delay dispersion (GDD) applied to the generated white light. As previously discussed, our aim is to achieve the narrowest possible spectral bandwidth, which corresponds to better-defined excitation wavelengths. To that end, the most dispersive WLD substrate was selected for use.

A comparison between the three WLD substrates is shown in Figure (3.26). The three output FWHM are 114nm, 74nm and 30nm for WLD 1,2,3 respectively, giving a clear separation between each delay available. Note that the spectra from WLD1 and WLD2 have been shifted for comparison purposes. These shifts arise due to software-controlled changes made via the OPA presets, which indirectly influence the central wavelength. As a result, small inaccuracies in the actual central wavelengths can occur when tuning through software adjustments alone. Additional dispersive substrates could potentially be introduced to reduce the spectral bandwidth further, although this would need to be tested experimentally.

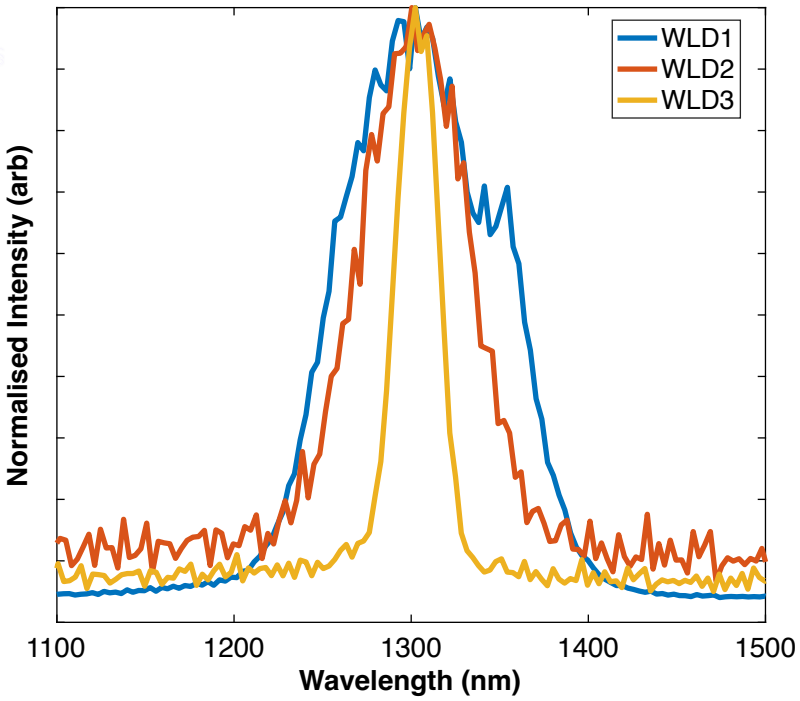

Figure 3.26: Comparison between the three WLD substrates taken with all three presets set to 1300nm, here WLD1 & WLD2 have been laterally shifted slightly to allow for a better overlap. Here a substantial reduction in our spectral bandwidth is shown with; $\text{FWHM}_{\text{WLD1}} \simeq 114\text{nm}$, $\text{FWHM}_{\text{WLD2}} \simeq 74\text{nm}$ and $\text{FWHM}_{\text{WLD3}} \simeq 30\text{nm}$. Data acquired using NIR Quest 256-2.5, Ocean Optics.

3.3 Design

The three-photon microscope developed for this work follows the general design principles of multiphoton imaging systems, as outlined in Section 1.2. The overall optical layout is shown in Figure 3.27.

Two laser sources are integrated into the system: a Coherent Axon 1064 TPC and a Light Conversion Carbide with Orpheus-F optical parametric amplifier (OPA). The Axon 1064 TPC operates at an 80 MHz repetition rate and delivers pulses of approximately 140 fs duration, serving as the excitation source for two-photon imaging. The Carbide–Orpheus-F OPA provides the longer-wavelength pulses required for three-photon excitation, producing around 2W average power (1300nm) at a 1 MHz repetition rate. To compensate for dispersion, the three-photon beam is directed through a Cronus two-prism pulse compressor (Light Conversion) before entering the main optical path.

The compressed beam passes through a series of optical components, beginning with a half-wave plate (HWP, Thorlabs) and a Glan–Thompson polarising beam splitter (Thorlabs GTH10M). Source combination and separation are achieved using a long-pass dichroic mirror (Thorlabs DMLP1180T). Pulse duration and quality are characterised using an APE Mini TPA/PD autocorrelator (APE) coupled to a G1115 photodiode (Hamamatsu Photonics).

Beam expansion and relay are provided by two plano-convex lenses, LB4821-C (f = 100 mm, Thorlabs) and LB4592-C (f = 60 mm, Thorlabs). Beam scanning is performed by a Vidrio Technologies RMR galvanometric scanner, optically coupled to a SL50-3P scan lens (f = 50 mm, Thorlabs) and a TL200-3P tube lens (f = 200 mm, Thorlabs). The specimen is mounted on an MPM250 XYZ stage (Thorlabs) with a PLSXY substage (Thorlabs), both controlled by an MCM301 motion controller (Thorlabs). Fine axial positioning is achieved with a P-721 Pifoc piezo stage (Physik

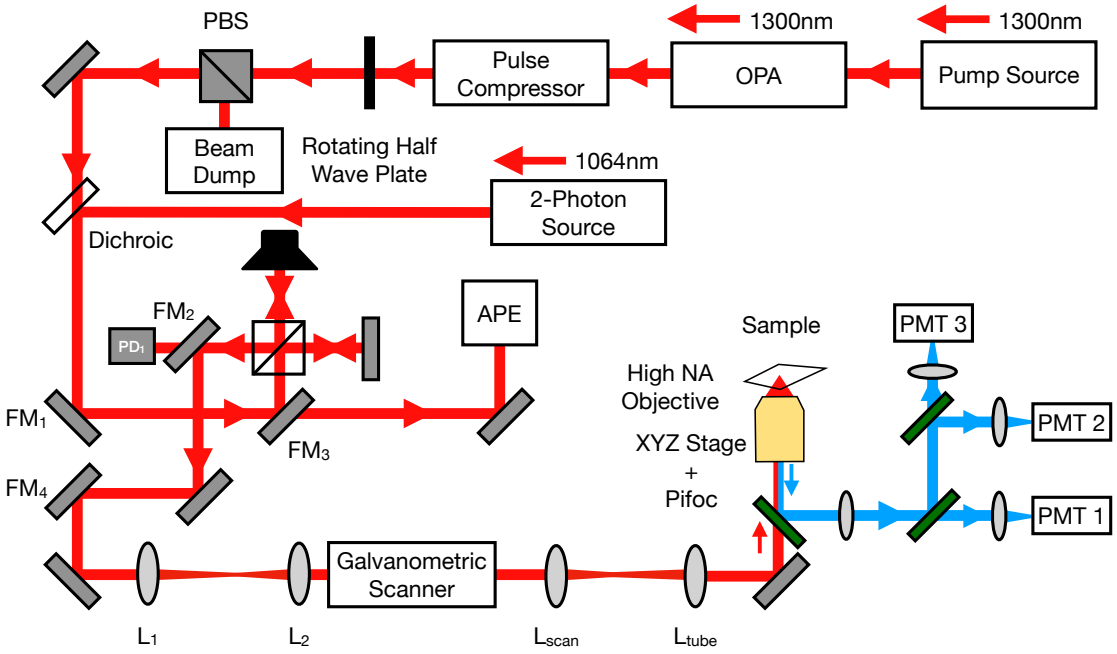

Figure 3.27: Three-photon microscope layout. Flip mirror 1/4 (FM_1/FM_4) are used to initiate pulse measurement where the APE (mini TPA/PD autocorrelator from APE) is used to measure the pulse duration

Instrumente, PI).

Excitation light is focused into the specimen using a Nikon N40XW-PF water immersion objective (40×, NA = 0.8, Nikon Instruments). The transmission efficiency of this objective at longer excitation wavelengths was confirmed to be suitable for three-photon imaging. The sample is mounted as an inverted microscope with fluorescence collected in the epi-direction and separated into multiple detection channels. Detection is achieved using three H11706 series photomultiplier tubes (Hamamatsu Photonics; models H11706-40 and H11706-40-01).

Microscope control is implemented via vDAQ from MBF Bioscience, operated through the controlling software ScanImage (MBF Bioscience) in MATLAB. A flip mirror (FM) allows the excitation beam to be directed into the autocorrelator path for pulse measurement. In typical imaging experiments, a pixel dwell time of 1000 ns is used in ScanImage. This value was chosen to match the 1 MHz repetition rate of the three-photon excitation source, ensuring that each pixel receives approximately one laser pulse.

3.4 Detection

Efficient fluorescence detection is essential in three-photon microscopy, as the signals are typically weak and distributed across several spectral bands. In this system, emitted light is collected in the epi-direction by the objective and directed into a dedicated detection pathway, illustrated schematically in Figure 3.28.

Relay lenses L_3 and L_4 reimage the collected fluorescence onto the active areas of the photomultiplier tubes (PMTs), maintaining signal throughput. To suppress back-reflected excitation light, a primary low-pass filter (F_0) is placed at the entrance of the detection path. The remaining fluorescence is then spectrally separated by a

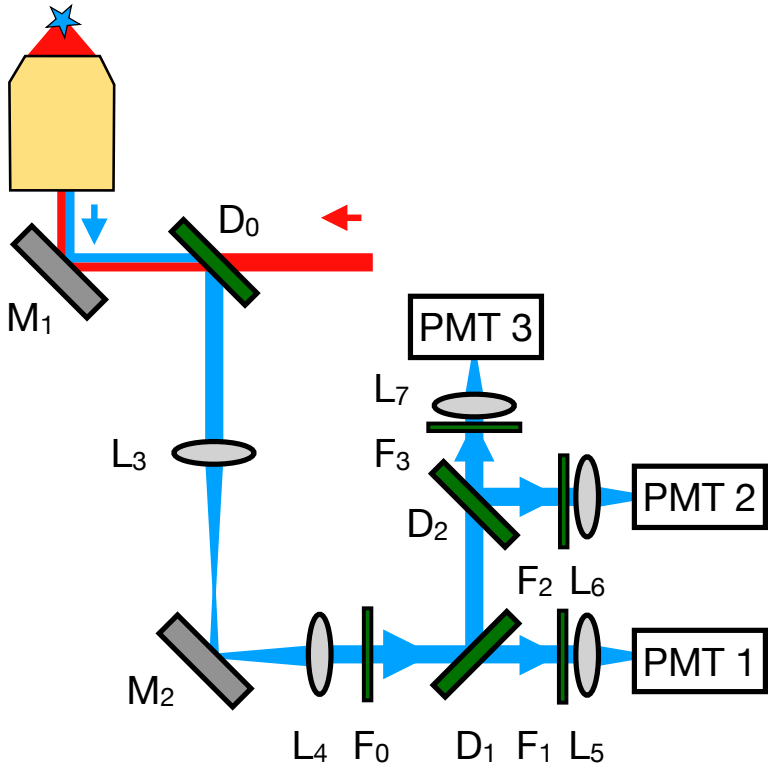

Figure 3.28: Schematic of the detection pathway for the three-photon microscope. Fluorescence is relayed, spectrally separated, and directed onto individual PMTs.

series of dichroic mirrors and bandpass filters, which divide the emission into discrete channels for simultaneous multi-colour imaging.

One example filter and dichroic configuration is listed in Table 3.1. In this arrangement, fluorescence is divided into three detection channels corresponding to blue, green, and red bands. This enables simultaneous detection of nuclear dyes, fluorescent proteins, and non-linear signals such as second-harmonic generation (SHG).

The effectiveness of this detection scheme is demonstrated in Figure 1, which shows a spheroid sample imaged using the configuration described in Table 3.1. Strong DAPI fluorescence is detected in the blue channel, while non-linear SHG is

Label	Component	λ Range (nm)
F_0	Short Pass at 850	Below 850
F_1	525/50, (Chroma)	500 - 550
F_2	FF01-650/13 (Semrock)	643.5 - 656.5
F_3	FF01-590/36 (Semrock)	572 - 608
D_1	FF556-SDi01 (Semrock), Short Pass	< 556
D_2	FF625-SDi01 (Semrock), Long Pass	> 625
PMT 1,2,**3**	Hamamatsu H11706-40 + **H11706-40-01** (GaAsP)	300 - 720

Table 3.1: Filter and dichroic configuration for a three-channel detection scheme.

simultaneously recorded, highlighting the ability of the system to capture multiple signals in parallel.

3.5 Characterisation

3.5.1 Power Measurement

Excitation power at the sample is controlled using a half-wave plate (HWP) and polarising beam splitter (PBS) arrangement. In ScanImage, this control is implemented as a percentage scale (0–100%), where 100% corresponds to the maximum transmission achievable with the HWP–PBS combination. However, for quantitative values it is necessary to convert this relative percentage scale into absolute power values at the sample. This is especially important when converting between WLD 1&3, since they will have different powers and therefore cannot be expressed as equated percentages.

To establish this calibration, power was recorded across the operational wavelength range of the OPA using a Thorlabs S122C Germanium photodiode connected

to a PM100D power meter. The detector provides reliable measurements up to 40 mW between 700 and 1800 nm. Measurements were taken in 2% increments of the ScanImage control until the detector's maximum measurable power was reached. Beyond this point, the relationship between percentage transmission and absolute power was extrapolated by applying a linear fit to the acquired data in MATLAB. This model was then used to estimate the maximum power corresponding to 100% transmission at each wavelength.

Figure 3.29 shows the measured and extrapolated values of maximum power as a function of wavelength. The shaded regions indicate spectral ranges where prism compressor pre-compensation could (red) or could not (blue) be applied, determined by the acceptance limits of the dispersion compensation system.

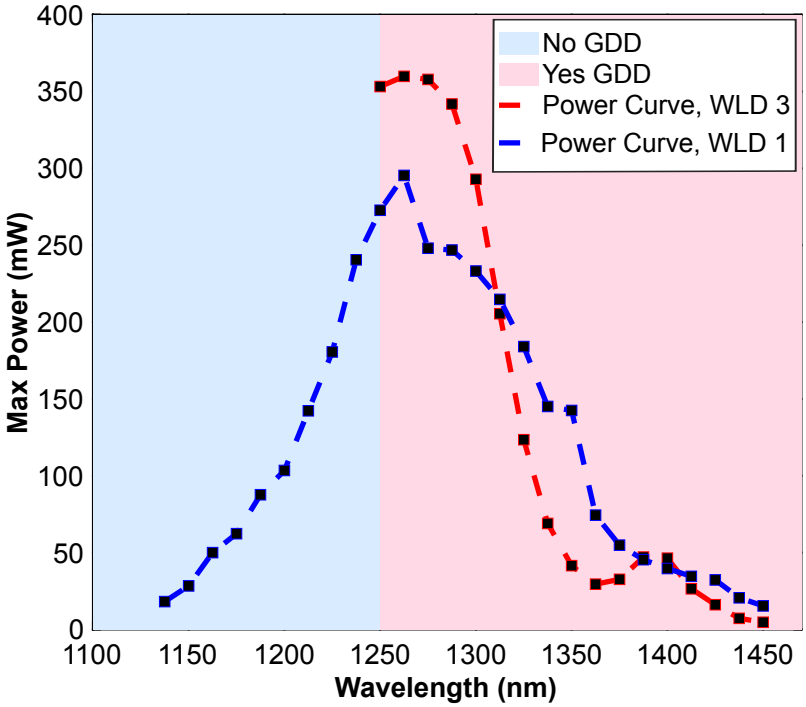

Figure 3.29: Power dependency when operating the OPA in WLD 1 and WLD 3. Measured and extrapolated maximum powers are shown as a function of wavelength, enabling conversion from the percentage scale in ScanImage to absolute power (mW) at the sample. Shaded regions indicate wavelengths where prism compressor pre-compensation could (red) or could not (blue) be applied.

3.5.2 Pulse Dispersion

Having established the relationship between applied power and delivered power at the sample, we next characterised the variation of pulse duration with wavelength and applied precompensation. The objective was to determine the optimum precompensation required to achieve the shortest possible pulse at each excitation wavelength, a vital requirement for boosting three photon signal. Here we will attempt to achieve the shortest pulse duration available, therefore selecting the white light delay 1 (WLD 1) setting on our OPA. These settings have the property of the most broad spectral

output, therefore in accordance with the time-bandwidth limit should be able to give the shortest pulse once properly compensated.

To achieve this, the intensity-only autocorrelator developed in Chapter 1.6 was integrated into the three-photon microscope [37], as shown schematically in Figure 3.27. In parallel, a commercial autocorrelator (APE-TPA) was employed. By taking a measurement of the pulse in the same location as photodiode a timebase for the autocorrelation trace was created and used at the focal plane. This approach both accelerated data acquisition and improved accuracy, eliminating the reliance on mechanical translation stages to retrieve pulse durations.

According to the manufacturer, the APE-TPA autocorrelator has a nominal error of 3.3×10^{-2} fs. This value appears unrealistically small, so we conservatively assume an uncertainty of 0.5 fs, corresponding to half of the device's time resolution. The dominant remaining source of error arises from optical differences between the pulse measured at the photodiode (when FM_1 is engaged) and that measured directly at the APE-TPA.

For each applied value of precompensation, traces were acquired simultaneously at photodiode PD_1 and the APE-TPA, with reference to Figure 3.27. These were compared by forming a timebase factor

$$T = \frac{\mathrm{APE}}{\mathrm{PD}_1},$$

expressed in femtoseconds, under the condition that both measurements were acquired with the same arbitrary oscilloscope timebase. This calibration was then used to recover the pulse duration measured by the photodiode when placed at the microscope focal plane.

The dependence of pulse duration on applied group-delay dispersion (GDD) for

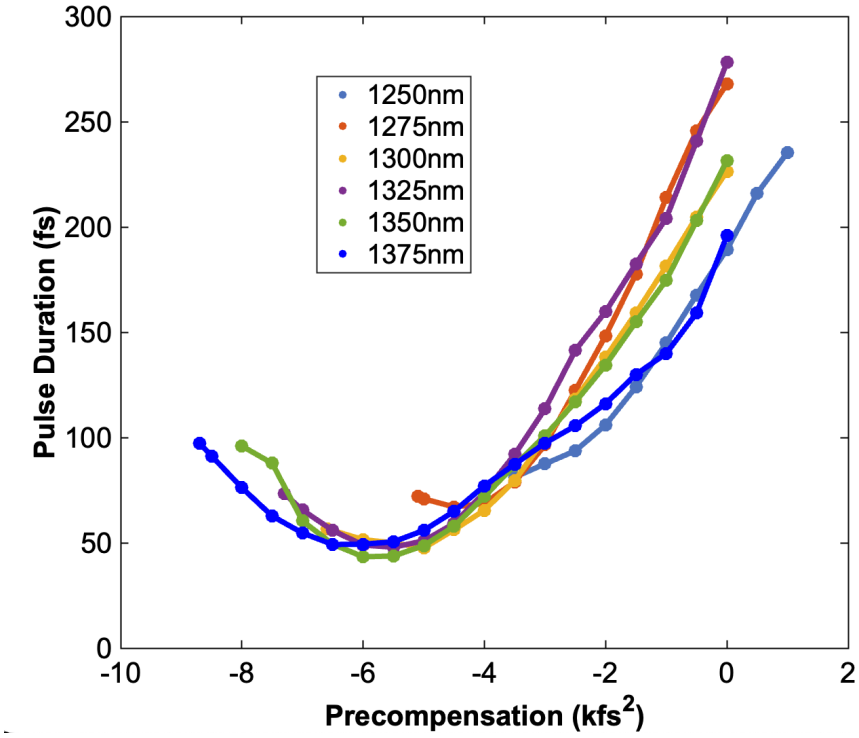

Figure 3.30: Wavelength-dependent pulse duration with varying precompensation applied by the prism compressor. Errors are omitted for clarity.

representative wavelengths is shown in Figure 3.30. In all cases, negative precompensation initially shortens the pulse until a minimum is reached, after which further precompensation broadens the pulse again due to over-compensation. An exception occurs at 1250 nm, where the available pulse compressor range was insufficient to achieve full compression.

The minimum pulse duration achievable at each wavelength is summarised in Figure 3.31. Error bars are derived from the standard deviation across 25 repeated measurements (with outliers discarded), combined with the 0.5 fs uncertainty assigned to the APE-TPA. These results provide a quantitative basis for selecting the optimal amount of precompensation at each operating wavelength.

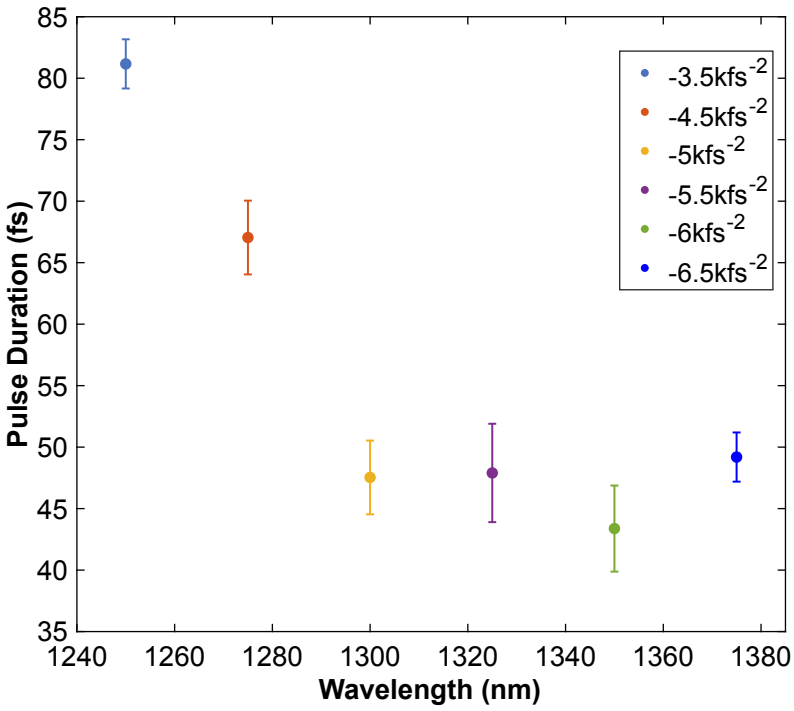

Figure 3.31: Shortest pulse duration at the sample as a function of excitation wavelength. The corresponding precompensation values applied by the prism compressor are indicated in the legend.

3.5.3 Power Dependency

To confirm that we are indeed achieving two and three photon excitation a power measurement is taken [24]. This aims to ramp the power in uniform increments and record the nonlinear increase in power. Following that $P_n \propto I^n$ our nonlinear mechanism can be characterised though taking the log of measured power against applied power as described in 3.27:

$$n \approx \frac{\mathrm{Log(P)}}{\mathrm{Log(I)}} \tag{3.27}$$

Therefore to verify that we are indeed able to excite fluorophores with two and three photons two samples were made with a peak excitation of approximately 1300nm/3 & 1300nm/2. For the 3 photon this corresponded to 4µm Dragon Green beads from Bang Labs (FSDG006). For a 2P sample 4µm Flash Red (FSFR006) beads from Bang Labs were selected, each has a peak excitation of 480nm and 660nm respectively.

Three-dimensional suspensions were prepared by dispersing 4µm green beads into an agar solution comprised of 1% agar (05040-250g, Sigma Aldrich) and 99% di-ionised water. This mixture was cast into custom 3D-printed moulds (1.5 cm × 1.5 cm × 5 mm, ≈ 1 mL volume) and cured. This volume of beads in agar is then mounted onto a cover slip and imaged from below. The same preparation was then made for the 2 photon process at 1300nm.

The samples were imaged with increasing excitation power taking 10 averages with a dwell time of 1000ns, 0.7V PMT biasing with an excitation wavelength of 1300nm using -5kfs^2 precompensation. The resulting images were then assembled into a stack, minus the background and analysed in ImageJ. A region of interest around the centre of a bead was taken, measuring the mean pixel value minus a dark

reading. The natural logarithmic of this and the power applied to the sample was then fitted with a line of best fit applied via least squares method.

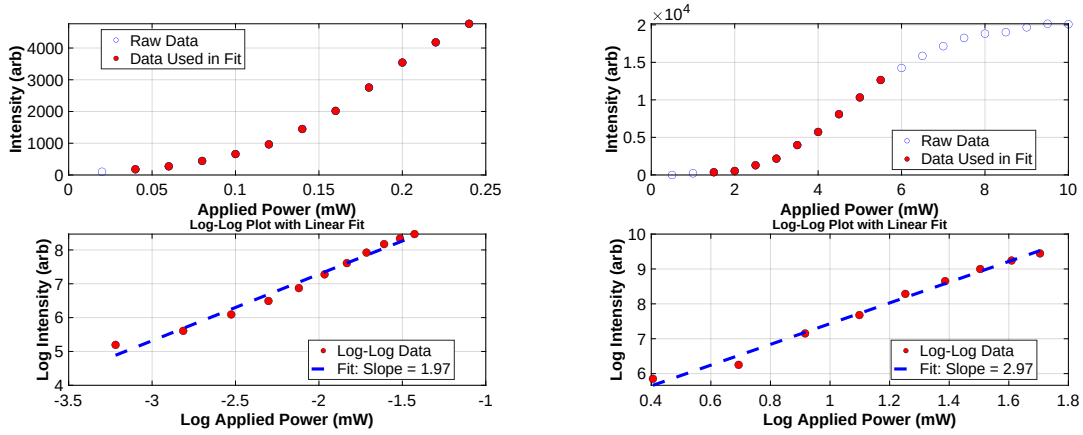

A **B**

Figure 3.32: **A**: Confirmation of two photon excitation, **B**: confirmation of three photon excitation

Figure 3.32 shows the results for both two and three photon excitation at 1300nm. Results show approximate values close to the expected values of 2&3, confirming the presence and distinction of two and three photon excitation.

3.5.4 Resolution Measurements

To assess the resolution capability of the microscope, we imaged sub-diffraction fluorescent beads [14]. According to the relation derived by Zipfel (Equation 1.4) [5], the theoretical point spread function (PSF) for our system (NA = 0.8, $\lambda = 1300$ nm) is $\omega_{x,y} = 0.37$µm and $\omega_z = 1.86$µm. Testing was initially done with beads that were 0.2µm in diameter, since this is approximately half the value derived using Zipfel's equation. However data taken was found not to give reliable results, therefore an

increase in bead size was made and fluorescent beads of 0.4µm diameter were selected.

The same protocol used in section 3.5.3 was used with 0.4µm Dragon Green beads (BangLabs, FCDG004) in an Agar concentration of 20µL per mL into 1% agar solution (05040-250g, Sigma Aldrich). Image stacks were acquired by translating the focus axially using a piezo objective positioner (pifoc), which offers superior precision compared with stage translation.

Initial stacks revealed an axial resolution far worse than predicted, with ω_z extending up to $\approx$ 15µm. Two factors contributed to this degradation: (i) optical tweezing [44] of beads at higher excitation powers, visible as lateral displacements between successive frames, and (ii) under-filling of the objective back focal plane (BFP) [45], which effectively reduces the system NA. To reduce tweezing artefacts, excitation power was lowered and multiple low-power scans were averaged since this is a power dependent process. However, under-filling of the BFP remained the dominant limitation.

The required beam size to properly fill the back aperture is given by:

$$d_{\mathrm{BFP}} = 2 \times f_{\mathrm{eff}} \times \mathrm{NA} = \frac{2 \times f_{\mathrm{TL}} \times \mathrm{NA}}{M} \tag{3.28}$$

where $\mathrm{d_{BFP}}$ is the back focal plane diameter, f_{eff} the effective focal length of the objective, M the magnification, and $\mathrm{f_{TL}}$ the tube lens focal length (200 mm). For our system this yields a required beam diameter of around 8mm (d = 2 × FWHM).

Beam diameters were measured using a knife-edge method [46] with a motorised translation stage (XR50P, Thorlabs) and a power meter (S122C, Thorlabs). With the initial relay optics ($\mathrm{L_1}$ = 100 mm, $\mathrm{L_2}$ = 30 mm), the effective magnification at the BFP was 1.2, resulting in a beam size of 3.62 mm—well below the required amount. Replacing $\mathrm{L_2}$ with a 60 mm lens increased the magnification to 2.4 and

produced a beam diameter of 7.41 mm.

After correcting for both tweezing artefacts and BFP under-filling, resolution measurements were repeated. An example dataset is presented in Figure 3.33. Images were acquired with 4.7 mW excitation at 1300 nm, applying -5 kfs^2 pre-compensation from the OPA (WLD3). Each frame represents the average of 10 scans with a dwell time of 1000 ns, and axial steps of 0.125µm were applied via the pifoc. Gaussian fits to bead profiles gave average resolutions of 0.93µm (X), 0.89µm (Y), and 3.44µm (Z).

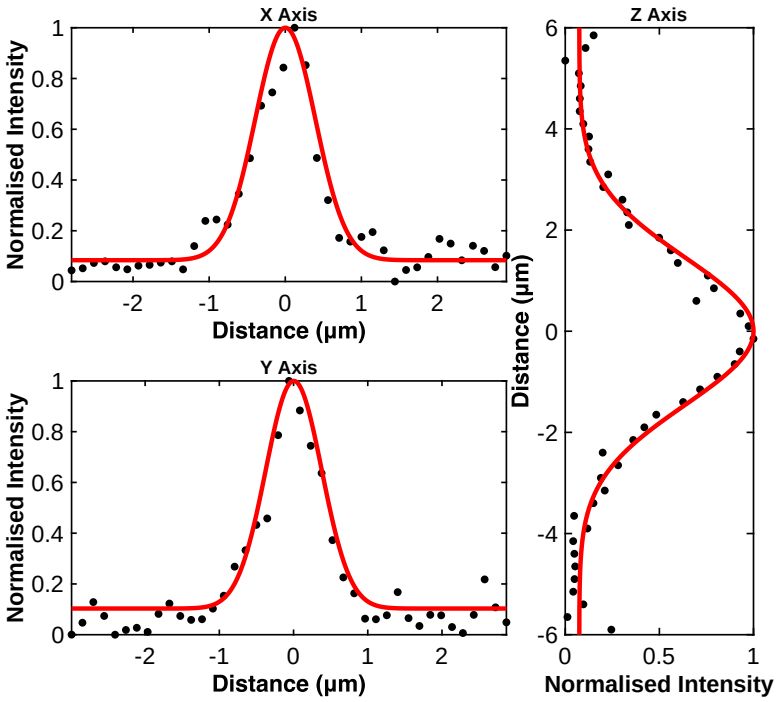

Figure 3.33: Measured lateral and axial resolution of 0.4µm beads imaged at 1300 nm. Resolutions in X, Y, and Z were 0.93 ± 0.10 µm, 0.89 ± 0.10 µm, and 3.44 ± 0.19 µm, respectively.

3.6 Summary

In this chapter, we described the implementation and characterisation of a three-photon excitation microscope based on an inverted epi-illumination. Excitation was provided by an Orpheus-F optical parametric amplifier (OPA, Light Conversion), integrated with a commercial pulse compressor.

We first quantified the relationship between nominal laser power settings and actual power delivered to the sample plane. Although power is adjusted in software as a percentage transmission via a half-wave plate and polarising beamsplitter, absolute power values were established through calibration with a germanium photodiode detector (Thorlabs S122C), ensuring accurate determination of sample irradiation across different wavelengths.

The effect of group delay dispersion (GDD) on pulse duration was then examined using a hybrid autocorrelation method that combined a custom-built intensity autocorrelator with the commercial APE-TPA. This approach provided a reliable time-base without reliance on mechanical delay lines, thereby improving accuracy and acquisition speed. Measurements revealed the wavelength-dependent effectiveness of pre-compensation, identifying the optimal conditions for achieving the shortest pulses at the sample plane.

Resolution was evaluated experimentally using 0.4 µm fluorescent beads embedded in agar. Theoretical limits based on a multiphoton model predicted sub-micron lateral resolution and axial resolution of 1.9 µm. Initial measurements, however, showed degraded axial resolution (15 µm), attributed to optical trapping effects and, more critically, under-filling of the objective's back focal plane. Optical tweezing artefacts were reduced by lowering excitation power, while beam expansion optics were redesigned to ensure proper overfilling of the objective pupil. Following these corrections, measured resolutions of 0.93 µm (X), 0.89 µm (Y), and 3.44 µm (Z) were

obtained at 1300 nm.

Overall, this chapter establishes both the operational parameters and practical limitations of the system. Power calibration ensures accurate sample dosing, dispersion management identifies the wavelength-dependent optimisation required for shortest pulses, and resolution studies reveal the influence of optical alignment and pupil filling on system performance. These findings lay the groundwork for subsequent imaging by defining the achievable spatio-temporal focusing characteristics of the microscope.

4. Imaging Cardiac Organoids with Two and Three-Photon Microscopy

In this study, we aim to image both cleared and uncleared organoids and spheroids in order to investigate their structural organisation in a non-invasive manner.

Understanding how our microscope performs with uncleared organoids and spheroids enables us to move toward functional imaging. A key requirement for this transition is to assess the limitations of imaging depth within the sample. To characterise this parameter, we introduce the concept of the characteristic attenuation length (CAL) while comparing it with some heart tissue from a rabbit heart.

4.1 Spheroids and Organoids

Cardiac research is a time-consuming, complex, and expensive field, posing significant challenges in a laboratory setting. This difficulty largely arises from the limited availability of samples from laboratory-grown animals and the strict time constraints associated with using them once available. Considerable effort is invested in preparing a sample before it can be imaged. To address these challenges, simplified versions of lab-grown organs—known as spheroids and organoids—are employed. These models provide a more accessible means to study tissue behaviour and test various

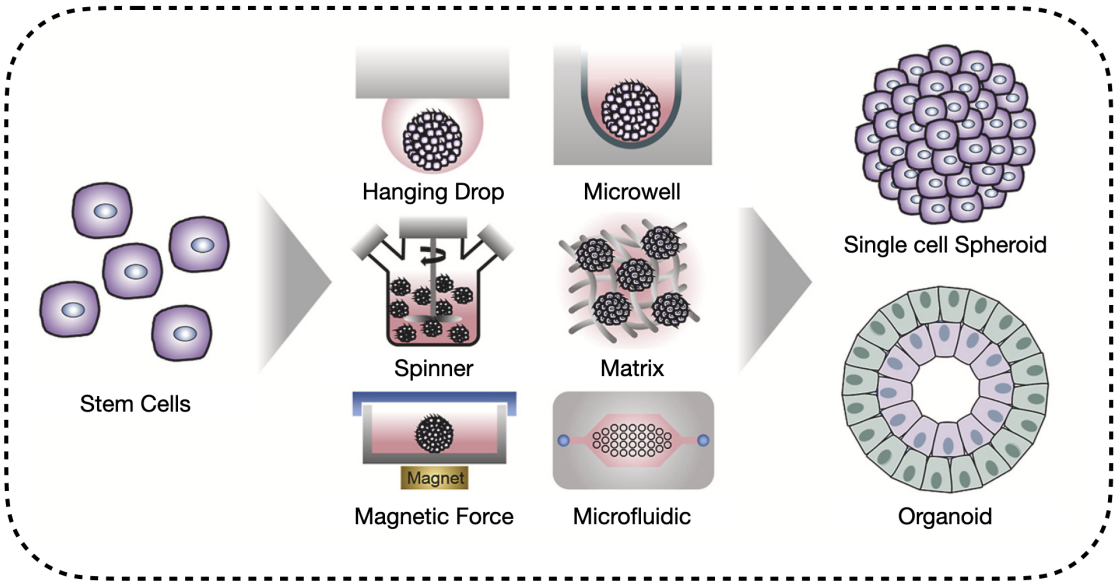

Figure 4.34: Spheroid and organoid generation from a variety of culturing techniques, adapted from [47].

applications.

In principle, spheroids and organoids have applications across a wide range of experimental and clinical research. A straightforward example is drug response modeling [48], which allows standardised drug testing at low cost and with rapid turnaround. Beyond this, they hold potential for applications such as modelling patient-specific diseases [49], where large-scale organoid production has been explored for personalised treatment. Functional imaging of organoids has also been demonstrated [50], which could be extended to multiphoton microscopy, offering a similar level of insight as perfused heart imaging [51, 52].

The distinction between spheroids and organoids lies in their complexity and cellular composition. Spheroids are relatively simple three-dimensional cell aggregates, typically consisting of a single cell type and designed to mimic certain features of tissue. Organoids, in contrast, are more complex, composed of multiple cell types

with the aim of reproducing aspects of organ structure and function [53].

In this chapter, we focus on imaging cardiac spheroids as well as cardiac and heart organoids. Here, a further distinction can be made between "cardiac" and "heart" organoids. Heart organoids in our case are composed of human induced pluripotent stem cell (hiPSC)-derived cardiomyocytes, fibroblasts, and endothelial cells. Cardiac organoids [54], on the other hand, consist primarily of cardiomyocytes but are not as simplistic as spheroids, nor can they be classified as such, since they are differentiated from stem cells—unlike spheroids, which do not necessarily undergo this process [55, 56].

4.1.1 Clearing

To obtain more detailed structural information from our samples, we chose to optically clear a subset or 50% of the samples.

Tissue clearing is a widely used technique that renders biological samples optically transparent, thereby allowing light to propagate through with minimal scattering [57, 58]. In principle, this process preserves the underlying structure while enabling deeper imaging. The main limitation, however, is that the sample becomes non-viable [59], and thus unsuitable for any form of functional imaging.

This method has been successfully applied in previous studies of spheroid samples, where it enabled complete imaging through the sample volume [60, 61]. In our case, the samples were cleared using a simple glycerol solution, which is an effective and practical approach given their small scale.

Since this study is primarily focused on the structural properties of organoids and spheroids, our objective is to assess imaging depth and determine how homogeneous the internal structure is. This information provides valuable insight into their overall organisation and build-up.

4.1.2 Dye Selection

To distinguish between different structures within the cellular build-up of the organoids, we employed two fluorescent dyes during staining. Dual staining is a common practice in microscopy, and in multiphoton microscopy it offers the additional advantage of detecting second harmonic generation (SHG) from non-centrosymmetric molecules. In previous spheroid imaging experiments, we observed a strong SHG signal, which informed our selection of dyes so as to reserve a narrow spectral channel around 650 nm for SHG detection.

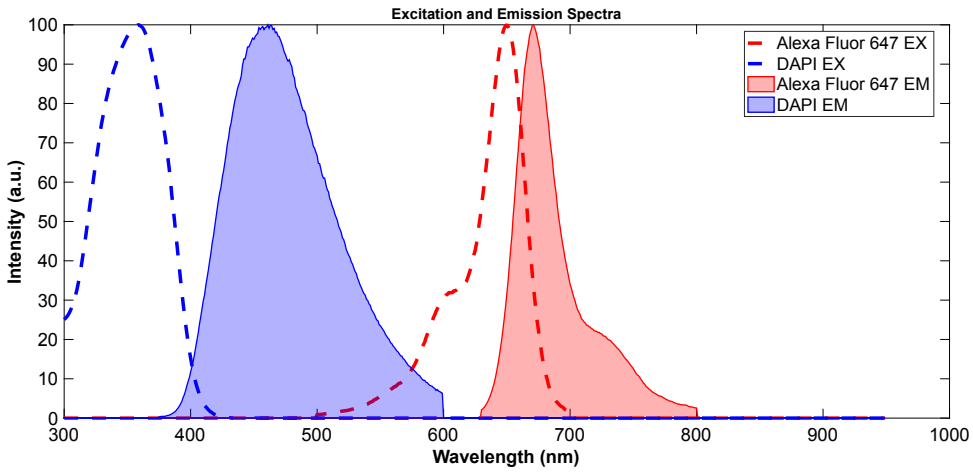

Figure 4.35: Dyes selected for use in organoid imaging. EX: excitation, EM: emission. Both dyes exhibit a characteristic Stokes shift. Data adapted from [62].

We selected a nuclear stain and a membrane stain to provide complementary structural information, staining the cell nucleus and membrane with separate dyes to contrast the acquired images. For nuclear staining, we used 4',6-diamidino-2-phenylindole (DAPI), which produces a strong signal under three-photon excitation, staining the cell nucleus. In previous imaging rounds, we also observed a red-shifted emission from DAPI, extending into the green spectral region. To minimise spectral overlap, we therefore selected a red-emitting dye for membrane labelling. Specifically,

Label	Component	λ Range (nm)
F_0	Short Pass at 850	Below 850
F_1	525/50, (Chroma)	500 - 550
F_2	FF01-650/13 (Semrock)	643.5 - 656.5
F_3	BLP01-647R-25 (Semrock)	647 - 850
D_1	FF556-SDi01 (Semrock), Short Pass	< 556
D_2	FF659-SDi01 (Semrock), Long Pass	> 659
PMT 1,2,**3**	Hamamatsu H11706-40 + **H11706-40-01** (GaAsP)	300 - 720

Table 4.2: Filters and dichroics used to image WGA-AF647 and DAPI stained organoids. This scheme corresponds to the detection setup shown in Figure 4.36.

we employed wheat germ agglutinin conjugated to Alexa Fluor 647 (WGA-AF647), which effectively labels cell membranes. The "647" denotes the peak excitation wavelength (647nm) under single-photon excitation (see Figure 1).

Based on these dye choices, we designed a filter and dichroic scheme to maximise separation of the emission signals while leaving a spectral gap for SHG detection. This approach is consistent with our earlier spheroid imaging experiments (Figure 1), where strong SHG was observed alongside the three-photon signal. The filter and dichroic configuration is summarised in Table 4.2 and corresponds to the detection layout illustrated in Figure 4.36.

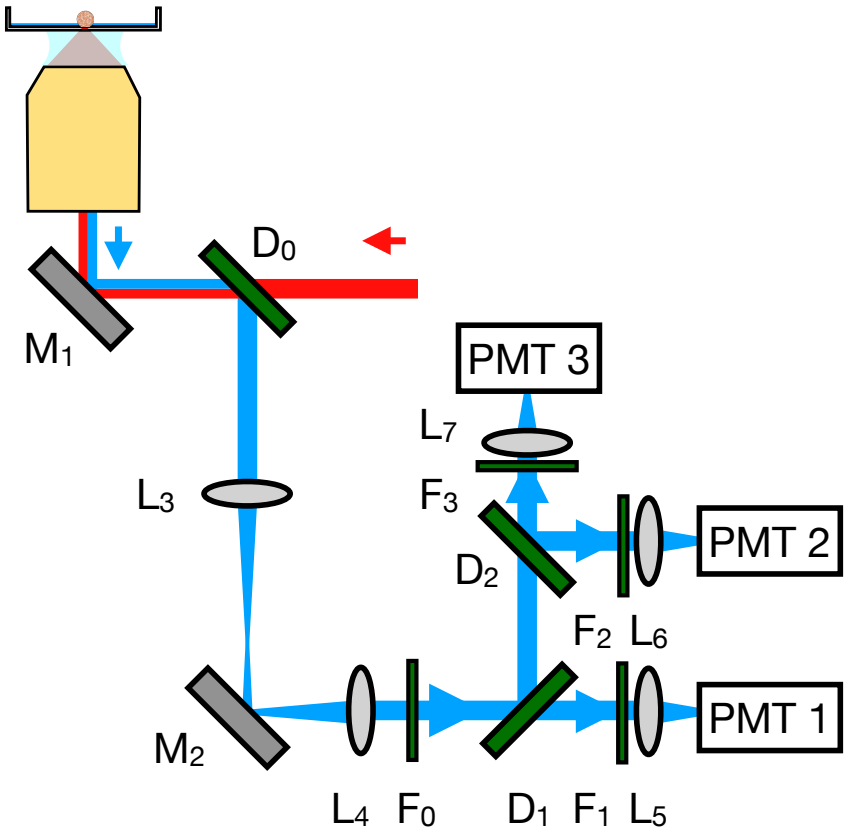

Figure 4.36: Detection setup showing the layout of filters F_1, F_2, F_3, D_1, and D_2.

4.2 Imaging with Multiphoton Microscopy

For this experiment, the WLD 3 presets were used to target the selected dyes. In particular, we employed the most optimal compressor preset, $-3\,\mathrm{kfs}^2$, corresponding to an output wavelength of 1300 nm, 30nm linewidth (FWHM) with a pulse duration of 47fs. These values were kept constant throughout the experiment.

Figure 4.37 shows the complete setup used for organoid imaging. The bright-field imaging system is highlighted, consisting of a white-light LED and a CCD camera to acquire bright-field images of the organoids. For this experiment, the previously used microscope objective was replaced with a higher-NA objective (XLPlan N 25×/1.05, FV1000MPE, Olympus). This objective provides improved optical throughput at higher excitation wavelengths while also enhancing optical sectioning, as discussed in Section 4.2.1.

4.2.1 Microscope Objective

For this experiment, we used the XLPlan N 25×/1.05, FV1000MPE (Olympus) objective. Here, we briefly evaluate the resolution capability of this objective using bead samples. To do so, 1% agarose samples were prepared with sub-resolution beads: 0.194 µm Flash Red beads and 0.4 µm Dragon Green beads (Bang Laboratories), following the procedure outlined in Section 2.4.

With the help of Ahmed Elnageh, the beads were analysed for their full width at half maximum (FWHM) both axially and laterally. A single-order Gaussian was fitted to each bead using custom code to identify and characterise individual beads. This method allowed the calculation of a large number of point spread functions (PSFs) simultaneously. The results are shown in Figure 4.38.

From these measurements, we determined an appropriate step size for imaging.

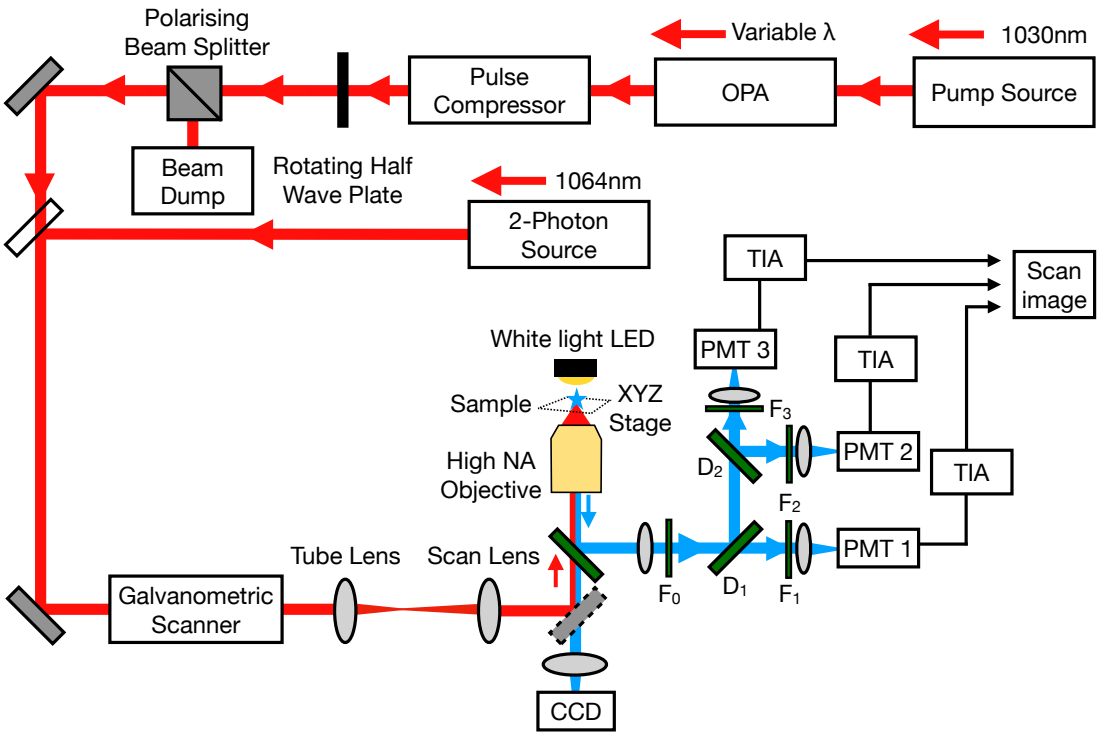

Figure 4.37: Microscope setup used for imaging cardiac and heart organoids. Galvanometric Scanner denotes the Vidrio Rapid Multi Region (RMR) scanner, a hybrid resonant-galvo-galvo (RGG) scan head. By employing an image-relayed mirror configuration, the system can rapidly switch between user-defined regions of interest while maintaining distortion-free beam steering, enabling efficient imaging of multiple selected areas within a sample rapidly.

Given that the axial resolution of the objective is 2.15 µm, we set the imaging step size to 1 µm, corresponding to at most half of the axial resolution.

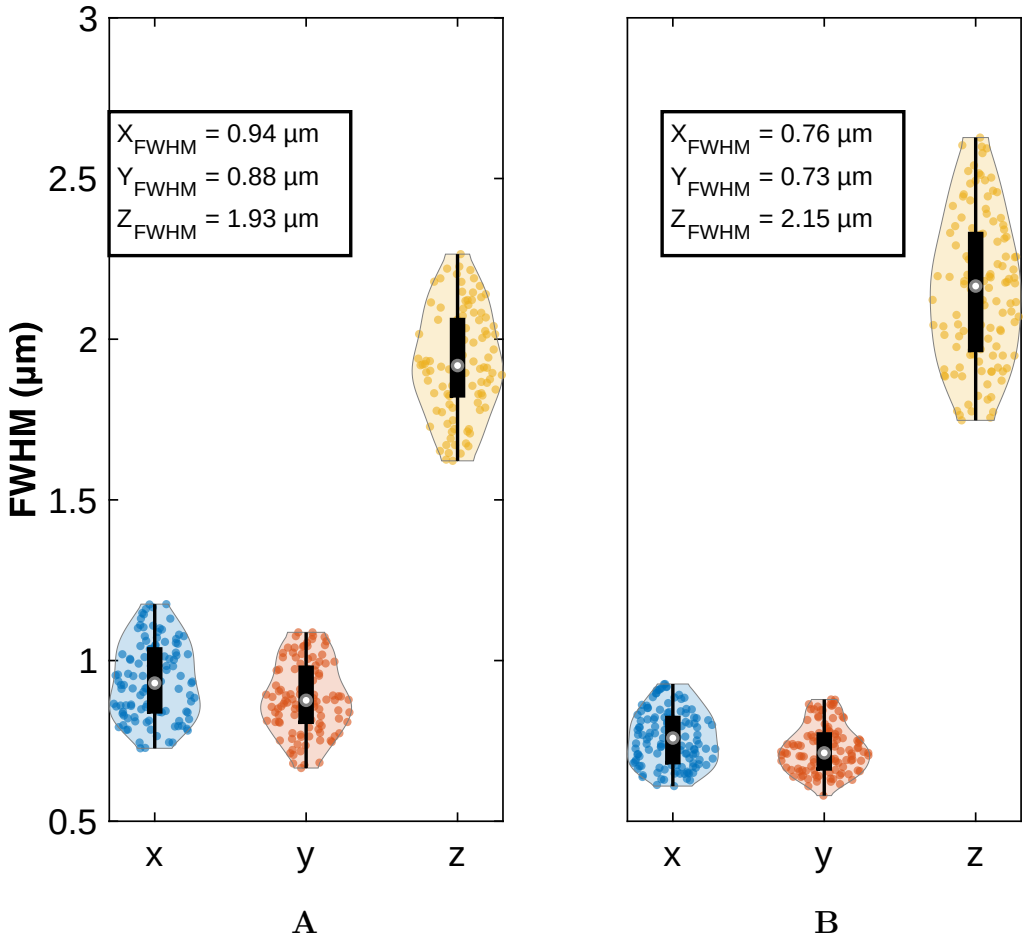

Figure 4.38: XLPlan N 25×/1.05, FV1000MPE (Olympus) used to measure PSFs. **A)** 2-photon case: 0.194 µm Flash Red beads, 111 analysed; **B)** 3-photon case: 0.4 µm Dragon Green beads, 123 analysed.

4.2.2 Imaging

Sample Preparation

The organoids were immobilised in agar within glass-bottom well plates. They are stored in a refrigerator at approximately 3°C when not being imaged.For cleared organoids, glycerol is topped up as needed to maintain optical clarity. For uncleared samples, a HEPES-supplemented solution is used to prevent dehydration and to provide a superior buffering capacity compared to bicarbonate-only systems, which is crucial for maintaining a stable pH.

The organoids were provided in glass-bottom well plates, with each plate containing 2–4 samples, each approximately 200 µm in diameter.

Samples were mounted on the microscope as shown in Figure 4.39. The inverted microscope setup is well-suited for imaging these samples, with the agar providing lateral and axial support. Some sagging of the organoid structure is, however, unavoidable.

Imaging Procedure

Bright-field mode is used to locate the organoid before switching to multiphoton imaging. This is necessary because the organoids are approximately 200 µm in diameter and can be difficult to locate visually or using multiphoton signals alone.

Once the organoid surface (the face closest to the objective) is located, the axial position is adjusted using the stage. Excitation power is then tuned to avoid damaging either the sample or the PMTs. The bottom of the organoid (facing away from the objective) is identified to acquire a full 3D stack. Cleared samples are easier to image completely, whereas non-cleared organoids suffer from increased scattering, limiting penetration.

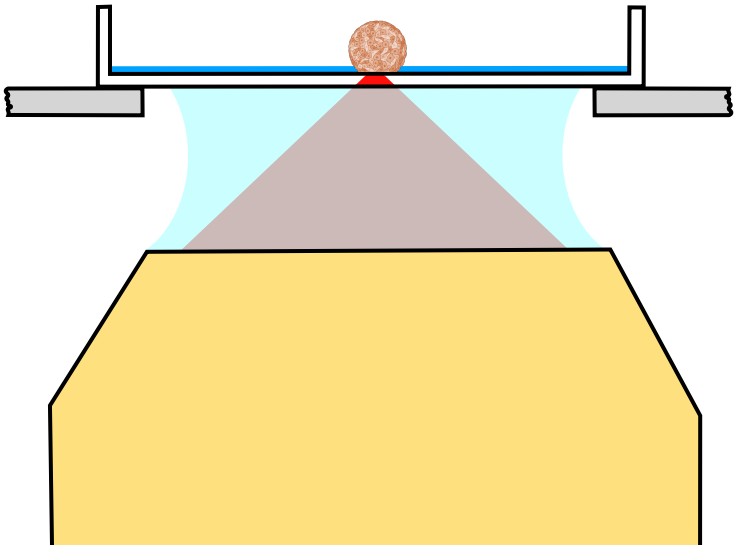

Figure 4.39: Cross-section of an organoid (not to scale) inside a cover glass–bottomed well plate. The organoid sits in a thin layer of agar that "fixes" it. The stage allows movement in 1 µm increments in XYZ.

A significant difference in required excitation power exists between 2-photon and 3-photon imaging—approximately a factor of 10. Consequently, two stacks are acquired sequentially: first the 2-photon acquisition, then the 3-photon. This order reduces the risk of photobleaching or other damage from the higher-energy 3-photon process.

Following the detection setup in Figure 4.36, channels 2 and 3 (PMTs 2 & 3) are used to collect the 2-photon signal, followed by channel 1 (PMT 1) for the 3-photon signal.

The excitation power required to maintain an adequate fluorescence signal increases with imaging depth due to absorption and scattering within the sample. Consequently, depth-resolved image stacks were acquired using a bounded power profile rather than a constant excitation power. This approach applies an exponential increase in laser power between user-defined minimum and maximum values,

reducing the risk of photodamage near the sample surface while preserving signal intensity at greater depths. The power bounds were determined by imaging a single plane near both the top and bottom of the organoid and recording the excitation powers required to achieve acceptable image quality at each depth. These values were then used to define an exponential power ramp within ScanImage, with the profile optimised experimentally based on the measured attenuation characteristics of the organoids.

4.3 Organoid Results

As expected, we observed strong signals in both 2&3 photon imaging modalities. This is evident in the example images shown in Figure 4.40, which display high-quality two- and three-photon images for all samples. Cleared organoids could be imaged throughout the entire sample, whereas uncleared organoids appeared more turbid and highly scattering. Unexpectedly, no strong signal was detected in the SHG channel.

The signal was defined as the mean intensity of the top 1% of pixel values within the organoid. The background intensity was calculated from an annular region located approximately 20,µm from the organoid boundary and with a thickness of 20,µm. Both signal and background intensities were evaluated at each imaging depth to account for depth-dependent changes in image quality.

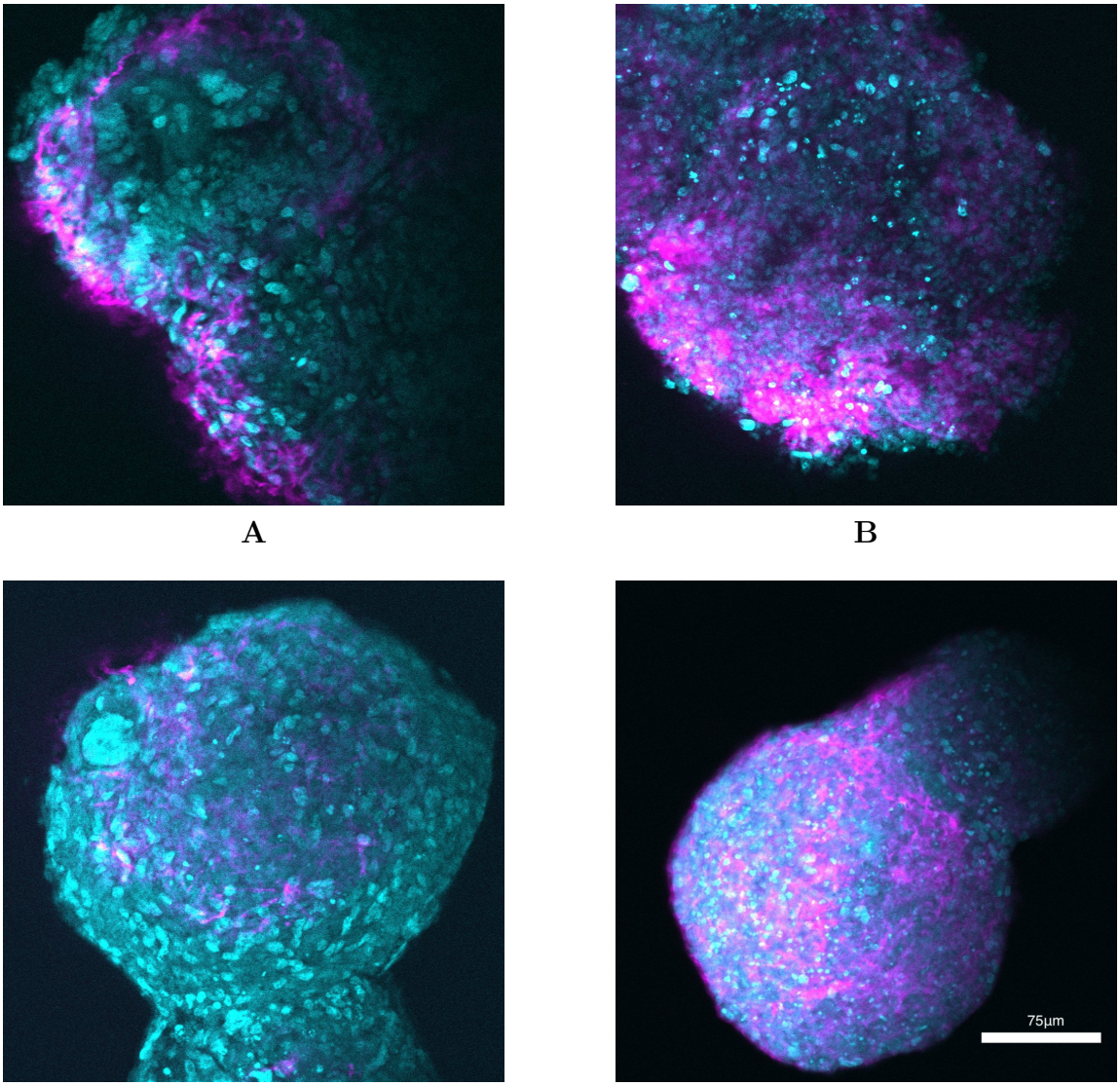

Figure 4.40: DAPI-stained nuclei are shown in cyan, and WGA-647–stained membranes are shown in magenta. **A:** Cleared Heart at depth 329 µm, **B:** Cleared Cardiac at depth 128 µm, **C:** Uncleared Heart at depth 40 µm, **D:** Uncleared Cardiac at depth 99 µm. The scale bar in **D** applies to all samples.

4.4 Analysis

4.4.1 Calculated Attenuation Length

To assess the penetration ability of our microscope within organoids, we measured the calculated attenuation length (CAL) [42] for uncleared organoids. This allows quantification of how effectively signal can be extracted from within the organoid structure. Here, we focus solely on uncleared samples to avoid unrealistic comparisons and to better inform future functional imaging studies with organoids.

By defining CAL as the length over which the generated intensity drops by a factor of $1/e$:

$$I(z) = I_0 e^{-z/\mathrm{CAL}} \tag{4.29}$$

where $I(z)$ is the generated intensity, I_0 is the initial intensity, and z is the imaging depth. Considering that the measured signal is directly proportional to the intensity raised to its respective power law, CAL can be expressed in terms of the measured signal:

$$\text{Signal(z)} \propto I(z)^n = I_0^n e^{-nz/\mathrm{CAL}} \tag{4.30}$$

where Signal(z) is the measured signal as a function of depth z and n is the excitation order of the nonlinear fluorescence process.

Evaluating:

$$\ln\big(\text{Signal}(z)\big) = \ln(I_0^n) - \frac{nz}{\mathrm{CAL}} \tag{4.31}$$

yields an expression for CAL in terms of the signal and the nonlinear excitation process:

$$\mathrm{CAL} = -\frac{n}{\dfrac{d}{dz}\ln\big(\mathrm{Signal}(z)\big)} \tag{4.32}$$

As previously mentioned, bounded stacks are often used for imaging uncleared organoids due to their turbid nature. In this approach, the laser power increases with depth according to:

$$P(z) = P_0 \exp\left(\frac{z - z_0}{L_z}\right) \tag{4.33}$$

where $P(z)$ is the power at imaging depth z, P_0 is the initial power, z_0 is the starting depth, and L_z is the decay constant, here set to 100 µm.

Since $\mathrm{Signal}(z) \propto P(z)^n$, CAL can be expressed as a function of bounded stack power:

$$\mathrm{CAL} = -\frac{n}{\dfrac{d}{dz}\ln\left(\dfrac{\mathrm{Signal}(z)}{P(z)^n}\right)} \tag{4.34}$$

Using this approach, we measured CAL for both two- and three-photon processes in our organoid samples.

Figures 4.41 and 4.42 show the CAL measurements for heart and cardiac uncleared organoids, respectively. Differences in power and grey values are apparent, with both bounded and unbounded measurements yielding similar results.

For comparison, CAL measurements were also performed on uncleared rabbit heart tissue (New Zealand White rabbits). DAPI-stained slices were imaged under identical conditions as the organoids.

All CAL results are summarised in Table 4.3.

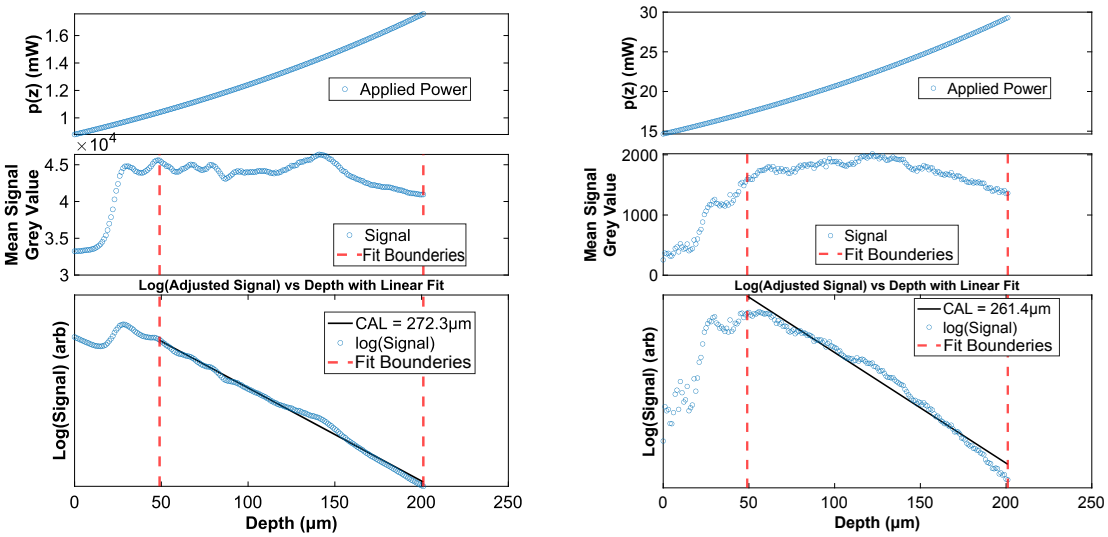

Figure 4.41: Unclear heart organoid CAL measurements. **A:** Two-photon emission, line of best fit $R^2 = 0.9444$. **B:** Three-photon emission, line of best fit $R^2 = 0.9921$.

Sample Type	2 Photon Process (µm)	3 Photon Process (µm)
Heart Organoid	272.3	261.4
Cardiac Organoid	303.5	249.2
Rabbit Left Ventricle	284.9	247.4

Table 4.3: Results of CAL calculations for heart and cardiac organoids, as well as mouse heart tissue, using 1300 nm excitation for both two- and three-photon processes.

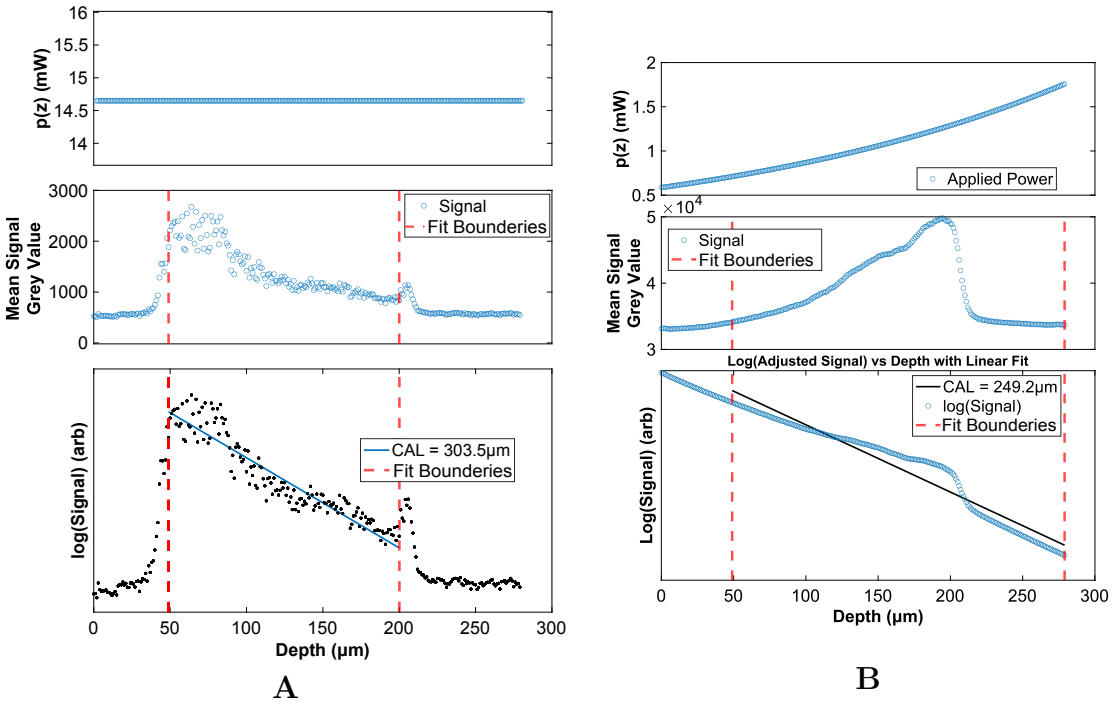

Figure 4.42: Unclear cardiac organoid CAL measurements. **A:** Two-photon emission, line of best fit $R^2 = 0.9938$ **B:** Three-photon emission, line of best fit $R^2 = 0.9748$.

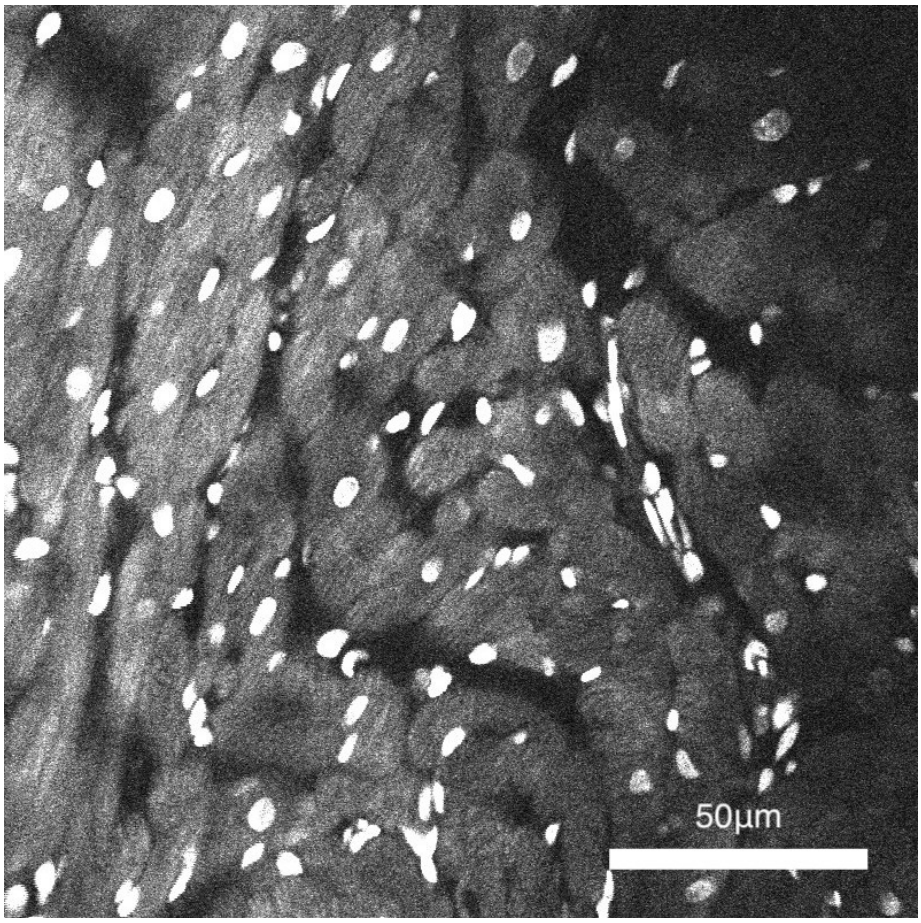

Figure 4.43: DAPI-stained New Zealand White rabbit left ventricle slice imaged at 211 µm depth (uncleared, bounded stack) using 1300 nm excitation with WLD3. Image acquired by Ahmed Elnageh.

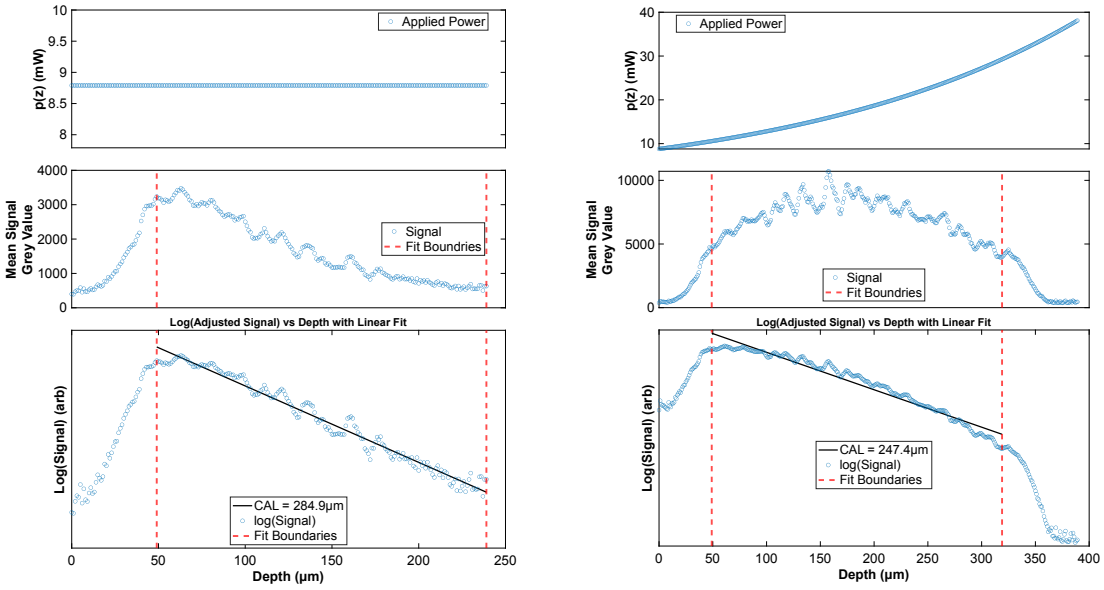

A **B**

Figure 4.44: CAL results for the left ventricle slice shown in Figure 4.43: **A:** Constant applied power $R^2 = 0.9745$. **B:** Bounded stack $R^2 = 0.9554$.

4.5 Discussion

The results shown in Table 4.3 can be compared with literature values summarised in Table 4.5. This comparison shows that the calculated attenuation lengths (CAL) in organoids are comparable to those reported in other biological tissues, mainly mouse brain, under similar three-photon conditions.

Sample	CAL/EAL	Value (µm)	Reference
Mouse Brain: Neocortex	CAL	401	[42]
Mouse Brain: Neocortex	EAL	329/150*	[63]
Mouse Brain: Cortex	EAL	≈ 300	[64]
Mouse Brain: Cortical vasculature	CAL	285	[65]
Mouse Brain: Cortex	EAL	275	[66]
Mouse Brain: External capsule	CAL	229	[42]
Mouse Brain: Cortex	EAL	285	[67]
Mouse Brain: Hippocampus	EAL	250	[66]
Mouse Brain: White Matter	EAL	101	[66]
Mouse: Spinal Cord	CAL	75/50†	[68]

Table 4.4: A list of tissue attenuation lengths for respective media in three-photon microscopy (unless otherwise stated) using wavelengths around 1300,nm. *329 at until a depth of 680 then 150 following that. †CAL=75/50µm for three/two photon microscopy at 1280nm respectively.

These results confirm that organoids can be successfully imaged with multiphoton microscopy techniques. While cleared samples naturally allow deeper light penetration, our measurements show that imaging depths of approximately 200 µm are consistently achievable in uncleared heart and cardiac organoids. Given these depths, functional imaging of uncleared organoids and spheroids is feasible with the current setup.

Several strategies could further enhance imaging depth and signal quality. Adaptive optics (AO), such as deformable mirrors or electronically tunable lenses (ETL), can correct wavefront distortions in highly scattering tissue, improving both imaging depth and resolution. This has been demonstrated in a variety of biological samples [66, 69], including two-objective setups that also increase imaging speed [70].

Temporal focusing (TF) offers a complementary approach by enabling widefield multiphoton imaging with high speed using a camera instead of point detectors. TF has recently been shown to be compatible with three-photon microscopy [71, 72], and integration with remote focusing techniques allows small shifts of the focal plane without moving the sample [73, 74].

Another straightforward approach to improve signal yield is optimising pulse precompensation for organoid-induced group velocity dispersion (GVD). By measuring the dispersion introduced by the organoid in units of $fs^2 \mu m^{-1}$, pulse duration can be adjusted using the compressor, ensuring optimal excitation throughout the sample. This approach mimics some benefits of AO without requiring a complex feedback loop, applying precompensation as a function of imaging depth. Overall, these results demonstrate that multiphoton imaging in uncleared organoids is achievable and provide clear avenues for improving imaging depth, signal strength, and acquisition speed. The combination of adaptive optics, temporal focusing, and optimised pulse precompensation will likely allow functional and high-resolution imaging of organoids deeper than currently demonstrated.

An important observation is that the experimentally acquired image stacks did not extend to depths approaching the calculated attenuation length. This discrepancy does not indicate an inconsistency in the CAL measurement itself, but rather reflects practical limitations of the image formation and signal detection in our system. One contributing factor is the presence of optical aberrations present on the

right hand side of our images, which become increasingly significant with imaging depth in heterogeneous and scattering samples such as organoids. Sample-induced aberrations distort the excitation point spread function, reducing fluorescence efficiency and contrast before the exponential signal decay predicted by the CAL is reached.

In addition to sample-induced effects, residual system misalignment may also limit usable imaging depth. Deviations in beam alignment and imperfect objective back-aperture filling could have lead to suboptimal focal confinement and reduced multi-photon excitation efficiency. These effects accumulate with depth and can cause a premature loss of image quality relative to what would be expected from attenuation alone. Taken together, these considerations highlight that the CAL represents an intrinsic optical property of the sample rather than a strict limit on experimentally achievable imaging depth. In practice, imaging depth is determined by a combination of attenuation, aberrations, system alignment and signal-to-noise constraints.

5. Multiphoton Action Cross Sections of Fluorescent Dyes

This chapter analyses the specific dyes (DAPI and WGA-AF647) used in Chapter (3.6) to image both spheroids and organoids, focusing on their multiphoton action cross sections. We discuss the theoretical basis for calculating cross sections and outline the experimental methods including the ones employed. Particular emphasis is placed on the experimental setup, as numerous measurements contribute to ensuring its accuracy.

The results are then presented, analysed, and discussed, with relevant considerations taken into account.

5.1 Theory

As described in previous chapters, multiphoton microscopy operates on the principle of nonlinear multiphoton absorption. In this process, the same fluorophores used in conventional single-photon excitation can, in theory, be excited using photons at approximately twice (or more) the wavelength. However, as previously noted, this equivalence is not guaranteed—neither in terms of efficiency nor excitation wavelength [75, 76]. That is, a dye that performs efficiently under single-photon excitation

does not necessarily exhibit strong absorption when excited via two- or three-photon processes [77]. Therefore, quantifying a fluorophore's response to multiphoton excitation becomes essential [78]. This is characterised by the dye's multiphoton absorption cross section, denoted as σ_n, where n represents the order of the multiphoton absorption process.

The quantity N_{abs} represents the number of photons absorbed by a population of fluorophores (i.e., referring to concentration, not individual molecules). Unsurprisingly, $N_{abs} \propto I^n$, given here:

$$N_{abs}(t) = C\sigma_n \int_V I(\mathbf{r}, t)^n d\mathbf{r} \tag{5.35}$$

where I is the intensity of the incident light and n is the order of the absorption process, C defines the concentration of molecules per unit volume, normally given as molecules per cm^3. The integral here represents the rate of nonlinear excitation over the focal volume V for nonlinear order n.

From this, we can define the time-dependent fluorescence signal, $F(t)$, as shown in Equation (5.36):

$$F(t) = \frac{1}{n}\phi\eta N_{abs} \tag{5.36}$$

In this expression, ϕ is the collection efficiency of the detection system, η is the quantum efficiency of the fluorophore. The factor n^{-1} appears because, in an n-photon process, n photons are required to generate a single fluorescence emission event.

Since the order of nonlinear susceptibility is given by $n = m - 1$ two photon absorption can be considered a χ^3 dependant process and three photon absorption a χ^4 dependant process

We can define the action cross section as the product $\sigma_n \eta$ as the action cross section, a necessary requirement since we cannot determine individually the cross section or the quantum yield.

5.2 Methods for Calculation

Indirect Methods for Calculations

There are numerous methods for estimating the multiphoton absorption cross section σ_n of fluorescent dyes, both direct and indirect. This discussion focuses on experimental approaches used for two- and three-photon absorption. However, three-photon microscopy is still a young field and, as such, there are relatively few investigations of three-photon cross sections.

Most indirect measurement techniques rely on characterising a dye's nonlinear optical response χ^n. In the two-photon case, the dye's third-order susceptibility, $\chi^{(3)}$, is assessed. From this, absorptive behaviour can be inferred through the imaginary part of $\chi^{(3)}$. In these techniques, nonlinear signal generation arises from interactions involving multiple photons and is governed by the material's nonlinear susceptibility. However, since multiphoton absorption cross sections are not directly measurable through wave mixing, they must be inferred via theoretical models that connect these phenomena through the Kramers–Kronig [16] relations or perturbative quantum electrodynamics. Consequently, these measurements typically involve several assumptions about the material's electronic structure and the temporal and

spectral characteristics of the excitation light.

Wave-mixing techniques such as Coherent anti-Stokes Raman Scattering (CARS), Degenerate Four-Wave Mixing (DFWM) [79], and the optical Kerr effect [80] fall into this category. These methods are considered indirect because the extraction of σ_n depends on modelling the nonlinear interaction and linking it to $\chi^{(3)}$; for a theoretical treatment of this link, see [81].

5.2.1 Direct Methods for Calculation

From the perspective of direct measurement, early pioneers in multiphoton microscopy began reporting multiphoton absorption cross sections in the mid to late 1990s [78]. These measurements primarily focused on common fluorophores and involved both two-photon and, to a lesser extent, three-photon absorption. The studies utilised relatively simple multiphoton microscopy setups equipped with photon-counting detectors. By measuring the rate at which fluorophores emitted photons under controlled excitation conditions, researchers were able to estimate the efficiency of fluorescence generation and, from this, infer the multiphoton absorption cross section.

Direct measurements were carried out by leading researchers such as Blab [82], Webb and Xu [78, 83, 75, 84], among others. In these foundational investigations, fluorophores were typically characterised for their two-photon absorption cross sections, with some shorter-wavelength measurements of three-photon absorption also reported. These experiments required comprehensive characterisation of the excitation source, including the pulse duration, repetition rate, average power, and pulse energy, all of which are necessary for determining the photon flux and calculating an absolute cross section. In addition, accurate measurements required characterisation of the optical system itself, including transmission losses through the excitation path,

objective numerical aperture, pulse broadening due to dispersion, and the collection efficiency of the detection optics. Careful preparation of the fluorophore samples is also required, with the dye concentration accurately determined and maintained between measurements, as the measured fluorescence signal depends directly on the number of fluorophores present within the excitation volume.

Despite the apparent precision of these early determinations, most measurements were inherently comparative. Researchers relied on reference standards—fluorophores whose cross sections had been thoroughly characterised. Rhodamine and fluorescein, in particular, became widely used standards [85]. These dyes were typically calibrated by comparing their single-photon and two-photon excitation spectra, assuming that their quantum yield remained constant across the relevant excitation wavelengths.

Such assumptions, while simplifying calculations, introduce notable uncertainties. Specifically, if the quantum efficiency of a dye changes with excitation wavelength—a realistic possibility—the comparison to standards may become unreliable. As a result, reported values for two-photon cross-sections may carry an implicit caveat when different wavelengths are used. Compounding this issue, multiple independent studies have reported conflicting values for the same fluorophore, illustrating the variability and limitations inherent in the standard-based comparative approach.

The laser sources used in these early experiments typically included tunable titanium:sapphire (Ti:Sapph) lasers and fixed-wavelength sources such as Nd:YAG. This allowed researchers to explore excitation wavelengths up to approximately 1100nm with variable output power. Although this spectral range constrained the study of higher-order processes, some investigations into three-photon absorption were conducted. For instance, three-photon absorption has been demonstrated in organic compounds [86] and biologically relevant dyes such as DAPI [83].

Nonetheless, the ability to measure three-photon cross sections was limited by the lack of suitable laser sources. In particular, efficient three-photon excitation requires longer wavelengths (typically 1200–1700nm), high peak powers, and ultrashort pulse durations. These technical limitations prevented early researchers from fully characterising three-photon absorption behaviour in dyes commonly used for two-photon microscopy.

5.2.2 Extension to Three-Photon and Higher-Order Absorption Measurements

With advancements in laser technology—particularly the development of ultrafast sources [21] capable of delivering tunable longer wavelengths, higher peak powers, and precise pulse control—direct measurement techniques initially established for two-photon absorption have been successfully extended into the three-photon regime [85, 87]. These improvements have enabled more accurate and reliable characterisation of three-photon absorption cross sections by providing the necessary excitation conditions while minimising photodamage. This has enabled the reassessment of many previously studied fluorophores under three-photon excitation conditions, expanding our understanding of their nonlinear optical behaviour.

Once again, the Xu group has been at the forefront of this effort, leading numerous investigations into three-photon microscopy and dye characterisation at longer wavelengths [88, 38, 89]. Notably, their work has demonstrated even four-photon excitation in fluorophores such as fluorescein and wild-type GFP (wtGFP) using excitation wavelengths around 1700 nm. Among these studies, Cheng et al. [89] continued to rely on reference dyes for estimating three-photon cross sections, mirroring earlier two-photon methods. In contrast, La Violette et al. [38] achieved cross section measurements through detailed and rigorous system characterisation, without

the use of comparative standards.

These developments indicate that, with proper characterisation of both the illumination (e.g., pulse duration, beam profile, power) and the detection system (e.g., quantum efficiency, collection efficiency), it is possible to directly measure the three-photon absorption cross sections of various fluorophores. Thus, the methodologies established by La Violette and Cheng provide a solid experimental framework for future quantitative studies of nonlinear excitation in biological imaging.

5.2.3 Theory of Physical Methods

Combining 5.36 & 5.35 gives the average amount of generated fluorescence $\langle F(t)\rangle$:

$$\langle F(t)\rangle = \frac{1}{n}\, g^{(n)}\, \phi\, C\, \eta\, \sigma_n\, \langle I_0(t)\rangle^n \int_V S_n(\mathbf{r})\, d\mathbf{r} \tag{5.37}$$

Here some physical parameters have to be considered before generating an expression for cross-section.

The parameter $g^{(n)}$ is the nth-order intensity correlation function of the excitation source, given by:

$$g^{(n)} = \frac{\langle I_0^n(t)\rangle}{\langle I_0(t)\rangle^n} \tag{5.38}$$

This varies with the order of the absorption process n, determining how the generated nth-order intensity is affected by fluctuations in the instantaneous power applied. Therefore, if the pulse is chirped in some manner, $\langle I_0^n(t)\rangle$ will decrease substantially,

lowering the value of $g^{(n)}$. This parameter essentially quantifies how efficient pulsed laser sources are at generating nonlinear responses when compared to a CW source with the same average power.

Following this, the intensity correlation function is altered to consider only the fraction of time that the laser is 'on'. This is done by including the duty cycle term $(f\tau)$, raised to the power of $n-1$. This adjustment arises from the proportionalities: 2 Photon Excitation $\propto (f\tau)^1$ and 3 Photon Excitation $\propto (f\tau)^2$. Therefore, $g_p^{(n)}$ is defined as a unitless term depending on the temporal intensity profile of the beam:

$$g_p^{(n)} = g^{(n)}(f\tau)^{(n-1)} \tag{5.39}$$

This term accounts for the temporal variation at the sample's focus. To compute the spatial component, the integral (5.40) is evaluated, where $S_n(\mathbf{r})$ describes the spatial distribution of light at the focal point. This depends on the numerical aperture (NA), the wavelength used, and the refractive index of the sample, n_0.

The solution, the derivation of which can be found in several publications [38, 90, 78], is given by:

$$\int_V S_n(\mathbf{r})\, d\mathbf{r} = b_n \left(\frac{n_0 \lambda^3}{8\pi^3 \mathrm{NA}^4} \right) \tag{5.40}$$

Here, the parameter b_n accounts for the spatial distribution of the focused excitation intensity, which depends on the wavelength, process order and NA of the objective lens. For our system, these values are $b_2 = 64.1$ and $b_3 = 28.18$, for an NA of 0.8 and a wavelength of 1300nm.

Combining equations 5.40 and 5.39 with 5.36 yields equations 5.41 and 5.42, which describe the fluorescence signal rates for the two- and three-photon cases,

respectively.

$$\langle F(t)\rangle_2 = \frac{1}{2}\frac{g_p^{(2)}}{f\tau}\phi C\eta\sigma_2 n_0 \frac{b_2\langle P(t)\rangle^2}{8\pi\lambda} \tag{5.41}$$

$$\langle F(t)\rangle_3 = \frac{1}{3}\frac{g_p^{(3)}}{(f\tau)^2}\phi C\eta\sigma_3 n_0 \frac{b_3 \mathrm{NA}^2\langle P(t)\rangle^3}{8\pi\lambda^3} \tag{5.42}$$

Measured from photon counts over a time t for the time-averaged input power $\langle P(t)\rangle^n$, the intensity correlation function is included here as a function of the measurable quantity $g_p^{(n)}$ over the duty cycle.

From this, an expression for the cross-sectional area can be derived straightforwardly. By defining $\mathrm{F_M}$ as the total fluorescent signal collected during the measurement time $\mathrm{T_{cnt}}$, and $\langle P_M\rangle^n$ as the effective excitation power raised to the nth power integrated over $\mathrm{T_{cnt}}$, we relate the observed signal to the multiphoton cross section:

$$\eta\sigma_2 = \frac{16 f\tau\pi\lambda_0}{b_2 g_p^{(2)}\,\phi C n_0 T_{\mathrm{cnt}} T_{\mathrm{cal}}^2}\,\frac{F_M}{\langle P_M\rangle^2} \tag{5.43}$$

$$\eta\sigma_3 = \frac{24 f^2\tau^2\lambda_0^3}{b_3 g_p^{(3)}\,\phi C n_0\,\mathrm{NA}^2\,T_{\mathrm{cnt}}\,T_{\mathrm{cal}}^3}\,\frac{F_M}{\langle P_M\rangle^3} \tag{5.44}$$

These correspond to the action cross section, defined as the product of the quantum efficiency, η, and the multiphoton cross section, σ_n. This combined parameter is necessary because the quantum efficiency cannot be independently evaluated here, effectively coupling the two quantities into the action cross section.

5.3 Experiment

To obtain direct and reliable measurements of the multiphoton action cross sections of our fluorescent dyes, it is essential to have a comprehensive understanding of several fundamental parameters related to our microscope and experimental setup. These include, but are not limited to, the pulse duration of the excitation source, the optical power delivered to the sample, the concentration of the dye, the photon counting regime employed during detection, and the central wavelength along with the spectral bandwidth of the excitation light. For this reason, the WLD3 preset described in Section 3.1 was used, as it provides the narrowest spectral bandwidth and therefore the best-defined excitation wavelength, described in 3.2.

Each of these parameters plays a critical role in shaping the measured fluorescence signal and, consequently, the calculated multiphoton action cross section. For example, the pulse duration influences the peak intensity and temporal profile of the excitation, which directly affects nonlinear absorption probabilities. Similarly, the power applied to the sample must be accurately measured and controlled, as deviations can lead to significant errors in quantifying the nonlinear response. The concentration of the dye must be precisely known to ensure that the number of fluorophores contributing to the signal is correctly accounted for, avoiding saturation effects or self-quenching. The photon counting regime impacts the sensitivity and linearity of detection, and the central wavelength and spectral bandwidth determine the excitation efficiency for the specific multiphoton process being investigated.

Given the critical influence of these factors, each has undergone thorough characterisation and calibration prior to data acquisition. This rigorous approach ensures that our experimental conditions are well defined and stable, providing a reliable foundation for the subsequent analysis and interpretation of the multiphoton cross section measurements.

5.3.1 Experimental Setup

The setup used can be seen in Figure (5.45). The core optical layout of the microscope described in Section (3.6) was retained, with additional components incorporated for pulse-duration measurement and photon counting.

A time correlated single photon counter (TCSPC) from Swabian has been added here, capable of sampling our signal at 90MHz, with multiple input channels. Here it is used for synchronisation with the laser clock and either PMT 1 or 3 to count the number of photons received from the sample over a defined time period.

Here the objective, Nikon N40XW-PF, 0.8 NA, 40×, water immersion, has been used. Although this objective is normally used with visible and NIR wavelengths here it is being used with wavelengths near 1300nm. This of course will change the actual NA away from the nominal value (0.8), since this has not been characterised it has instead been considered in the error of our measurements. This change in applied wavelength also changes the power tranmission and pulse dispersion, both of which have been characterised in previous chapters.

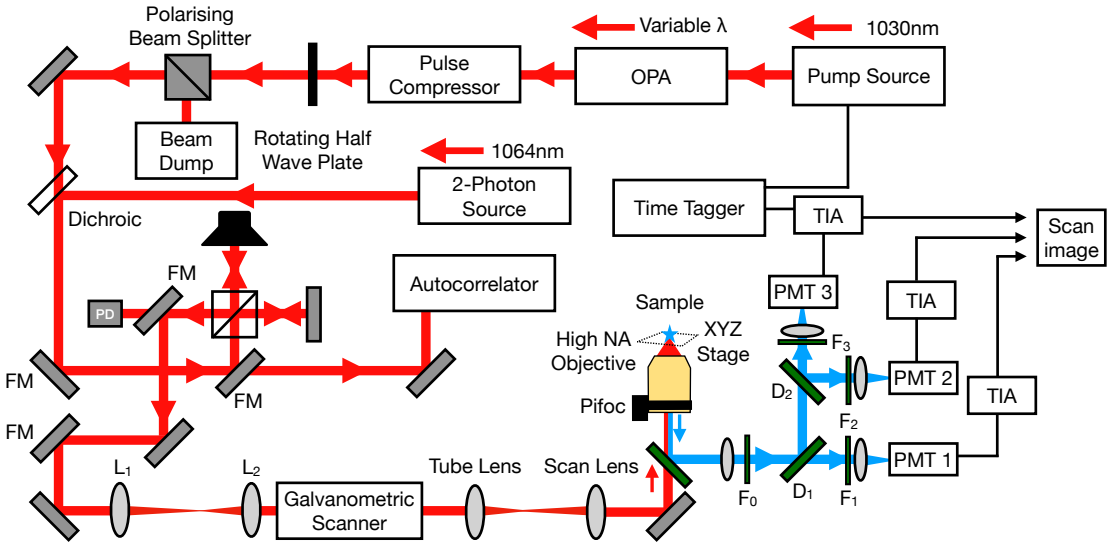

Figure 5.45: Three-photon microscope setup with adaptations to measure pulse duration and action cross section. OPA: Optical Parametric Amplifier, FM: Flip Mirror, PD: Photodiode, L_1 & L_2 form a beam reducing telescope, $F_{0,1,2,3}$: excitation filters, $D_{1,2}$: Excitation dichroics, PMT: photomultiplier tube, TIA: transimpedence amplifier, Scan image: aquisition software. Full detail of the components can be found in section 3.3

5.3.2 Excitation Wavelength

To accurately assess the wavelength dependence of fluorescent dyes, it is useful to work with a laser source that has as narrow a spectral bandwidth as possible. In an ideal case—such as with a continuous-wave (CW) laser—this would allow for highly precise analysis, as the output consists of a single, well-defined wavelength. However, its not practical as the instantaneous peak powers required to drive nonlinear processes efficiently will increase the average power. Moreover, as discussed earlier, the situation becomes more complicated when using ultrafast lasers. Because of the Fourier limit, the spectral bandwidth is directly tied to pulse duration: shorter pulses require broader bandwidths. This limits the ability to isolate a narrow wavelength range without significantly lengthening the pulse. As a result, a practical compromise must be made—producing a spectrum that is narrow enough to define a clear central wavelength, while still maintaining short pulse durations that enable efficient multiphoton excitation. This approach allows for better control over both the wavelength and the temporal profile of the pulse. For this purpose I have decided to use the OPA's WLD3 preset described in Section 3.2.

With reference to the use of WLD3, exact quantification of the spectrum has been performed. As discussed in Section 3.2, spectral tuning of the OPA typically produces a distribution centred approximately around the target wavelength. However, the presence of unexpected peaks or noise within the spectrum can lead to inaccuracies if one simply takes the peak or nominal central wavelength at face value. To mitigate this, a more robust approach—calculating the spectral centre of mass—was adopted to determine the effective central wavelength of the output.

Target Central λ (nm)	1250	1275	1300	1325	1350	1375
Measured Central λ (nm)	1250.3	1272.3	1297.2	1319.7	1339.9	1362.2
Measured FWHM (nm)	42.2	44.3	35.1	32.1	36.9	35.6

Table 5.5: Central Wavelengths compared with the expected value

$$\lambda_0 = \frac{\int_{-\infty}^{\infty} \lambda S(\lambda)\, d\lambda}{\int_{-\infty}^{\infty} S(\lambda)\, d\lambda} \tag{5.45}$$

Equation (5.45) defines the centre-of-mass calculation, where the central frequency ω_0 is given by the weighted average of spectral intensity ($S(\omega)$) over frequency (ω). This method takes into account all spectral components, thereby providing a more accurate representation of the spectrum's mean wavelength and reducing the influence of anomalous peaks or noise.

A comparison of the primary wavelengths used in this experiment is shown in Figure (5.46). The relatively narrow spectral bandwidth that has been generated is shown here. The deviation of the measured central wavelength and measurements of the FWHM can be found in Table 5.5. Here the FWHM has been measured explicitly, taking the intersection of the spectrum to half it's maximum value.

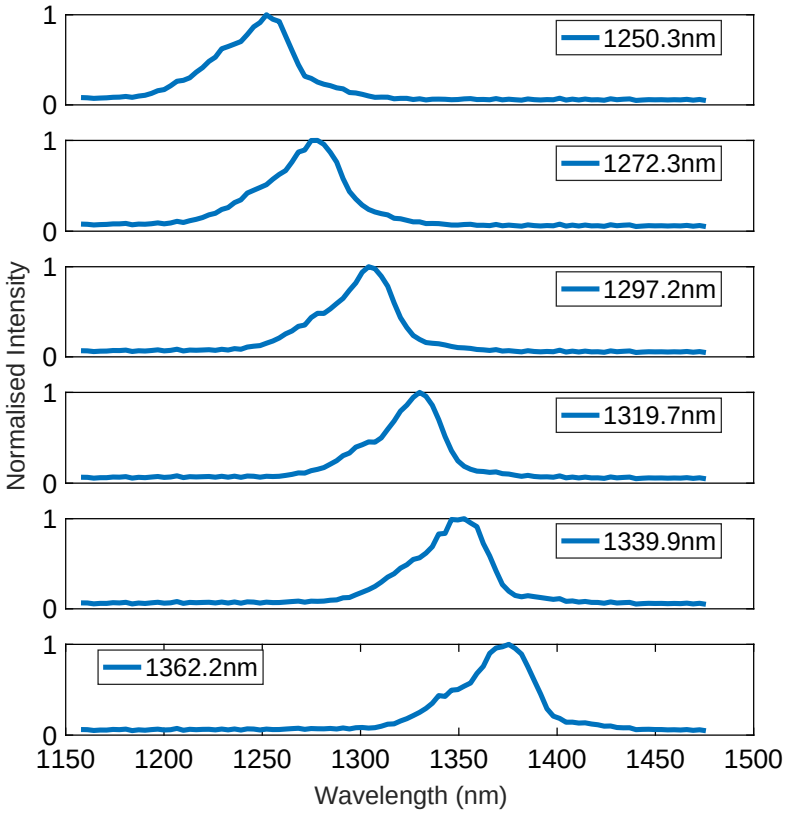

Figure 5.46: Centre-of-mass calculations for spectra generated with target central wavelengths of 1250, 1275, 1300, 1325, 1350, and 1375 nm. The corresponding centre-of-mass wavelengths are shown. All spectra were generated using the WLD3 preset.

5.3.3 Temporal Considerations

Since both the central wavelength and spectral bandwidth of the output have been modified through the use of the WLD3 preset, previous measurements of pulse duration no longer stand. This is since changing the spectral output ($\Delta\lambda$) will alter the bandwith product TBP = $\Delta\nu\Delta\tau$), therefore, it is likely a different value for the applied precompensation will be required.

As such, pulse characterisation has been repeated for each generated wavelength following the same procedure outlined in Section 3.5.2.

To achieve this, inline autocorrelation was used to measure pulse duration at the sample plane. The setup remains as shown in Figure 5.45, with the beam redirected into the autocorrelator using flip mirrors. Pulse duration was measured as a function of precompensation by adjusting the dispersion applied by the pulse compressor. This process was repeated from the minimum to the maximum precompensation setting for each central wavelength calculated using Equation 5.45.

The results are shown in Figure 5.47, demonstrating how pulse duration varies with precompensation. As expected, longer central wavelengths require greater amounts of precompensation to achieve optimal temporal compression.

Using the data presented in Figure (5.47), the shortest achievable pulse duration for each wavelength can be extracted. This determines the optimal precompensation setting required to temporally compress each pulse to its minimum width, shown in Figure (5.48). Here the corresponding optimal precompensation values required to achieve these durations are shown the the figure legend. Pulse durations range from 73.3 - 48.8fs across the central wavelength range of 1250.3 - 1362.2nm. These values were subsequently used as the fixed precompensation settings for all remaining measurements throughout this experiment.

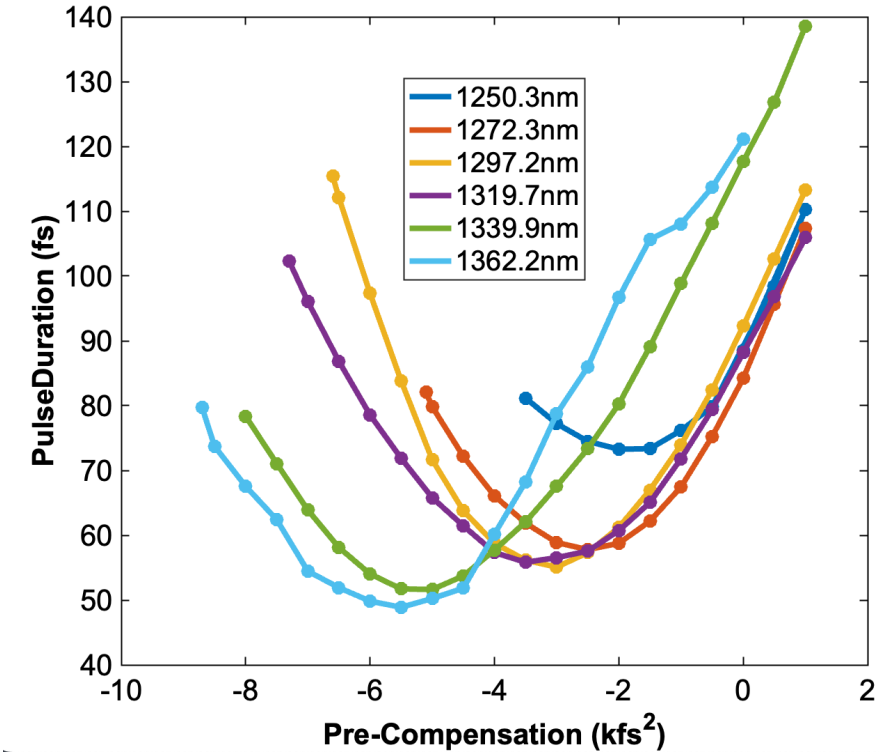

Figure 5.47: Measured pulse durations at the sample plane as a function of applied precompensation for various central wavelengths generated using the WLD3 preset. Each wavelength exhibits the expected quadratic relationship between pulse duration and applied group delay dispersion (GDD), consistent with previous observations. Notably, the lower spectral bandwidths associated with the WLD3 preset result in a reduced requirement for precompensation to achieve temporal compression.

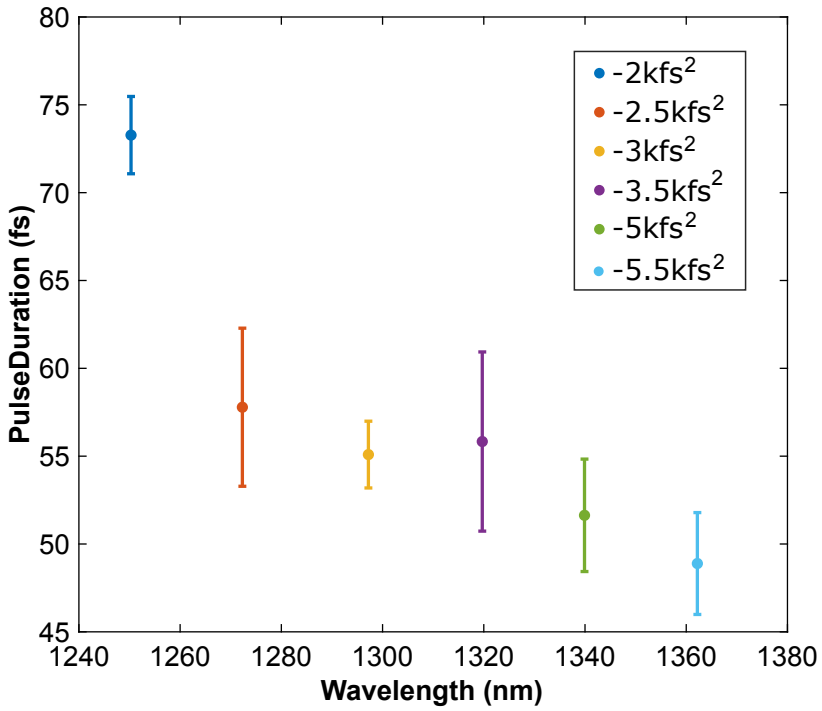

Figure 5.48: Shortest measured pulse durations at the sample plane for each central wavelength using the WLD3 preset.

5.3.4 Collection Efficiency

Calculating the fraction of generated photons that are actually collected is crucial to accurately determining the cross section, as it effectively indicates the true number of photons produced. This fraction is calculated as the cumulative effect of all losses through optical elements between the focal point and the signal sent to the amplifier, providing a measure of the total system loss. A more detailed schematic of the collection setup is shown in Figure (5.49).

To formalise the process we can define the total collection efficiency and product ϕ as being the product of all losses encountered, Equation (5.46):

$$\phi = \xi_{frac} * \xi_{\Delta z} * \xi_{CS} * \xi_{w} * \xi_{obj} * \xi_{M_1} * \xi_{D_0} * \xi_{L_{3,4}} * \xi_{M_2} * \xi_{D} * \xi_{F} * \xi_{L_{5/7}} * \xi_{PMT_\lambda} \quad (5.46)$$

ξ_f, is the total fraction of generated photons are are collected by the objective. $\xi_{\Delta z}$ & ξ_w are losses due to absorption within the dye and water, calculated using the Beer-Lambert law. ξ_{CS} is the loss from the cover slip. ξ_{obj}, $\xi_{L_{3,4}}$, and $\xi_{L_{5/7}}$ represent the total losses from the lenses that the emitted light must traverse at each respective wavelength. ξ_{M_1} & ξ_{M_2} represent loss from the two mirrors M_1 and M_2 with ξ_D accounting for losses due to the dichroic D_0. ξ_D accounts for losses due to reflection or transmission through the dichroics in the collection arm. ξ_F is the combined loss from the filters F_0 and either F_3 or F_1. Finally, ξ_{PMT_λ} denotes the quantum efficiency of the PMT at the dye's peak emission wavelength. These values are typically provided by manufacturers and can be found in lookup tables.

To calculate the fraction of emitted photons collected versus the total number generated (ξ_{frac}), we make the critical assumption that the emitted light is truly isotropic. This follows from the assumption that the fluorophores' molecular orien-

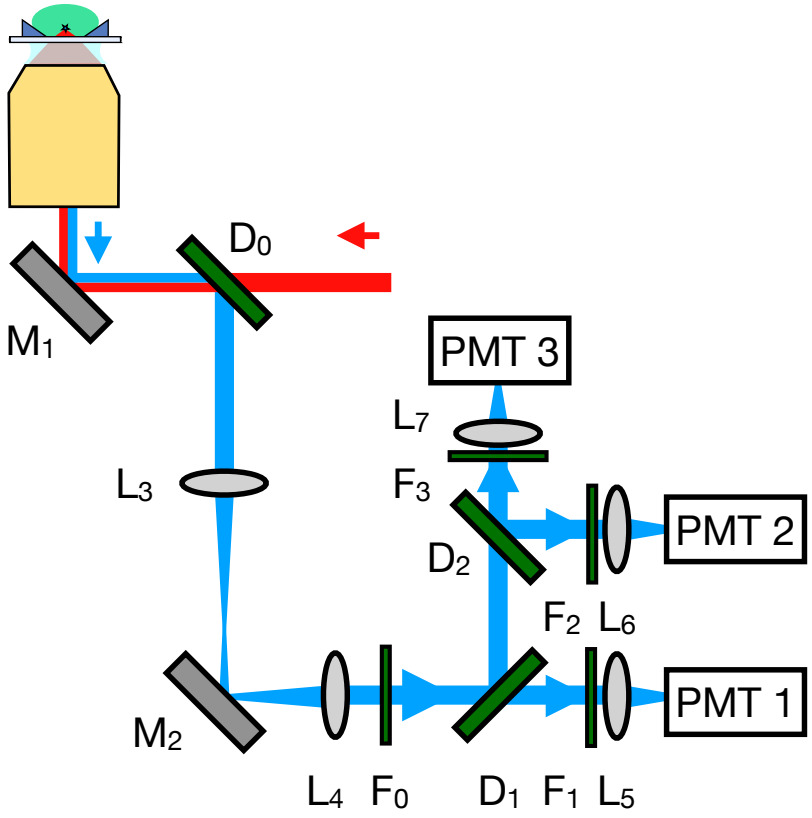

Figure 5.49: A more detailed version of the collection arm of the experimental setup shown in Figure (5.45). The objective lens is a water immersion lens, therefore water is used between the objective lens and cover glass. Here all optical elements that the signal have to traverse are shown; Objective: N40XW-PF (Nikon), M_1: PFR14-P02 (Thorlabs), D_0: DMLP805R (Thorlabs), L_3: LA5714 (Thorlabs), M_2: PF20-03-P01 (Thorlabs), L_4: LA1979 (Thorlabs), F_0: FESH0850 (Thorlabs), D_1: FF556-SDi01 (Semrock), F_1: ET525/50m (Chroma), L_5: LA1951 (Thorlabs), D_2: FF659-SDi01 (Semrock), F_2: FF01-650/13 (Semrock), L_6: LA1951 (Thorlabs), F_3: BLP01-647R-25 (Semrock), L_7: LA1951 (Thorlabs).

tations are random. Using Equation (5.47), ξ_{frac} is determined as the fraction of photons collected by an objective with numerical aperture (NA) and refractive index n_0.

$$\xi_f = \frac{1}{2}\left(1 - \sqrt{1 - \left(\frac{\mathrm{NA}}{n_0}\right)^2}\right) \tag{5.47}$$

ξ_{CS} represents the transmission through both interfaces of the coverslip. This value was calculated using the Fresnel equations for s- and p-polarised light, taking the average since our light source is randomly polarised. Figure (5.50) shows how the transmission varies up to the maximum acceptance angle of the objective, defined as $\theta_{max} = \sin^{-1}(\mathrm{NA}/n_0)$, where n_0 is the refractive index of the immersion medium (water: 1.33).

The resulting overall transmission, ξ_{CG}, is 0.9905, 0.9908, and 0.9914 for DAPI, Fluorescein, and Cy5, respectively. While this represents only a minor source of loss, it is nevertheless important to include. By contrast, if an air objective were used instead, the transmission would be approximately 0.92, making the loss significantly more impactful.

$\xi_{\Delta z}$ represents the attenuation of photons as they travel through a distance Δz within the dye. Similarly, ξ_w accounts for the reduction in collection efficiency due to absorption by the immersion water.

Using the Beer–Lambert law and assuming all dyes have the same refractive index ($n = 1.33$), we calculate the transmission through both the immersion water and the dye. By evaluating the path length Δz (50 µm) together with the objective's working distance, we determine the values of $\xi_{\Delta z}$ and ξ_w. The wavelength-dependent water absorption coefficients were taken from Landsman [91]. Total transmission estimates

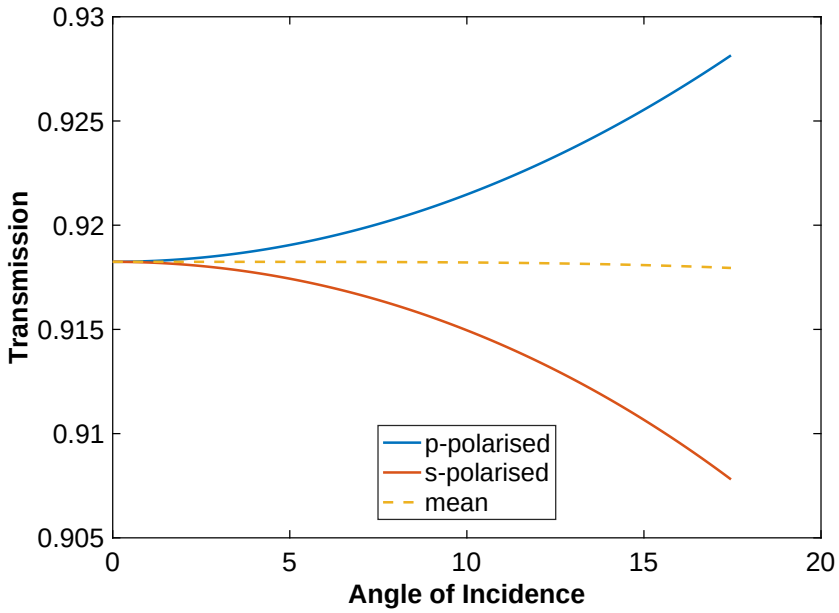

Figure 5.50: Transmission through both interfaces of the coverslip, calculated using the Fresnel equations. The plot shows transmission for light at 480 nm, corresponding to DAPI's central emission wavelength.

for all optical elements depicted in Figure 5.49 have been compiled in Table 5.3.4.

Part \ Dye	DAPI	Fluorescein	Cy5	Reference
ξ_f	0.0230	0.0230	0.0230	Equation 5.47
$\xi_{\Delta z}$	0.9950	0.9983	0.9704	Theoretical
ξ_{CS}	0.9908	0.9908	0.9914	Theoretical
ξ_w	0.837	0.9214	0.9396	Theoretical
ξ_{obj}	0.88	0.872	0.81	Appendix F.66
ξ_{M_1}	0.93	0.93	0.84	Appendix F.67
ξ_{D_0}	0.97	0.984	0.99	Appendix F.68
$\xi_{L_{3,4}}$	0.893	0.893	0.893	Appendix F.69
ξ_{M_2}	0.965	0.96	0.955	Appendix F.67
ξ_{F_0}	0.98	0.99	0.99	Appendix F.70
ξ_D	0.975	0.9506	0.942	Appendix F.71, F.72
ξ_F	0.99	0.97	0.97	Appendix F.73, F.74
$\xi_{L_{5/7}}$	0.97	0.97	0.97	Appendix F.69
ξ_{PMT_λ}	0.454	0.424	0.321	Appendix F.69
Total ϕ (%)	0.541	0.538	0.336	

Table 5.6: Normalised loss for each contribution / total losses throughput for all optical elements between detection and fluorescence generation for the three dyes used.

5.3.5 Detection

Two GaAsP (Gallium Arsenide Phosphide) photomultiplier tubes (PMTs; Hamamatsu H10770PA-40) were used in this experiment to detect the fluorescent signals generated by multiphoton excitation. These PMTs offer high quantum efficiency in the visible range and low dark count rates, both of which are essential for accurately quantifying weak fluorescence when determining the multiphoton action cross section. The filters and dichroics corresponding to the detection channels are detailed in Table 5.7.

Each PMT output is connected to a transimpedance amplifier (Thorlabs TIA60), which converts the PMT's current output into a voltage signal. The TIA60 provides a bandwidth of up to 60 MHz and a fixed transimpedance gain of 30200 V/A. Although this bandwidth far exceeds the frequency content required for photon counting, it ensures preservation of fast signal transitions, which is beneficial for precise edge detection and clean timing discrimination.

Due to the known red-shift in DAPI fluorescence under multiphoton excitation, both DAPI and Fluorescein emissions are detected on Channel 1, while Cy5 fluorescence is collected on Channel 3. The optical filter and dichroic configuration used for spectral separation is shown in Table 5.7. These filter sets were selected to minimise spectral overlap and optimise detection efficiency, which is critical for ensuring accurate and reproducible quantification of relative fluorescence signals for cross-section analysis.

Photon counting is performed using a Swabian Instruments Time Tagger Ultra, a high-precision time-to-digital converter capable of recording individual photon arrival times with picosecond-scale resolution. While the device is commonly used in time-correlated single photon counting (TCSPC) applications to extract fluorescence lifetimes, in this experiment it is used exclusively in photon counting mode to

quantify the number of detected photons under varying excitation conditions.

To achieve consistent timing accuracy across different signal amplitudes, a constant fraction discriminator (CFD) is employed. This reduces time walk and ensures reliable edge detection. A dedicated Sync channel receives a TTL trigger from the laser pulse train, enabling precise temporal alignment of detected photons with the excitation source. While lifetime information is not extracted in this study, this synchronisation permits optional gated acquisition and ensures consistency in timing reference.

The Time Tagger Ultra supports sustained detection rates of up to 90 MHz per channel and can record both rising and falling edges. Its key specifications include a time resolution (timebin resolution) of 3 ps, RMS timing jitter of approximately 8 ps, and a dead time of less than 1 ns. These performance characteristics, although exceeding the requirements of the present experiment, ensure accurate and linear photon counting across a wide dynamic range. This high fidelity is essential for precise cross-sectional area measurements, where relative changes in photon emission must be attributed solely to excitation parameters rather than detector limitations.

Label	Component	λ Range (nm)
F_0	Short Pass at 850	Below 850
F_1	525/50, (Chroma)	500 - 550
F_2	FF01-650/13 (Semrock)	643.5 - 656.5
F_3	BLP01-647R-25 (Semrock)	647 - 850
D_1	FF556-SDi01 (Semrock), Short Pass	< 556
D_2	FF659-SDi01 (Semrock), Long Pass	> 659
PMT 1,2,**3**	Hamamatsu H11706-40 + **H11706-40-01** (GaAsP)	300 - 720

Table 5.7: Details of the filters and dichroics used in the setup for measuring fluorescent signals. The λ Range column indicates the spectral bandpass of each dichroic and filter, with the label corresponding to the components shown in Figure 5.45.

5.3.6 Dye Preparation

For this experiment our three dyes were prepared with the help of Sasha Forbes (PGR).

The solutions of DAPI, fluorescein and Cy5 were first prepared as stock solutions by dissolving their powdered forms in deionised water (dH_2O). The stock solutions were subsequently diluted using a buffer solution to ensure a neutral pH, consistent with physiological conditions. This approach was chosen in contrast to some published protocols where pH is deliberately adjusted to enhance fluorescence. By maintaining neutrality, we aim to replicate the dye's behaviour in biological tissue, where pH deviations may lead to cellular damage or altered dye performance. This provides a more realistic assessment of each dye's fluorescence under intended experimental conditions.

For Fluorescein (Sigma-Aldrich), 250 mg was dissolved in 75 mL of dH_2O to yield

a 10 mM stock solution, which was then diluted 1:1000 with buffer to produce a 10 µM working solution. DAPI dilactate (Thermo Fisher Scientific) was prepared by dissolving 10 mg in 1.28 mL of dH_2O, resulting in a 10 mM stock, which was diluted 1:100 to achieve a 100 µM final concentration. Sulfo-Cy5 (TargetMol) was similarly prepared by dissolving 10 mg in 1.28 mL of dH_2O, yielding a 10 mM stock, then diluted 1:100 with buffer to obtain a final concentration of 100 µM.

Fluorescein was deliberately diluted by an additional order of magnitude compared to the other dyes. This was done both to align with concentrations commonly used in prior studies and to prevent saturation or potential damage to the PMTs due to its high fluorescence yield.

Using the a commercial spectrometer, the Duetta Horiba, we measured the one-photon excitation and emission spectra of our dyes, in doing so we can determine if our dyes are behaving as expected before attempting a complex experiment with them, ruling out potential errors with multiphoton excitation. Single photon measurements were also carried out both to determine the appropriate filter configuration and to attempt a comparison between the single and three-photon excitation cases. Of course, this comparison is challenging due to the inherent complexity of the different excitation processes of single and multiphoton.

From a basic theoretical standpoint, the emission spectrum from a three-photon excitation process should be identical to that of one-photon excitation. However, as observed when imaging spheroids and organoids, DAPI exhibited a green spectral shift.

During the experiment, a fresh 100 µL aliquot of dye was deposited onto the coverslip setup shown in Figure (5.52). This was done to ensure no photobleaching occurred while maintaining the same axial position, Δz. This was then repeated

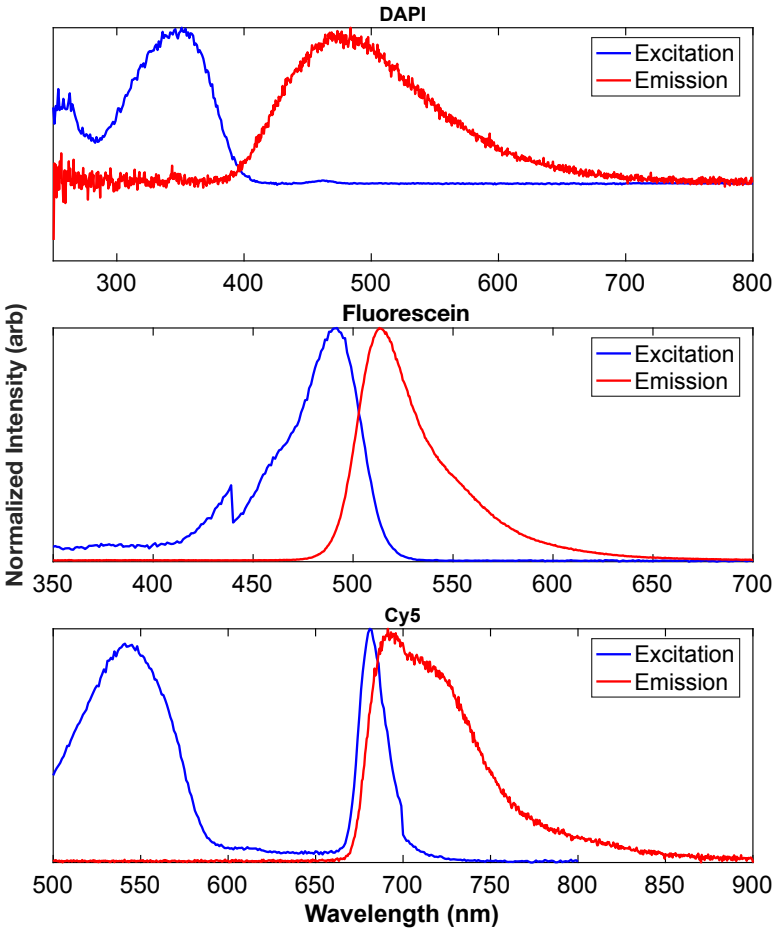

Figure 5.51: Single-photon excitation and emission spectra of the three dyes, measured by the Horiba Duetta.

before changing the wavelength.

5.3.7 Data Taking Procedure

All data were acquired using the white light delay 3 (WLD 3) preset, which as previously mentioned provides the narrowest spectral bandwidth available. Correspondingly the shortest pulse duration was then achieved using the amount of precompensation shown in Figure 5.48.

For each dye measurement, the axial distance Δz between the focal plane and the cover glass surface was fixed at 50µm. This positioning was established prior to dye introduction by assembling the setup shown in Figure 5.52 and identifying the third order harmonic generation (THG) signal generated at the water/glass interface. This signal was located by translating the interface into the laser focus at elevated excitation powers ($\approx$ 200mW), where nonlinear effects are readily observed. The optical setup employed a water immersion objective lens with a 2mm working distance. A standard borosilicate cover slip (Corning No. 1, 170µm thick) was used, in accordance with the objective manufacturer's specifications. To contain the sample, approximately 100µL of dye solution was placed into an open-top cavity formed on a glass-bottom dish using Blu Tack (Bostik). The axial distance Δz, as shown in Figure (5.52), effectively defines the thickness of dye that the incident, focusing beam traverses before reaching the focal volume. By using the z location of THG signal as a reference the same was then translated axially to achieve the desired Δz for all subsequent measurements. This ensured that the same amount of dye was in place between the cover slip and the focal spot.

The excitation power was then adjusted incrementally, and the dye was excited at each power level for 30 seconds at a fixed wavelength. After imaging, the sample was removed, and the power at the objective was measured at the same increments. The wavelength and precompensation settings were then changed, and the process was repeated.

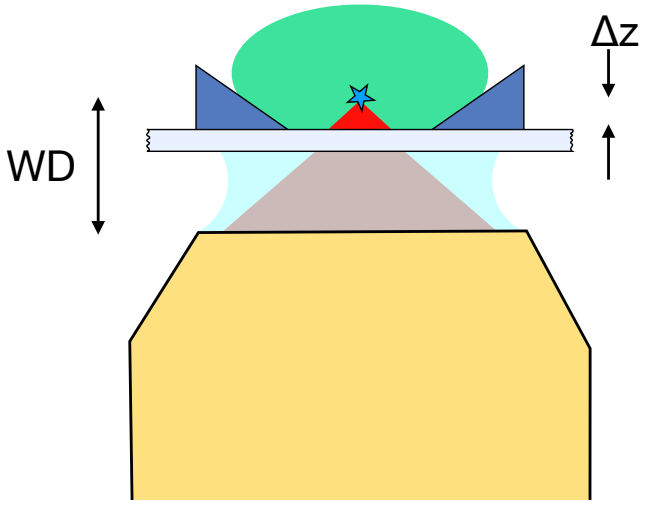

Figure 5.52: Cross section of the focal volume showing the top of the inverted microscope's objective.

To avoid damage to the PMTs and to accommodate dye brightness differences, the repetition rate was varied for each dye. DAPI was measured at the maximum available repetition rate of 1 MHz, while Fluorescein was measured at 500 kHz to match the conditions used in [38].

5.4 Multiphoton Action Cross Section Measurements

As described in Section (5.3.7), data was collected over a range of increasing excitation powers for each dye and wavelength. This leads to a corresponding increase in photon counts, following the dye's characteristic power scaling behavior. As before, the data can be represented on a log-log plot to examine the power dependence.

The raw data plotted on a log-log scale are shown in Figures (5.53) and (5.4). In all cases, the fits deviate from ideal behavior, with the data exhibiting 'super-nonlinear' increases at higher powers, meaning that the power scaling seems to be of a higher order.

To properly characterise this, we focus on the regions where photon counts scale approximately quadratically or cubically—consistent with the expected two-photon or three-photon excitation processes, respectively.

This approach follows the methodology of [92], where deviations from ideal detector behaviour were similarly observed. Accordingly, the data used for calculating cross sections, shown in Figures (5.53) and (5.4), are taken from these regions exhibiting power law slopes near 2 (for Cy5) and 3 (for DAPI and Fluorescein). Here measurements were taken at six characterised wavelengths using a repetition rate (laser rep rate) of 125 kHz, 500 kHz and 1 MHz for Cy5, Fluorescein and DAPI respectively. A line of best fit for each wavelength has been included with legends indicate the gradient of each fit.

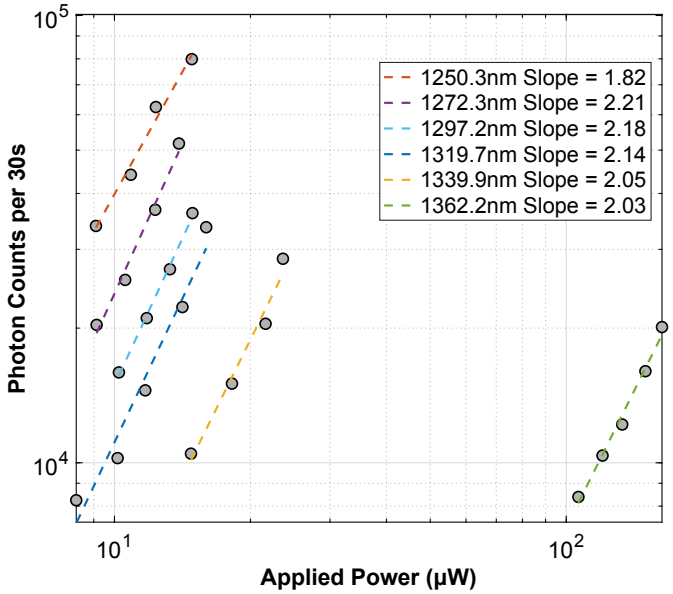

Figure 5.53: Results of Cy5 measurements shown on a log-log scale to illustrate power scaling. Measurements were taken over 30s intervals, showing evidence of a 2 photon process.

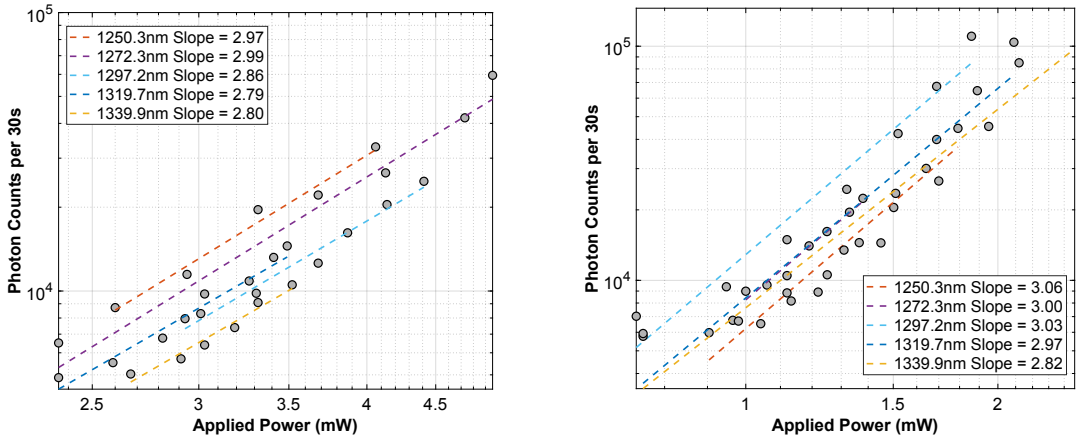

Figure 5.54: Three-photon dye measurements: (**A**) DAPI and (**B**) Fluorescein

5.4.1 Photon Counting Troubleshooting

Unexpected nonlinearities in photon count data prompted an investigation into potential sources of systematic error in the detection chain. A primary concern was PMT afterpulsing—spurious signal events following legitimate photon detections—which could lead to artificially inflated photon counts, especially at high excitation powers.

To examine this, a control experiment was carried out using a β-Barium Borate (BBO) crystal (Eksma Optics, 50 µm thick), which exhibits a well-characterised second-order nonlinear optical response. The BBO was mounted as shown in Figure 5.55, with the crystal positioned such that the focal volume was centered within the material while maintaining optical contact with the water immersion objective. This geometry attempts to reduce high-index boundaries and ensures that any measured signal originates from within the crystal.

The crystal was illuminated at 1350 nm to suppress THG and to ensure that the resulting SHG (675 nm) fell cleanly within the passband of filter F_3 on Channel 3.

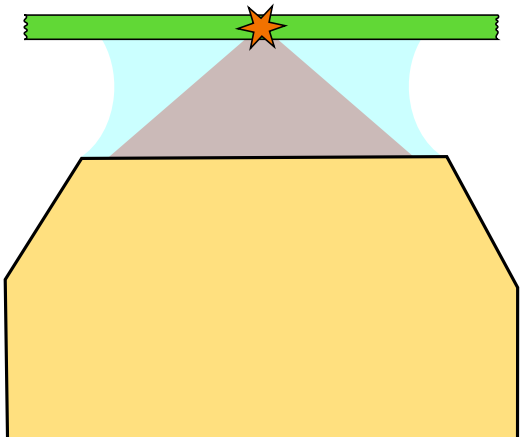

Figure 5.55: Experimental configuration for SHG-based control experiment using a BBO crystal (Eksma Optics, 50 µm thick). The crystal is mounted in contact with the water immersion objective to eliminate high-index interfaces.

This was checked to ensure that all scaling oberved would be a second order process. With this configuration, the PMT output was monitored via the connected transimpedance amplifier (Thorlabs TIA60), and its analog signal was recorded using a digital oscilloscope (Rigol MSO5104). Excitation power was gradually increased, and the resulting signal waveforms were examined for evidence of after pulsing.

Figure 5.56 shows that delayed secondary pulses begin to appear roughly 25 ns after the initial detection event and grow in prominence with increasing power. These delayed signals are consistent with known PMT afterpulsing effects and would result in false photon counts if uncorrected.

To suppress these spurious detections, the TCSPC module's `dead time` was increased to 200 ns. This inhibits additional counts within a fixed window following each registered event and prevents after pulsing from inflating the data.

Following this adjustment, the power-scaling experiment was repeated using the BBO crystal as a reference. Photon counts were recorded as a function of incident power, and the results are shown in Figure 5.57. The data reveals three distinct re-

gions in the log-log plot, with slopes of 1, 2, and 3 corresponding to linear, quadratic, and higher-order dependencies. This confirmed that the system was capable of reproducing known nonlinear optical behaviours.

Despite the correction for afterpulsing, a residual superlinear response was observed, particularly at higher powers. To determine whether this was caused by the photon-counting hardware itself, the same experiment was repeated using a different TCSPC system (quTAG, quTools). As shown in Figure 5.58, the nonlinear trend persisted, indicating that the counting electronics were not responsible. The theoretical value of photon count rate matched roughly matched the initial count rate, ruling out any pulse pile up.

Consultation with Swabian Instruments and other TCSPC experts identified the likely cause: the PMTs used in this setup were operated in analog mode, where output pulse amplitude scales with the number of photoelectrons generated. This is fundamentally different from Geiger-mode devices, which produce uniform digital pulses tailored for time-tagging systems. Analog-mode operation can result in multiphoton events producing larger pulses that exceed discriminator thresholds multiple times, leading to duplicate or false counts—particularly at high signal levels.

While operating the PMTs in Geiger mode would produce more TCSPC-compatible signals, this would limit the maximum count rate to $\sim$10 kHz, far below the laser repetition rates (125 kHz to 1 MHz) used throughout this study. Such a reduction would severely increase acquisition time (T_{cnt}) and compromise statistical accuracy. Therefore, analog-mode operation was retained, with afterpulsing suppression and power-limited acquisition protocols in place to minimise detection artefacts.

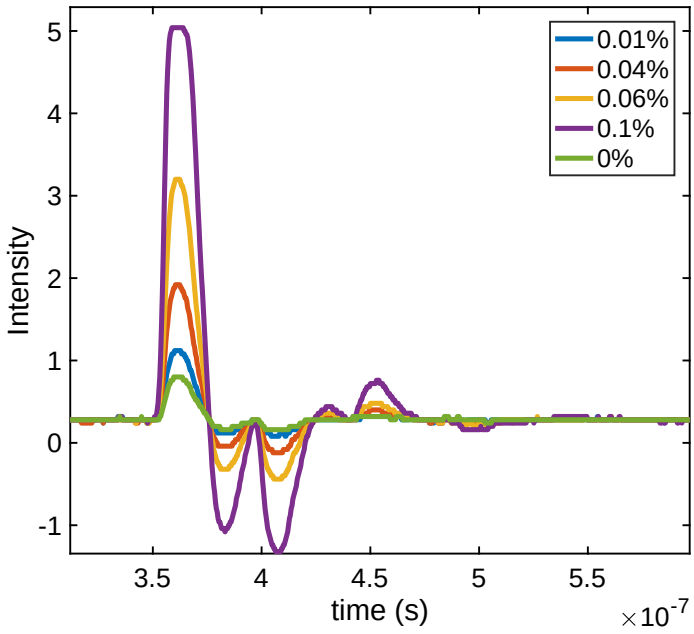

Figure 5.56: PMT signal recorded using a Rigol MSO5104 oscilloscope as the power is increased in % terms of the total power at 1300nm linearly. After pulsing becomes increasingly prominent with excitation power typically appearing ∼25 ns after the main detection pulse.

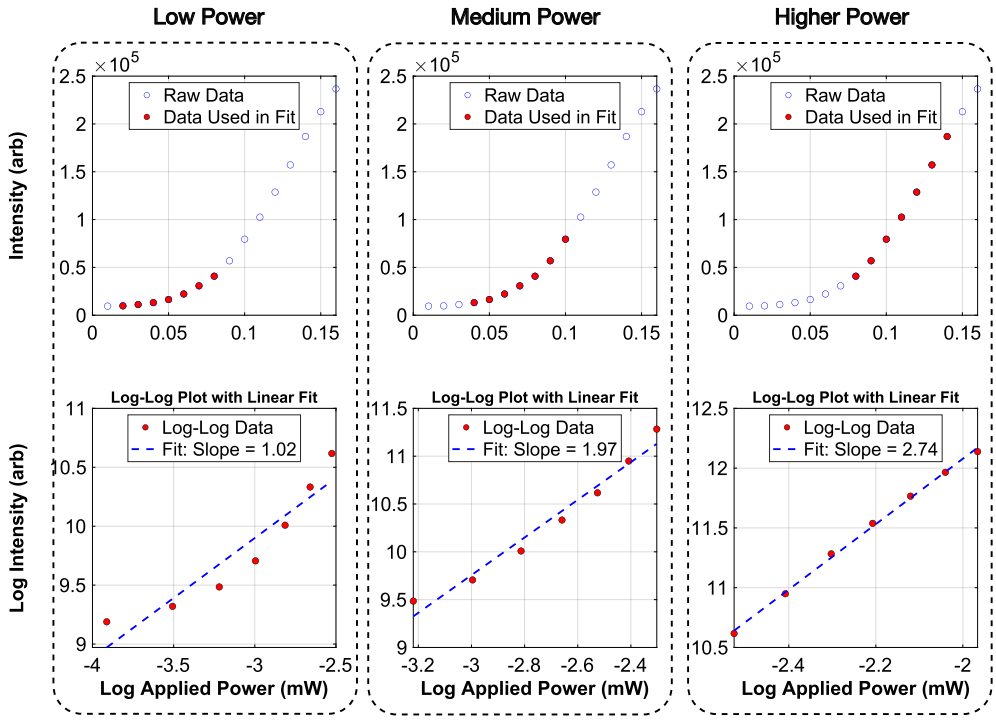

Figure 5.57: Analysis of BBO signal under increasing excitation power. Raw photon counts (top) and corresponding log-log plot (bottom) show distinct power dependence regimes with slopes of 1, 2, and 3.

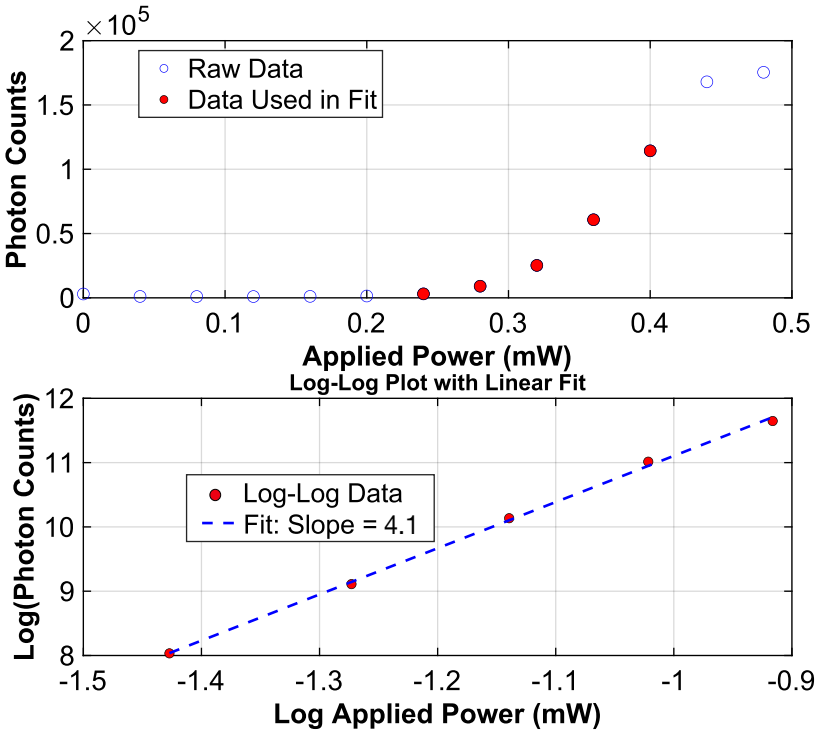

Figure 5.58: Power-scaling measurement of SHG signal using quTAG (quTools). Nonlinear response similar to that in Figure 5.57 confirms the effect is independent of counting hardware. Here a gradient of ≈ 4 is found.

5.4.2 Analysis

The data shown in Figures 5.53 and 5.4 has been analysed using Equations 5.43 and 5.2.3, with results displayed in Figures 5.59–5.61. As stated in Section 5.4, only regions exhibiting quadratic or cubic power dependence were selected for analysis.

It is important to note that for the expressions $\frac{F_M}{\langle P_M \rangle^3}$ and $\frac{F_M}{\langle P_M \rangle^2}$, the slopes were obtained by fitting a line of best fit in MATLAB of the form $y = mx$, rather than the conventional $y = mx + c$. This was done to avoid the unphysical implication of a non-zero fluorescence signal in the absence of excitation power.

A dark count was taken with the PMT biased and the photon counter on and was found to have negligible rates of counting ($<$100) per 30s interval.

Where possible, uncertainties were calculated via error propagation of all contributing parameters; wavelength measurements, laser rep rate, objective NA, power meter, concentration of fluorescent dye, T_{cnt} and ϕ.

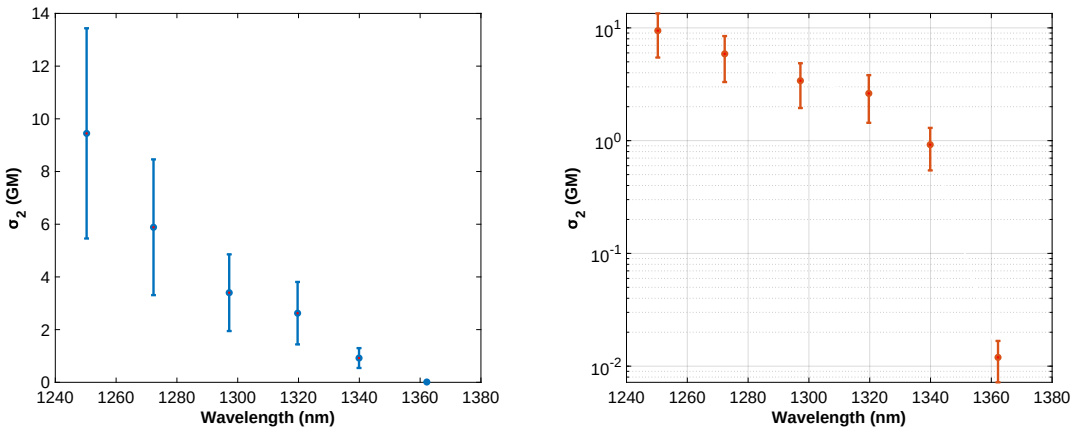

Figure 5.59: Left: Calculated two-photon cross-sectional area of Cy5, given in the units GM (Goeppert-Mayer), where 1 GM = 10^{-50} cm^{4}s/photon. Right: The same data shown on a semi-log plot. For these calculations, a central emission wavelength of 647 nm has been assumed. Dye concentration $C = 10$ μM, repetition rate $f = 125$ kHz, $b_2 = 64.1$, pulse-shape factor $g_p^{(2)} = 0.587$, quantum yield $\phi = 0.51\%$, acquisition time $T_{\text{cnt}} = 30$ s, and transmission calibration factor $T_{\text{cal}} = 0.9$.

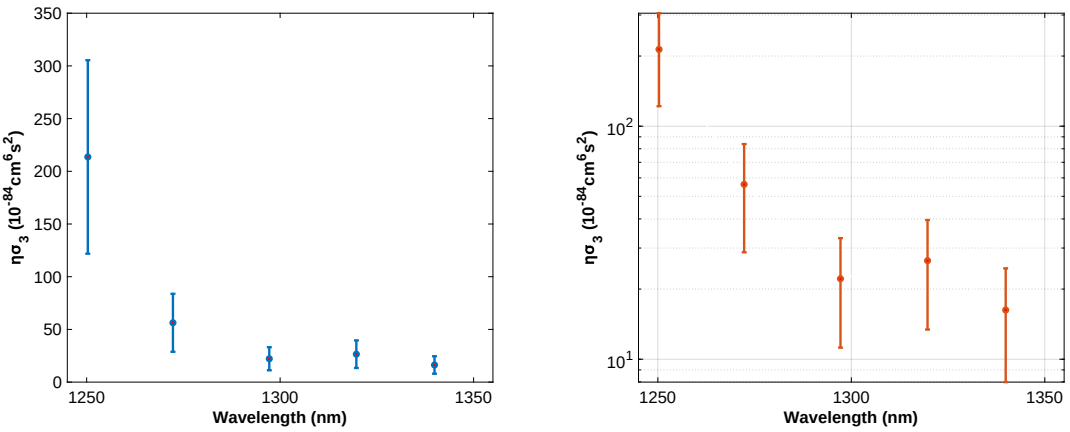

Figure 5.60: Left: Calculated three-photon cross-sectional area of DAPI. Right: Same data plotted on a semi-logarithmic scale. Both are given in units of $\mathrm{cm}^6\,\mathrm{s}^2$. Calculations assume a central emission wavelength of 520 nm and use the following constants: $g_p^{(3)} = 0.41$, quantum yield $\phi = 0.61\%$, dye concentration $C = 100$ μM, repetition rate $f = 1$ MHz, numerical aperture NA $= 0.8$, refractive index $\mathrm{n}_0 = 1.33$, acquisition time $T_{\mathrm{cnt}} = 30$ s, and calibration factor $T_{\mathrm{cal}} = 0.9$.

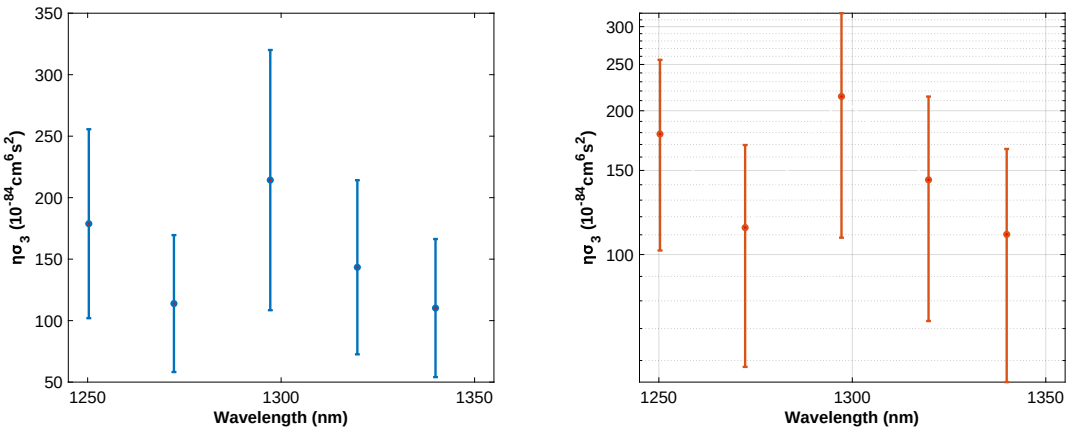

Figure 5.61: Left: Calculated three-photon cross-sectional area of Fluorescein. Right: Same data plotted on a semi-logarithmic scale. Both are given in units of $\mathrm{cm}^6\,\mathrm{s}^2$. Calculations assume a central emission wavelength of 515 nm and use the following constants: $g_p^{(3)} = 0.41$, quantum yield $\phi = 0.60\%$, dye concentration $C = 10\ \mu\mathrm{M}$, repetition rate $f = 500$ kHz, numerical aperture NA $= 0.8$, refractive index $\mathrm{n}_0 = 1.33$, acquisition time $T_{\mathrm{cnt}} = 30$ s, and calibration factor $T_{\mathrm{cal}} = 0.9$.

Wavelength (nm)	Cy5 (GM)	Fluorescein (10^{-84}cm^{6}s^2)	DAPI (10^{-84}cm^{6}s^2)
1250.3	9.45 ± 3.99	178.80 ± 76.82	44.17 ± 18.98
1272.3	5.88 ± 2.58	113.87 ± 55.68	24.56 ± 12.01
1297.2	3.40 ± 1.45	214.28 ± 105.79	14.59 ± 7.20
1319.7	2.62 ± 1.18	143.38 ± 70.79	16.60 ± 8.20
1339.9	0.92 ± 0.38	110.21 ± 56.14	10.70 ± 5.45
1362.2	0.01 ± 0.005	NA	NA

Table 5.8: Full table of calculated action cross sections for all three dyes: Cy5, Fluorescein, and DAPI. Values were obtained using the method described in Section 5.4.2, isolating regions with quadratic and cubic power scaling.

5.5 Discussion of Results

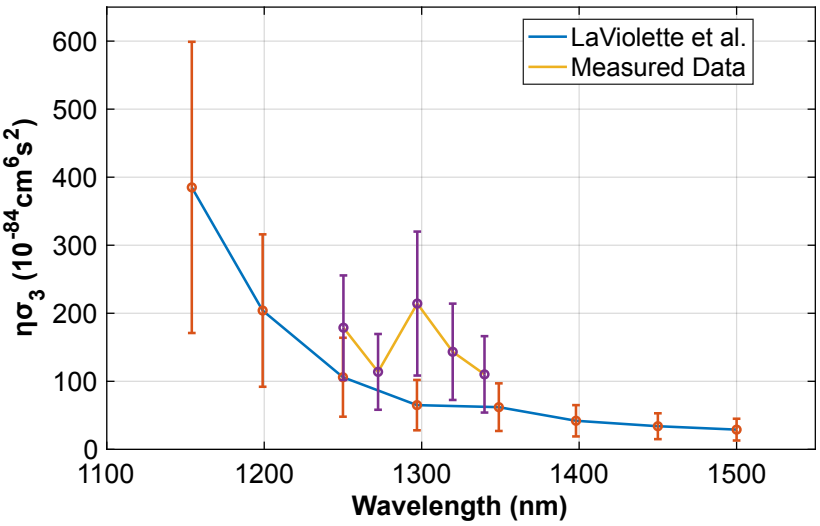

Figure 5.62: Three-photon action cross section for Fluorescein from [38], alongside the measured data.

Due to the scarcity of comparable datasets in the literature, opportunities for

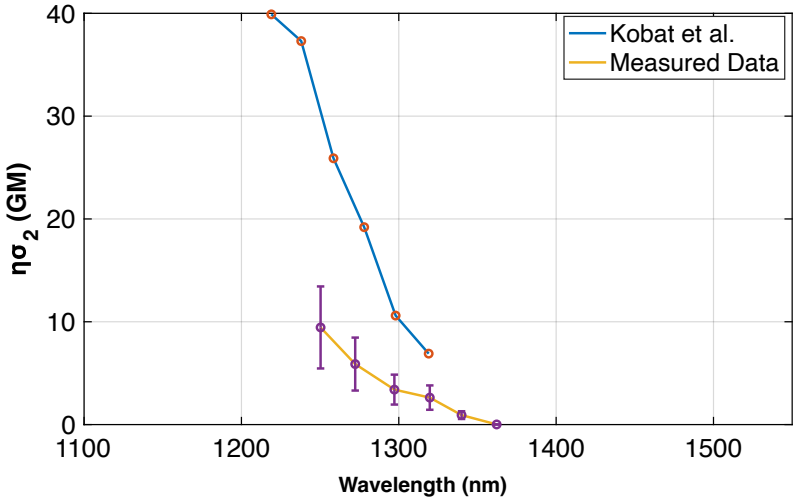

Figure 5.63: Two-photon action cross section for Cy5 from, digitised from [65]

direct benchmarking of our results are limited. Two notable exceptions are the work by La Violette et al and Kobat et al. on Fluorescein [38] and Cy5 [65]. These two data sets have been reproduced in Figure 5.62 and Figure 5.63, with Kobat using the same comparative method as [84]). Their measurements were conducted using Fluorescein from a different manufacturer, prepared at a pH of approximately 11.5 to enhance fluorescence yield. In contrast, our samples were prepared in phosphate-buffered saline at pH 7, mimicking physiologically relevant imaging conditions.

When comparing our Fluorescein results with those of La Violette et al., no consistent wavelength-dependent trend is observed in our data. However, the absolute magnitudes of the calculated action cross sections are within the same order of magnitude. This level of agreement—despite differences in preparation, system calibration, and experimental conditions—provides some confidence in the validity of our methodology and results, given they are in the same ballpark. Accordingly, Fluorescein serves effectively as a control measurement, reinforcing the credibility of our approximate findings for Cy5 and DAPI.

For both Cy5 and DAPI a clear trend emerges in which the measured action cross section increases at shorter excitation wavelengths. This observation aligns qualitatively with the expectation that higher photon energies (shorter wavelengths) appear to move the multiphoton energy closer to an allowed transition in the case of both of these dyes. Additionally, the observed wavelength dependence reflects the intrinsic spectral characteristics of each fluorophore, further supporting the internal consistency of our results. The detailed shape of these trends, however, is governed by molecular-level photophysics, including transition dipole strengths and intermediate-state resonance effects.

Further comparison with literature reveals some divergence. Hontani et al. [88] reported three-photon action cross sections for several red-emitting fluorophores, including Alexa Fluor 546 and Texas Red. While their three-photon values are generally in agreement with our measurements in terms of magnitude, their reported two-photon action cross sections for red-emitting dyes are approximately two orders of magnitude lower than our estimate for Cy5. This discrepancy underscores the sensitivity of multiphoton cross section measurements to various experimental factors, such as excitation repetition rate, pulse width, local environment, dye formulation, solvent, pH, calibration method and reference standard.

Taken together, these comparisons suggest that our experimental setup and analysis methods yield results that are broadly consistent with published literature, while also highlighting areas where methodological differences can lead to variability. This reinforces the need for standardisation and thorough reporting in multiphoton cross section measurements.

5.5.1 Considerations

Several considerations in our experimental design could be improved upon in future iterations to enhance accuracy and reproducibility.

Firstly, the microscope objective used in this study (Nikon N40XW-PF, 40×, NA 0.8) is optimised for ultraviolet to visible wavelengths. While it maintains reasonable transmission into the infrared, its performance beyond 1000 nm may lead to a reduction in the effective numerical aperture (NA) due to chromatic aberrations or altered focusing geometry. This wavelength-dependent degradation is rarely accounted for but can significantly influence focal volume and intensity distributions. Techniques such as the knife-edge method or point spread function (PSF) analysis could be used to directly measure the effective NA at each wavelength of interest [93]. Based on preliminary estimates, the true NA in the infrared may lie closer to 0.7–0.75, rather than the nominal 0.8.

Secondly, our analysis assumes nominal values for the temporal coherence parameters $g_p^{(2)}$ and $g_p^{(3)}$. While these are often treated as fixed constants for Gaussian pulse shapes, they can vary significantly depending on the actual temporal pulse profile and spectral phase distortions. More accurate values could be obtained through direct measurement. For instance, Horikiri et al. [94] demonstrated the use of photon correlation measurements to determine $g^{(2)}$ and $g^{(3)}$ in an exciton-polariton system, revealing measurable deviations from ideal behaviour. More relevant to fluorescence microscopy, La Violette and Xu [38] developed a methodology to extract $g_p^{(n)}$ empirically via nonlinear fluorescence saturation analysis. Incorporating experimentally derived values of $g_p^{(n)}$ would significantly improve the accuracy of the calculated action cross sections by better accounting for pulse temporal characteristics.

Overall, addressing these factors—particularly the effective NA and coherence parameters—would reduce systematic uncertainties and enhance the precision of mul-

tiphoton cross-section measurements.

Similarly, the propagation loss terms b_2 and b_3 could have been treated with greater wavelength specificity. While we used fixed values in our calculations, these parameters are known to vary with wavelength. However, as reported in the literature [1], this variation is typically less than 1%, and thus is unlikely to have introduced significant error into our final results.

The collection efficiency was determined through a theoretical model rather than experimental calibration. While this approach is common in first-pass analyses, it introduces uncertainty—particularly since ϕ contributes multiplicatively to the final cross-section result and spans several orders of magnitude (typically $\sim 10^3$). A more accurate strategy would involve direct experimental measurement of ϕ, which would substantially increase the validity and confidence in our cross-sectional calculations by avoiding the compounded error associated with an assumed value.

Additionally, the axial confinement length (Δz) was not dynamically adjusted during the experiment. Ideally, Δz should reflect the actual excitation volume under the specific optical conditions used, especially considering wavelength-dependent focal behavior. While this factor likely contributes a relatively small correction, its inclusion would improve the precision of the calculated cross-sectional areas, particularly for dyes excited at the extreme ends of our wavelength range.

The filter and dichroic setup used (see Table 5.7) was originally selected for imaging spheroids and organoids stained with DAPI and WGA-AF647. During these initial experiments, it was observed that DAPI displayed a shift in its emission peak, centered around 510 nm—higher than its nominal peak emission. Although not thoroughly characterised, this observation informed our choice of filters and was factored into the wavelength used in subsequent emission calculations.

Finally, issues with photon counting represented the most significant experimen-

tal hurdle in this investigation. Although a clear and reproducible trend was observed for both Cy5 and DAPI, the photon counting artifacts contributed the largest source of systematic uncertainty. Through extensive troubleshooting—including the use of alternative photon counters and consultation with manufacturers—we identified the likely origin of the problem and implemented corrective strategies to minimise its effect on our analysed data.

5.6 Summary

We have determined approximate multiphoton action cross sections for the dyes Cy5, Fluorescein, and DAPI under both two-photon and three-photon excitation, as summarised in Figure 5.64. These results establish a foundation for assessing the wavelength-dependent excitation efficiency of commonly used fluorophores across different nonlinear excitation regimes. Given the extensive number of independent measurements required across varying optical conditions, this characterisation remains experimentally challenging, which partly explains the scarcity of comprehensive three-photon action cross section data in the literature.

Although the reliability of our results is somewhat constrained by challenges related to photon counting, the data nonetheless provide valuable insights into the wavelength dependence of fluorophore excitation efficiency. In principle, combining these cross-sectional measurements with applied power and pulse duration data could enable the determination of optimal excitation wavelengths for each dye. Interestingly, our findings suggest that the optimal excitation wavelength does not always coincide with the shortest pulse duration; rather, we observe increased dye efficiency at shorter excitation wavelengths, despite the longer pulse durations encountered at

these wavelengths.

Future investigations could expand upon these findings by comparing the measured response of Cy5 with that of WGA-AF647. Imaging WGA-AF647–stained spheroids or organoids may offer an avenue to evaluate the applicability of our current results within more complex biological environments.

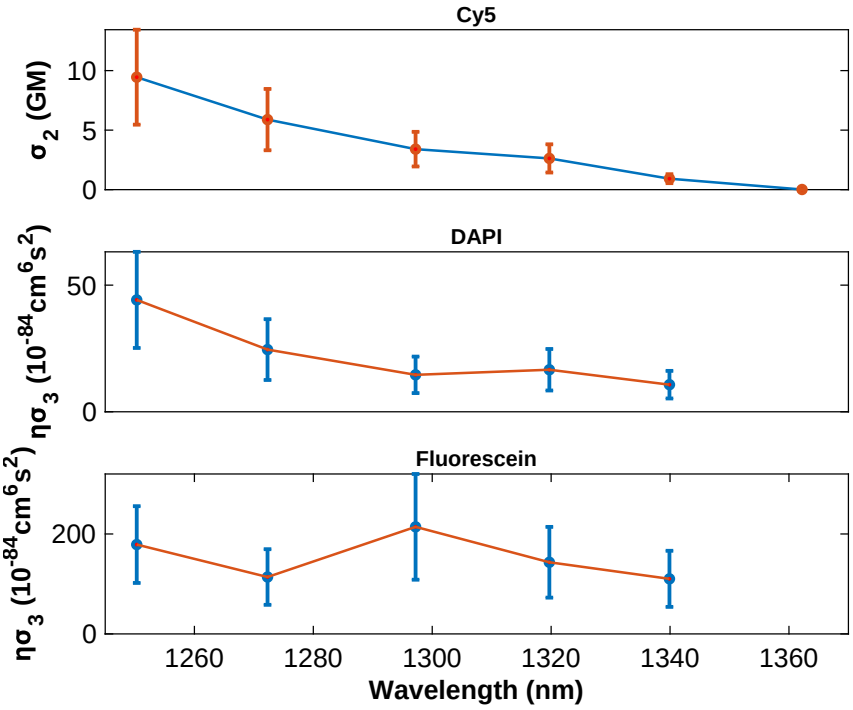

Figure 5.64: Summary of the multiphoton action cross sections determined for the dyes Cy5, DAPI, and Fluorescein.

6. Conclusions and Outlook

The primary aim of this thesis was the development and optimisation of multiphoton microscopy for imaging organoids, with particular emphasis on dispersion management and the establishment of methods for quantifying multiphoton cross-sectional areas.

Conclusions

3. Development of Multi-Photon Microscopy Systems

Following the development of a pulse compressor and autocorrelator pair, the dispersion present in a complex two-photon microscope incorporating remote focusing has been thoroughly characterised and compensated. This correction significantly enhanced the fluorescent signal, enabling more accurate and reliable imaging. Consequently, remote focusing was successfully implemented to monitor action potentials in rabbit hearts as they propagated transmurally, providing high-resolution temporal and spatial insight into cardiac electrophysiology, data shown in [95].

Building upon these advances in managing dispersion within remote-focusing systems, a home-built three-photon microscope was designed, constructed, and comprehensively characterised. Both the spatial and temporal properties of sample illumination were carefully optimised, allowing for the measurement of three-photon

absorption using the same treatment found in Chapter (1.6). Concurrently, the pulse duration and spectral output of the optical parametric amplifier (OPA) were fine-tuned to maximise multiphoton excitation efficiency, with the new presets undergoing the same treatment to measure the pulse duration at the sample with variations in GDD from the compressor. Following these fine tunings the presence of two and three photon absorption was determined and measured, finding that we were indeed exciting using three photon absorption where required. The point spread function (PSF) was initially estimated using fluorescent beads and subsequently re-evaluated using beads with a higher numerical aperture (NA), as described in Chapter 4.2.1. This comparison confirmed that increasing the NA directly improves lateral resolution, validating both the optical design and system performance. In addition to the spatio-temporal analysis preformed a power characterisation was also made of the system, providing a guide to the power used at sample.

The collection efficiency of the system has also been tested. A network of filters and dichroics have been constructed to filter the fluorescent signal into three PMTs. Signal has been acquired and analysed using the commercial Scan Image software (Vidreo Technologies), providing real time image processing.

The successful development and characterisation of the three-photon microscope demonstrates the feasibility of achieving three photon absorption. While further optimisation of pulse management and detection efficiency will enhance performance, this work establishes a strong foundation for future improvements and applications in three photon microscopy.

4. Organoid Imaging with Multiphoton Microscopy

The imaging capabilities of the home-built microscope were successfully applied to both heart tissue and cardiac spheroids and organoids, employing two- and three-

photon excitation to achieve high-resolution imaging. Comparison of the calculated attenuation lengths for these organoids with literature values for mouse brain and other biological tissues shows that organoids exhibit comparable scattering and absorption characteristics under 1300 nm excitation, confirming their suitability for multiphoton imaging. In uncleared organoids, imaging depths of approximately 200µm were consistently achieved, demonstrating that functional imaging of such samples is feasible with the current setup. These findings not only validate the performance of the microscope in biologically relevant three-dimensional samples but have also provided direct feedback to collaborators, contributing to optimised staining procedures and improvements in organoid generation. Overall, the results establish some of the first evidence that multiphoton / three-photon microscopy can reliably image cardiac organoids, supporting structural studies within these complex tissue models [96, 97, 98]. These results are particularly helpful to our collaborators in the School of Cardiovascular and Metabolic Health whom aim to target functional imaging of both spheroids and organoids as well as using them to implant within live tissue moving forward.

5. Action Cross Section

Despite the growing interest in three-photon microscopy, quantitative studies of action cross sections remain limited. Chapter 4.5 addresses this gap by performing long-wavelength characterisation of fluorescein, DAPI and Cy5 using a fully independent method that does not rely on a reference dye. This approach was successfully applied to three commonly used fluorophores—DAPI, Fluorescein, and Cy5—allowing direct assessment of their multiphoton absorption properties around 1300 nm. Notably, the study produced novel and physically consistent values for the three-photon action cross section of DAPI, confirming both the presence and magnitude of three-photon

absorption.

Measured values of the three-photon action cross sections show clear wavelength-dependent trends. For DAPI, the cross section decreases from approximately $44.2 \pm 19.0 \times 10^{-84}$ cm^{6}s^2 at 1250.3 nm to $10.7 \pm 5.5 \times 10^{-84}$ cm^{6}s^2 at 1339.9 nm, reflecting the intrinsic spectral properties of the dye. Fluorescein exhibits a non-monotonic behaviour, with values ranging from $113.9 \pm 55.7 \times 10^{-84}$ cm^{6}s^2 at 1272.3 nm to $214.3 \pm 105.8 \times 10^{-84}$ cm^{6}s^2 at 1297.2 nm. For Cy5, the two-photon cross section decreases steadily from 9.45±3.99 GM at 1250.3 nm to 0.92±0.38 GM at 1339.9 nm, illustrating the reduced efficiency of longer-wavelength excitation for this red-emitting dye. Two-photon measurements of Cy5 also yielded values consistent with literature reports, further validating the experimental methodology.

Comparison with previous studies for Fluorescein and Cy5 indicates that our measurements are broadly comparable with literature values [1], despite differences in sample preparation, pH, and system calibration. Some divergence is observed, particularly for red-emitting dyes under two-photon excitation, highlighting the sensitivity of multiphoton cross-section measurements to experimental factors such as pulse width, repetition rate, local environment, and dye formulation. Systematic considerations—including effective numerical aperture, temporal coherence parameters, photon collection efficiency, and axial confinement length—were carefully accounted for, although they remain sources of uncertainty contributing to overall variability. Photon counting artefacts represented the largest experimental challenge, yet trends were observed across the three photon measurements, confirming the robustness of the results.

Overall, the chapter establishes a reliable, quantitative characterisation of multi-photon excitation efficiency for commonly used fluorescent dyes. The results provide detailed insights into the wavelength dependence of their two- and three-photon ab-

sorption, demonstrating internal consistency across measurements and agreement with literature values where available. These findings represent a substantial contribution to the quantitative understanding of multiphoton processes, particularly for DAPI, and provide a validated foundation for future high-resolution, deep-tissue imaging experiments.

Outlook

3. Three Photon Microscopy

We have made progress in developing three-photon microscopy for deep-tissue imaging. However, further improvements are possible in both multiphoton absorption efficiency and spatial resolution. These enhancements can be achieved through the use of adaptive optics (AO). AO compensates for optical distortions by reshaping the incoming wavefront—typically with a deformable mirror (DM) or a spatial light modulator (SLM)—thereby restoring diffraction-limited focusing within highly scattering biological tissues. This approach has been successfully applied in both two- and three-photon imaging systems to increase imaging depth, improve resolution, and boost signal-to-noise ratio. In the context of three-photon microscopy, AO provides an especially powerful combination. Three-photon excitation already enables deeper penetration into tissue because it uses longer excitation wavelength. However as we have seen, these longer wavelengths are not immune to tissue-induced aberrations, and the cubic dependence of excitation efficiency on focal intensity makes three-photon microscopy even more sensitive to distortions: a small degradation of the focal spot can dramatically reduce signal generation. Thus, wavefront correction is particularly valuable in three-photon microscopy, where even modest improvements in focus quality yield disproportionately large gains in signal strength.

Recent advances illustrate this. Wavefront correction techniques [66, 99, 69] have demonstrated substantial improvements in resolution and brightness at depths beyond 1 mm, enabling functional and structural imaging through intact or minimally thinned skulls. These studies often employ deformable mirrors to apply corrections for low- and high-order aberrations introduced by the tissue, restoring the excitation point spread function and enabling fine structures, such as dendritic spines, to be resolved at depth. In some implementations, adaptive optics not only corrects conventional optical aberrations but also helps mitigate phase distortions associated with third-order dispersion and other pulse-broadening effects, ensuring that ultrashort femtosecond pulses remain temporally compressed at the focal plane. The result is a simultaneous enhancement of spatial resolution, signal strength, and penetration depth, making AO-augmented three-photon microscopy one of the most effective current strategies for deep-tissue imaging in neuroscience and other biological applications.

4. Multiphoton Imaging of Organoids

As organoid research and imaging continue to evolve as an emerging field, future developments in deep-imaging modalities—particularly three-photon microscopy—are poised to extend the achievable imaging depth and resolution in intact organoids, thereby enabling more comprehensive investigations of their structure and function. Such advancements will be essential for interrogating the increasingly complex biological models that organoids now represent. As discussed, further developments in three-photon microscopy hold considerable promise for enhancing penetration depth and intrinsic optical sectioning capabilities. This would, in turn, facilitate the advancement of three-photon imaging of highly scattering samples such as organoids,

with the express aim of enabling the detailed visualisation of entire organoid structures without the need for physical sectioning or optical clearing. This is particularly relevant for functional imaging, where maintaining physiological conditions is essential for accurate measurements of neural or electrophysiological activity. As organoids become increasingly sophisticated models of human development and disease [100], integrating three-photon microscopy with genetically encoded indicators or voltage-sensitive dyes could provide new insights into their functional organisation, analogous to techniques currently employed in cardiac electrophysiology.

Recent work on scattering-aware computational imaging further underscores the importance of correcting optical distortions in thick three-dimensional tissues. For example, Suzuki [101], introduced a method for estimating refractive index distributions in spheroids and applying shift-variant deconvolution to recover high-resolution fluorescence signals at depth. Such approaches could merge with future three-photon implementations by providing computational compensation for residual aberrations and scattering that persist even with optimised optics, benefiting from deeper imaging available with three photon imaging.

Related advances in modelling and inverting complex light-scattering behaviour—such as the Pupil Phase Series framework proposed by Hugonnet *et al.*—demonstrate that forward and inverse scattering models are becoming sufficiently accurate and energy-conserving to reconstruct subcellular features deep within organoids [102]. Incorporating these physically informed models into three-photon reconstruction pipelines may enable deeper and more faithful recovery of structural features without increasing excitation power. Similarly, broader developments in deep-tissue microscopy highlight the role of adaptive optics, pulse-dispersion management, and wavelength optimisation in maximising signal quality while minimising photodam-

age. As summarised by Hsieh *et al.*, innovations across modalities—from confocal to light-sheet—continue to address trade-offs in resolution, imaging depth, phototoxicity, and sample scattering, with particular relevance to complex three-dimensional systems such as organoids and spheroids [103]. These considerations are especially relevant to three-photon microscopy, whose performance depends critically on the careful shaping and delivery of ultrashort pulses.

In parallel, there is growing interest in enabling long-term or live imaging of organoids without compromising viability. Techniques such as on-chip live clearing [104] or high-throughput organoid-handling platforms [105] may help integrate three-photon microscopy into experimental workflows in which dozens or hundreds of organoids are imaged under controlled physiological conditions. These innovations could expand the utility of deep functional imaging for developmental studies, disease modelling, and drug screening - one of the ultimate end goals of spheroid and organoid research. Overall, the convergence of three-photon microscopy with advances in computational imaging, adaptive optics, tissue clearing, and high-throughput organoid manipulation has the potential to shape the next generation of volumetric imaging in organoid systems. By enabling deeper, less invasive, and more physiologically faithful imaging, these technologies show promise to support increasingly detailed investigations of organoid structure and function.

Beyond the likely advancements in raster-scanning three-photon microscopy for organoid imaging, emerging techniques offer the prospect of rapid, non-invasive, and potentially whole-organ imaging. Adaptive optics provides a robust approach for correcting sample-induced aberrations, with demonstrated benefits for both penetration depth and spatial resolution in highly scattering tissues. Complementing this, temporal focusing provides a powerful approach to significantly increasing acquisition speeds and expanding fields of view. It enables wide-field multiphoton imaging

while preserving axial confinement, though it does present challenges in thicker or highly scattering samples, such as reduced penetration and increased out-of-focus background noise

5. Action Cross Section

The quantification of three-photon dyes remains a valuable yet challenging task, requiring accuracy across several aspects of the experiment. This involves not only precise photon counting, but also careful characterisation of pulse duration, spectral bandwidth, and pulse-to-pulse stability. In this study, the dyes under investigation reached the upper limit of their usable excitation wavelength, largely due to a combination of decreasing three-photon absorption efficiency and limitations in signal-to-noise at longer wavelengths. Although there is scope for extending measurements across a broader spectral range, further improvements in instrumentation would be required to do so reliably.

As discussed in Chapter 4.5, Xu and Webb's two-photon studies demonstrated the value of defining a standard reference dye—fluorescein in several cases—which enabled consistent comparison of cross sections across laboratories. A similar standard has not yet emerged for three-photon excitation, due in part to the smaller number of well-characterised fluorophores and the increased sensitivity of the process to pulse properties. Nevertheless, there is strong potential for establishing a reliable reference dye for three-photon measurements. An ideal candidate would be fluorescein, given its extensive use and now twice characterised fluorescence behaviour.

Further refinements could also enhance measurement rigour. In particular, greater control over dispersion and spectral bandwidth would reduce systematic errors. Third-order dispersion within the microscope broadens and distorts the pulse, lowering peak intensity and leading to systematic underestimation of cross sections. Compensating

for this dispersion, or narrowing the optical parametric amplifier (OPA) output to more closely approach the transform-limited pulse, would minimise these effects. Reducing uncertainty related to pulse shape and spectral width would, in turn, improve reproducibility both within and between laboratories.

Taken together, improved dispersion management, stricter control of excitation bandwidth, and the establishment of standard reference dyes would streamline the quantification of three-photon absorption cross sections. These developments would provide a more robust foundation for comparing excitation efficiencies across dyes and would support the broader adoption of three-photon probes in neuroscience and deep-tissue imaging, enabling more reliable cross-laboratory comparisons and broader biological applications.

Bibliography

[1] Aaron K. LaViolette, Dimitre G. Ouzounov, and Chris Xu. "Measurement of three-photon excitation cross-sections of fluorescein from 1154 nm to 1500 nm". en. In: *Biomedical Optics Express* 14.8 (Aug. 2023), p. 4369. ISSN: 2156-7085, 2156-7085. DOI: 10.1364/BOE.498214. URL: https://opg.optica.org/abstract.cfm?URI=boe-14-8-4369 (visited on 02/04/2025).

[2] Amicia D. Elliott. "Confocal Microscopy: Principles and Modern Practices". en. In: *Current Protocols in Cytometry* 92.1 (Mar. 2020), e68. ISSN: 1934-9297, 1934-9300. DOI: 10.1002/cpcy.68. URL: https://currentprotocols.onlinelibrary.wiley.com/doi/10.1002/cpcy.68 (visited on 06/08/2026).

[3] José-Angel Conchello and Jeff W Lichtman. "Optical sectioning microscopy". en. In: *Nature Methods* 2.12 (Dec. 2005), pp. 920–931. ISSN: 1548-7091, 1548-7105. DOI: 10.1038/nmeth815. URL: https://www.nature.com/articles/nmeth815 (visited on 06/08/2026).

[4] Winfried Denk, James H. Strickler, and Watt W. Webb. "Two-Photon Laser Scanning Fluorescence Microscopy". en. In: *Science* 248.4951 (Apr. 1990), pp. 73–76. ISSN: 0036-8075, 1095-9203. DOI: 10.1126/science.2321027. URL: https://www.science.org/doi/10.1126/science.2321027 (visited on 09/03/2025).

[5] Warren R Zipfel, Rebecca M Williams, and Watt W Webb. "Nonlinear magic: multiphoton microscopy in the biosciences". en. In: *Nature Biotechnology* 21.11 (Nov. 2003), pp. 1369–1377. ISSN: 1087-0156, 1546-1696. DOI: 10.1038/nbt899. URL: http://www.nature.com/articles/nbt899 (visited on 03/01/2023).

[6] Maria Göppert-Mayer. "Über Elementarakte mit zwei Quantensprüngen". de. In: *Annalen der Physik* 401.3 (Jan. 1931), pp. 273–294. ISSN: 0003-3804, 1521-3889. DOI: 10.1002/andp.19314010303. URL: https://onlinelibrary.wiley.com/doi/10.1002/andp.19314010303 (visited on 06/08/2026).

[7] Marlan O. Scully and Muhammad Suhail Zubairy. *Quantum optics*. eng. Cambridge New York Melbourne Madrid Cape Town Singapore Sao Paulo Delhi Dubai Tokyo Mexic City: Cambridge University Press, 2008. ISBN: 978-0-521-43458-4 978-1-139-63816-6.

[8] Joseph R. Lakowicz and Barry R. Masters. "Principles of Fluorescence Spectroscopy, Third Edition". en. In: *Journal of Biomedical Optics* 13.2 (2008), p. 029901. ISSN: 10833668. DOI: 10.1117/1.2904580. URL: http://biomedicaloptics.spiedigitallibrary.org/article.aspx?doi=10.1117/1.2904580 (visited on 06/08/2026).

[9] Fritjof Helmchen and Winfried Denk. "Deep tissue two-photon microscopy". en. In: *Nature Methods* 2.12 (Dec. 2005), pp. 932–940. ISSN: 1548-7091, 1548-7105. DOI: 10.1038/nmeth818. URL: https://www.nature.com/articles/nmeth818 (visited on 09/03/2025).

[10] Sergey Polyakov. *Experimental Methods in the Physical Sciences*. en. Vol. 45. Elsevier, 2013. ISBN: 978-0-12-387695-9. DOI: 10.1016/B978-0-12-387695-

9.00003-2. URL: https://linkinghub.elsevier.com/retrieve/pii/B9780123876959000032 (visited on 06/08/2026).

[11] X. Michalet et al. "Hybrid photodetector for single-molecule spectroscopy and microscopy". en. In: ed. by Jörg Enderlein, Zygmunt K. Gryczynski, and Rainer Erdmann. San Jose, CA, Feb. 2008, 68620F. DOI: 10.1117/12.763449. URL: http://proceedings.spiedigitallibrary.org/proceeding.aspx?doi=10.1117/12.763449 (visited on 06/08/2026).

[12] James Pawley. *Handbook of Biological Confocal Microscopy*. en. New York, NY: Springer, 1995. ISBN: 978-0-306-43538-6 978-1-4615-7133-9.

[13] Lei Wang et al. "Improvement in Resolution of Multiphoton Scanning Structured Illumination Microscopy via Harmonics". en. In: *Engineering* 16 (Sept. 2022), pp. 65–72. ISSN: 20958099. DOI: 10.1016/j.eng.2021.12.010. URL: https://linkinghub.elsevier.com/retrieve/pii/S2095809922000194 (visited on 09/03/2025).

[14] Chen-Yuan Dong, Karsten Koenig, and Peter So. "Characterizing point spread functions of two-photon fluorescence microscopy in turbid medium". en. In: *Journal of Biomedical Optics* 8.3 (2003), p. 450. ISSN: 10833668. DOI: 10.1117/1.1578644. URL: http://biomedicaloptics.spiedigitallibrary.org/article.aspx?doi=10.1117/1.1578644 (visited on 09/03/2025).

[15] Jörg Mütze et al. "Excitation Spectra and Brightness Optimization of Two-Photon Excited Probes". en. In: *Biophysical Journal* 102.4 (Feb. 2012), pp. 934–944. ISSN: 00063495. DOI: 10.1016/j.bpj.2011.12.056. URL: https://linkinghub.elsevier.com/retrieve/pii/S000634951200063X (visited on 09/03/2025).

[16] Robert W. Boyd. *Nonlinear optics*. en. Fourth edition. London: Elsevier, AP Academic Press, 2020. ISBN: 978-0-12-811002-7 978-0-12-811003-4. DOI: 10.1016/C2015-0-05510-1.

[17] Jean-Claude Diels and Wolfgang Rudolph. *Ultrashort laser pulse phenomena: fundamentals, techniques, and applications on a femtosecond time scale*. en. Second edition. Amsterdam Boston Heidelberg: Academic Press, an Imprint of Elsevier, 2006. ISBN: 978-0-12-215493-5.

[18] Ferenc Krausz and Misha Ivanov. "Attosecond physics". en. In: *Reviews of Modern Physics* 81.1 (Feb. 2009), pp. 163–234. ISSN: 0034-6861, 1539-0756. DOI: 10.1103/RevModPhys.81.163. URL: https://link.aps.org/doi/10.1103/RevModPhys.81.163 (visited on 06/08/2026).

[19] Orazio Svelto. *Principles of Lasers*. en. Boston, MA: Springer US, 2010. ISBN: 978-1-4419-1301-2 978-1-4419-1302-9. DOI: 10.1007/978-1-4419-1302-9. URL: http://link.springer.com/10.1007/978-1-4419-1302-9 (visited on 06/08/2026).

[20] P. F. Moulton. "Spectroscopic and laser characteristics of Ti:Al_2O_3". en. In: *Journal of the Optical Society of America B* 3.1 (Jan. 1986), p. 125. ISSN: 0740-3224, 1520-8540. DOI: 10.1364/JOSAB.3.000125. URL: https://opg.optica.org/abstract.cfm?URI=josab-3-1-125 (visited on 06/08/2026).

[21] C. Xu and F. W. Wise. "Recent advances in fibre lasers for nonlinear microscopy". en. In: *Nature Photonics* 7.11 (Nov. 2013), pp. 875–882. ISSN: 1749-4885, 1749-4893. DOI: 10.1038/nphoton.2013.284. URL: https://www.nature.com/articles/nphoton.2013.284 (visited on 06/08/2026).

[22] Claude Rullière, ed. *Femtosecond laser pulses: principles and experiments*. eng. 2. ed., [repr.] New York: Springer, 2010. ISBN: 978-1-4419-1850-5.

[23] Weichao Wang et al. "Origin and effect of high-order dispersion in ultrashort pulse multiphoton microscopy in the 10 fs regime". en. In: *Applied Optics* 49.35 (Dec. 2010), p. 6703. ISSN: 0003-6935, 1539-4522. DOI: 10.1364/AO.49.006703. URL: https://opg.optica.org/abstract.cfm?URI=ao-49-35-6703 (visited on 06/08/2026).

[24] Stefan W. Hell. "Three-photon excitation in fluorescence microscopy". en. In: *Journal of Biomedical Optics* 1.1 (1996), p. 71. ISSN: 10833668. DOI: 10.1117/12.229062. URL: http://biomedicaloptics.spiedigitallibrary.org/article.aspx?doi=10.1117/12.229062 (visited on 06/19/2025).

[25] Michael E Durst, Demirhan Kobat, and Chris Xu. "Tunable dispersion compensation by a rotating cylindrical lens". en. In: ().

[26] A. M. Weiner. "Femtosecond pulse shaping using spatial light modulators". en. In: *Review of Scientific Instruments* 71.5 (May 2000), pp. 1929–1960. ISSN: 0034-6748, 1089-7623. DOI: 10.1063/1.1150614. URL: https://pubs.aip.org/rsi/article/71/5/1929/436146/Femtosecond-pulse-shaping-using-spatial-light (visited on 06/08/2026).

[27] Jess M. Gunn et al. "The MIIPS method for simultaneous phase measurement and compensation of femtosecond laser pulses and its role in two-photon microscopy and imaging". en. In: ed. by Joseph Neev et al. San Jose, CA, Feb. 2006, p. 61080C. DOI: 10.1117/12.659795. URL: http://proceedings.spiedigitallibrary.org/proceeding.aspx?doi=10.1117/12.659795 (visited on 06/08/2026).

[28] Peter Rupprecht et al. "Remote z-scanning with a macroscopic voice coil motor for fast 3D multiphoton laser scanning microscopy". In: *Biomedical Optics Express* 7.5 (Apr. 2016), pp. 1656–1671. ISSN: 2156-7085. DOI: 10.1364/

BOE.7.001656. URL: https://www.ncbi.nlm.nih.gov/pmc/articles/PMC4871072/ (visited on 05/05/2022).

[29] Wenzhi Hong, Hugh Sparks, and Chris Dunsby. "Alignment and characterization of remote-refocusing systems". en. In: *Applied Optics* 62.28 (Oct. 2023), p. 7431. ISSN: 1559-128X, 2155-3165. DOI: 10.1364/AO.500281. URL: https://opg.optica.org/abstract.cfm?URI=ao-62-28-7431 (visited on 08/13/2025).

[30] Edward J. Botcherby et al. "Aberration-free three-dimensional multiphoton imaging of neuronal activity at kHz rates". en. In: *Proceedings of the National Academy of Sciences* 109.8 (Feb. 2012), pp. 2919–2924. ISSN: 0027-8424, 1091-6490. DOI: 10.1073/pnas.1111662109. URL: https://pnas.org/doi/full/10.1073/pnas.1111662109 (visited on 08/13/2025).

[31] Francesca Anselmi et al. "Three-dimensional imaging and photostimulation by remote-focusing and holographic light patterning". en. In: *Proceedings of the National Academy of Sciences* 108.49 (Dec. 2011), pp. 19504–19509. ISSN: 0027-8424, 1091-6490. DOI: 10.1073/pnas.1109111108. URL: https://pnas.org/doi/full/10.1073/pnas.1109111108 (visited on 08/13/2025).

[32] Giedre Astrauskaite et al. "Remote focusing for 2-photon microscopy to follow action potential propagation transmurally in acute rabbit cardiac slices". en. In: *Multiphoton Microscopy in the Biomedical Sciences XXIV*. Ed. by Ammasi Periasamy, Peter T. So, and Karsten König. San Francisco, United States: SPIE, Mar. 2024, p. 67. ISBN: 978-1-5106-6953-6 978-1-5106-6954-3. DOI: 10.1117/12.3002956. URL: https://www.spiedigitallibrary.org/conference-proceedings-of-spie/12847/3002956/Remote-focusing-

for-2-photon-microscopy-to-follow-action-potential/10.1117/12.3002956.full (visited on 08/12/2025).

[33] Rick Trebino et al. "Measuring ultrashort laser pulses in the time-frequency domain using frequency-resolved optical gating". en. In: *Review of Scientific Instruments* 68.9 (Sept. 1997), pp. 3277–3295. ISSN: 0034-6748, 1089-7623. DOI: 10.1063/1.1148286. URL: http://aip.scitation.org/doi/10.1063/1.1148286 (visited on 10/31/2022).

[34] Ian A. Walmsley and Christophe Dorrer. "Characterization of ultrashort electromagnetic pulses". en. In: *Advances in Optics and Photonics* 1.2 (Apr. 2009), p. 308. ISSN: 1943-8206. DOI: 10.1364/AOP.1.000308. URL: https://opg.optica.org/aop/abstract.cfm?uri=aop-1-2-308 (visited on 06/08/2026).

[35] Yoshihiro Takagi et al. "Multiple- and single-shot autocorrelator based on two-photon conductivity in semiconductors". en. In: *Optics Letters* 17.9 (May 1992), p. 658. ISSN: 0146-9592, 1539-4794. DOI: 10.1364/OL.17.000658. URL: https://opg.optica.org/abstract.cfm?URI=ol-17-9-658 (visited on 08/19/2025).

[36] D. T. Reid et al. "Light-emitting diodes as measurement devices for femtosecond laser pulses". en. In: *Optics Letters* 22.4 (Feb. 1997), p. 233. ISSN: 0146-9592, 1539-4794. DOI: 10.1364/OL.22.000233. URL: https://opg.optica.org/abstract.cfm?URI=ol-22-4-233 (visited on 05/12/2022).

[37] Chris Xu et al. "Determination of absolute two-photon excitation cross sections by in situ second-order autocorrelation". en. In: *Optics Letters* 20.23 (Dec. 1995), p. 2372. ISSN: 0146-9592, 1539-4794. DOI: 10.1364/OL.20.002372. URL: https://opg.optica.org/abstract.cfm?URI=ol-20-23-2372 (visited on 07/01/2025).

[38] Aaron K. LaViolette, Mihailo R. Rebec, and Chris Xu. "Measurement of third order coherence by in situ autocorrelation for determining three-photon cross-sections". en. In: *Biomedical Optics Express* 15.6 (June 2024), p. 3555. ISSN: 2156-7085, 2156-7085. DOI: 10.1364/BOE.521529. URL: https://opg.optica.org/abstract.cfm?URI=boe-15-6-3555 (visited on 07/04/2025).

[39] Selcuk Akturk et al. "Extremely simple single-prism ultrashort- pulse compressor". en. In: *Optics Express* 14.21 (2006), p. 10101. ISSN: 1094-4087. DOI: 10.1364/OE.14.010101. URL: https://opg.optica.org/oe/abstract.cfm?uri=oe-14-21-10101 (visited on 01/30/2023).

[40] R. L. Fork, O. E. Martinez, and J. P. Gordon. "Negative dispersion using pairs of prisms". en. In: *Optics Letters* 9.5 (May 1984), p. 150. ISSN: 0146-9592, 1539-4794. DOI: 10.1364/OL.9.000150. URL: https://opg.optica.org/abstract.cfm?URI=ol-9-5-150 (visited on 01/30/2023).

[41] Lingjie Kong and Meng Cui. *A high throughput (>90%), large compensation range, single-prism femtosecond pulse compressor*. arXiv:1306.5011 [physics]. June 2013. URL: http://arxiv.org/abs/1306.5011 (visited on 08/16/2022).

[42] Nicholas G. Horton et al. "In vivo three-photon microscopy of subcortical structures within an intact mouse brain". en. In: *Nature Photonics* 7.3 (Mar. 2013), pp. 205–209. ISSN: 1749-4885, 1749-4893. DOI: 10.1038/nphoton.2012.336. URL: http://www.nature.com/articles/nphoton.2012.336 (visited on 03/15/2022).

[43] Hanieh Fattahi et al. "Third-generation femtosecond technology". en. In: *Optica* 1.1 (July 2014), p. 45. ISSN: 2334-2536. DOI: 10.1364/OPTICA.1.000045. URL: https://opg.optica.org/abstract.cfm?URI=optica-1-1-45 (visited on 06/08/2026).

[44] Tal Sneh et al. "Optical tweezing of microparticles and cells using silicon-photonics-based optical phased arrays". en. In: *Nature Communications* 15.1 (Oct. 2024), p. 8493. ISSN: 2041-1723. DOI: 10.1038/s41467-024-52273-x. URL: https://www.nature.com/articles/s41467-024-52273-x (visited on 09/04/2025).

[45] Samuel T. Hess and Watt W. Webb. "Focal Volume Optics and Experimental Artifacts in Confocal Fluorescence Correlation Spectroscopy". en. In: *Biophysical Journal* 83.4 (Oct. 2002), pp. 2300–2317. ISSN: 00063495. DOI: 10.1016/S0006-3495(02)73990-8. URL: https://linkinghub.elsevier.com/retrieve/pii/S0006349502739908 (visited on 09/04/2025).

[46] Anthony E. Siegman. *Lasers*. eng. Mill Valley, California: University Science Books, 1986. ISBN: 978-0-935702-11-8 978-0-19-855713-5.

[47] Woochan Kim et al. "Therapeutic strategies of three-dimensional stem cell spheroids and organoids for tissue repair and regeneration". en. In: *Bioactive Materials* 19 (Jan. 2023). Publisher: Elsevier BV, pp. 50–74. ISSN: 2452-199X. DOI: 10.1016/j.bioactmat.2022.03.039. URL: https://linkinghub.elsevier.com/retrieve/pii/S2452199X22001554 (visited on 07/10/2025).

[48] Hans Clevers. "Modeling Development and Disease with Organoids". en. In: *Cell* 165.7 (June 2016). Publisher: Elsevier BV, pp. 1586–1597. ISSN: 0092-8674. DOI: 10.1016/j.cell.2016.05.082. URL: https://linkinghub.elsevier.com/retrieve/pii/S0092867416307292 (visited on 07/10/2025).

[49] Mark A. Skylar-Scott et al. "Biomanufacturing of organ-specific tissues with high cellular density and embedded vascular channels". en. In: *Science Advances* 5.9 (Sept. 2019). Publisher: American Association for the Advancement of Science (AAAS). ISSN: 2375-2548. DOI: 10.1126/sciadv.aaw2459.

URL: https://www.science.org/doi/10.1126/sciadv.aaw2459 (visited on 07/10/2025).

[50] Hannah A. Strobel, Sarah M. Moss, and James B. Hoying. "Methods for vascularization and perfusion of tissue organoids". en. In: *Mammalian Genome* 33.3 (Sept. 2022), pp. 437–450. ISSN: 0938-8990, 1432-1777. DOI: 10.1007/s00335-022-09951-2. URL: https://link.springer.com/10.1007/s00335-022-09951-2 (visited on 08/12/2025).

[51] Jason S. Jones, David M. Small, and Nozomi Nishimura. "In Vivo Calcium Imaging of Cardiomyocytes in the Beating Mouse Heart With Multiphoton Microscopy". en. In: *Frontiers in Physiology* 9 (July 2018), p. 969. ISSN: 1664-042X. DOI: 10.3389/fphys.2018.00969. URL: https://www.frontiersin.org/article/10.3389/fphys.2018.00969/full (visited on 08/12/2025).

[52] Soyeon Ahn, Jung-yeon Yoon, and Pilhan Kim. "Intravital imaging of cardiac tissue utilizing tissue-stabilized heart window chamber in live animal model". en. In: *European Heart Journal - Imaging Methods and Practice* 2.1 (Jan. 2024), qyae062. ISSN: 2755-9637. DOI: 10.1093/ehjimp/qyae062. URL: https://academic.oup.com/ehjimp/article/doi/10.1093/ehjimp/qyae062/7701992 (visited on 08/12/2025).

[53] Madeline A. Lancaster and Juergen A. Knoblich. "Organogenesis in a dish: Modeling development and disease using organoid technologies". en. In: *Science* 345.6194 (July 2014), p. 1247125. ISSN: 0036-8075, 1095-9203. DOI: 10.1126/science.1247125. URL: https://www.science.org/doi/10.1126/science.1247125 (visited on 06/08/2026).

[54] Pablo Hofbauer et al. "Cardioids reveal self-organizing principles of human cardiogenesis". en. In: *Cell* 184.12 (June 2021), 3299–3317.e22. ISSN: 00928674.

DOI: 10.1016/j.cell.2021.04.034. URL: https://linkinghub.elsevier.com/retrieve/pii/S0092867421005377 (visited on 06/08/2026).

[55] Jaeyeaon Cho et al. "From engineered heart tissue to cardiac organoid". en. In: *Theranostics* 12.6 (2022), pp. 2758–2772. ISSN: 1838-7640. DOI: 10.7150/thno.67661. URL: https://www.thno.org/v12p2758.htm (visited on 08/12/2025).

[56] Caleb Jensen and Yong Teng. "Is It Time to Start Transitioning From 2D to 3D Cell Culture?" en. In: *Frontiers in Molecular Biosciences* 7 (Mar. 2020), p. 33. ISSN: 2296-889X. DOI: 10.3389/fmolb.2020.00033. URL: https://www.frontiersin.org/article/10.3389/fmolb.2020.00033/full (visited on 06/08/2026).

[57] Douglas S. Richardson and Jeff W. Lichtman. "Clarifying Tissue Clearing". en. In: *Cell* 162.2 (July 2015), pp. 246–257. ISSN: 00928674. DOI: 10.1016/j.cell.2015.06.067. URL: https://linkinghub.elsevier.com/retrieve/pii/S0092867415008375 (visited on 06/08/2026).

[58] Kazuki Tainaka et al. "Chemical Principles in Tissue Clearing and Staining Protocols for Whole-Body Cell Profiling". en. In: *Annual Review of Cell and Developmental Biology* 32.1 (Oct. 2016), pp. 713–741. ISSN: 1081-0706, 1530-8995. DOI: 10.1146/annurev-cellbio-111315-125001. URL: https://www.annualreviews.org/doi/10.1146/annurev-cellbio-111315-125001 (visited on 06/08/2026).

[59] Hiroki R. Ueda et al. "Tissue clearing and its applications in neuroscience". en. In: *Nature Reviews Neuroscience* 21.2 (Feb. 2020), pp. 61–79. ISSN: 1471-003X, 1471-0048. DOI: 10.1038/s41583-019-0250-1. URL: https://www.nature.com/articles/s41583-019-0250-1 (visited on 06/08/2026).

[60] Wouter Masselink et al. "Broad applicability of a streamlined Ethyl Cinnamate-based clearing procedure". en. In: *Development* (Jan. 2019), dev.166884. ISSN: 1477-9129, 0950-1991. DOI: 10.1242/dev.166884. URL: https://journals.biologists.com/dev/article/doi/10.1242/dev.166884/264754/Broad-applicability-of-a-streamlined-Ethyl (visited on 06/08/2026).

[61] Johanna F. Dekkers et al. "High-resolution 3D imaging of fixed and cleared organoids". en. In: *Nature Protocols* 14.6 (June 2019), pp. 1756–1771. ISSN: 1754-2189, 1750-2799. DOI: 10.1038/s41596-019-0160-8. URL: https://www.nature.com/articles/s41596-019-0160-8 (visited on 06/08/2026).

[62] *Fluorescence SpectraViewer*. URL: https://www.thermofisher.com/order/fluorescence-spectraviewer/ (visited on 07/10/2025).

[63] Mengran Wang et al. "Comparing the effective attenuation lengths for long wavelength in vivo imaging of the mouse brain". en. In: *Biomedical Optics Express* 9.8 (Aug. 2018), p. 3534. ISSN: 2156-7085, 2156-7085. DOI: 10.1364/BOE.9.003534. URL: https://opg.optica.org/abstract.cfm?URI=boe-9-8-3534 (visited on 03/25/2022).

[64] Yusaku Hontani et al. "Deep-Tissue Three-Photon Fluorescence Microscopy in Intact Mouse and Zebrafish Brain". en. In: *Journal of Visualized Experiments* 179 (Jan. 2022), p. 63213. ISSN: 1940-087X. DOI: 10.3791/63213. URL: https://app.jove.com/t/63213 (visited on 04/11/2025).

[65] Demirhan Kobat et al. "Deep tissue multiphoton microscopy using longer wavelength excitation". en. In: *Optics Express* 17.16 (Aug. 2009), p. 13354. ISSN: 1094-4087. DOI: 10.1364/OE.17.013354. URL: https://opg.optica.org/oe/abstract.cfm?uri=oe-17-16-13354 (visited on 11/24/2024).

[66] Lina Streich et al. "High-resolution structural and functional deep brain imaging using adaptive optics three-photon microscopy". en. In: *Nature Methods* 18.10 (Oct. 2021), pp. 1253–1258. ISSN: 1548-7091, 1548-7105. DOI: 10.1038/s41592-021-01257-6. URL: https://www.nature.com/articles/s41592-021-01257-6 (visited on 04/11/2025).

[67] Murat Yildirim et al. "Functional imaging of visual cortical layers and subplate in awake mice with optimized three-photon microscopy". en. In: *Nature Communications* 10.1 (Jan. 2019), p. 177. ISSN: 2041-1723. DOI: 10.1038/s41467-018-08179-6. URL: https://www.nature.com/articles/s41467-018-08179-6 (visited on 08/05/2025).

[68] Yu-Ting Cheng et al. *Three-photon excited fluorescence microscopy enables imaging of blood flow, neural structure and inflammatory response deep into mouse spinal cord in vivo*. en. June 2024. DOI: 10.7554/eLife.95804.1. URL: https://elifesciences.org/reviewed-preprints/95804v1 (visited on 08/05/2025).

[69] David Sinefeld et al. "Three-Photon Adaptive Optics for Mouse Brain Imaging". en. In: *Frontiers in Neuroscience* 16 (May 2022), p. 880859. ISSN: 1662-453X. DOI: 10.3389/fnins.2022.880859. URL: https://www.frontiersin.org/articles/10.3389/fnins.2022.880859/full (visited on 08/12/2025).

[70] Bernhard Rauer et al. "Scattering correcting wavefront shaping for three-photon microscopy". en. In: *Optics Letters* 47.23 (Dec. 2022). arXiv:2206.13191 [physics], p. 6233. ISSN: 0146-9592, 1539-4794. DOI: 10.1364/OL.468834. URL: http://arxiv.org/abs/2206.13191 (visited on 08/12/2025).

[71] Keisuke Toda et al. "Temporal focusing microscopy using three-photon excitation fluorescence with a 92-fs Yb-fiber chirped pulse amplifier". en. In:

Biomedical Optics Express 8.6 (June 2017), p. 2796. ISSN: 2156-7085, 2156-7085. DOI: 10.1364/BOE.8.002796. URL: https://opg.optica.org/abstract.cfm?URI=boe-8-6-2796 (visited on 11/27/2024).

[72] Keisuke Toda et al. "Interferometric temporal focusing microscopy using three-photon excitation fluorescence". en. In: *Biomedical Optics Express* 9.4 (Apr. 2018), p. 1510. ISSN: 2156-7085, 2156-7085. DOI: 10.1364/BOE.9.001510. URL: https://opg.optica.org/abstract.cfm?URI=boe-9-4-1510 (visited on 08/12/2025).

[73] Michael E. Durst et al. "Remote focusing in a temporal focusing microscope". en. In: *OSA Continuum* 4.11 (Nov. 2021), p. 2757. ISSN: 2578-7519. DOI: 10.1364/OSAC.443116. URL: https://opg.optica.org/abstract.cfm?URI=osac-4-11-2757 (visited on 11/20/2023).

[74] B. Leshem et al. "When can temporally focused excitation be axially shifted by dispersion?" en. In: *Optics Express* 22.6 (Mar. 2014), p. 7087. ISSN: 1094-4087. DOI: 10.1364/OE.22.007087. URL: https://opg.optica.org/oe/abstract.cfm?uri=oe-22-6-7087 (visited on 01/08/2024).

[75] Chris Xu and Watt W. Webb. "Multiphoton Excitation of Molecular Fluorophores and Nonlinear Laser Microscopy". en. In: *Topics in Fluorescence Spectroscopy*. Ed. by Joseph R. Lakowicz. Boston, MA: Springer US, 2002, pp. 471–540. ISBN: 978-0-306-45553-7 978-0-306-47070-7. DOI: 10.1007/0-306-47070-5_11. URL: http://link.springer.com/10.1007/0-306-47070-5_11 (visited on 06/19/2025).

[76] Peter T. C. So et al. "Two-Photon Excitation Fluorescence Microscopy". en. In: *Annual Review of Biomedical Engineering* 2.1 (Aug. 2000), pp. 399–429. ISSN: 1523-9829, 1545-4274. DOI: 10.1146/annurev.bioeng.2.1.399. URL:

https://www.annualreviews.org/doi/10.1146/annurev.bioeng.2.1.399 (visited on 06/08/2026).

[77] M. Drobizhev et al. "Absolute Two-Photon Absorption Spectra and Two-Photon Brightness of Orange and Red Fluorescent Proteins". en. In: *The Journal of Physical Chemistry B* 113.4 (Jan. 2009), pp. 855–859. ISSN: 1520-6106, 1520-5207. DOI: 10.1021/jp8087379. URL: https://pubs.acs.org/doi/10.1021/jp8087379 (visited on 07/04/2025).

[78] Chris Xu and Watt W. Webb. "Measurement of two-photon excitation cross sections of molecular fluorophores with data from 690 to 1050 nm". en. In: *Journal of the Optical Society of America B* 13.3 (Mar. 1996), p. 481. ISSN: 0740-3224, 1520-8540. DOI: 10.1364/JOSAB.13.000481. URL: https://opg.optica.org/abstract.cfm?URI=josab-13-3-481 (visited on 01/06/2025).

[79] S. Venugopal Rao, N.K.M. Naga Srinivas, and D. Narayana Rao. "Nonlinear absorption and excited state dynamics in Rhodamine B studied using Z-scan and degenerate four wave mixing techniques". en. In: *Chemical Physics Letters* 361.5-6 (Aug. 2002), pp. 439–445. ISSN: 00092614. DOI: 10.1016/S0009-2614(02)00928-4. URL: https://linkinghub.elsevier.com/retrieve/pii/S0009261402009284 (visited on 07/04/2025).

[80] B. Anusha et al. "Nonlinear Optical Features of Phenol Red Dye in Different Solvent Media Using Z-scan and Density Functional Theory". en. In: *Journal of Fluorescence* (Mar. 2025). ISSN: 1573-4994. DOI: 10.1007/s10895-025-04224-y. URL: https://link.springer.com/10.1007/s10895-025-04224-y (visited on 07/04/2025).

[81] Paul Newman Butcher and David Cotter. *The elements of nonlinear optics*. en. 1. paperback ed., repr. Cambridge studies in modern optics 9. Cambridge: Cambridge Univ. Pr, 1998. ISBN: 978-0-521-34183-7 978-0-521-42424-0.

[82] Gerhard A Blab et al. "Two-photon excitation action cross-sections of the auto¯uorescent proteins". en. In: *Chemical Physics Letters* (2001).

[83] Chris Xu et al. "Multiphoton excitation cross-sections of molecular fluorophores". en. In: *Bioimaging* 4.3 (Sept. 1996), pp. 198–207. ISSN: 09669051, 13616374. DOI: 10.1002/1361-6374(199609)4:3<198::AID-BIO10>3.0.CO;2-X. URL: https://onlinelibrary.wiley.com/doi/10.1002/1361-6374(199609)4:3%3C198::AID-BIO10%3E3.0.CO;2-X (visited on 02/24/2025).

[84] Marius A. Albota, Chris Xu, and Watt W. Webb. "Two-photon fluorescence excitation cross sections of biomolecular probes from 690 to 960 nm". en. In: *Applied Optics* 37.31 (Nov. 1998), p. 7352. ISSN: 0003-6935, 1539-4522. DOI: 10.1364/AO.37.007352. URL: https://opg.optica.org/abstract.cfm?URI=ao-37-31-7352 (visited on 07/04/2025).

[85] Nikolay S. Makarov, Mikhail Drobizhev, and Aleksander Rebane. "Two-photon absorption standards in the 550-1600 nm excitation wavelength range". en. In: *Optics Express* 16.6 (Mar. 2008), p. 4029. ISSN: 1094-4087. DOI: 10.1364/OE.16.004029. URL: https://opg.optica.org/oe/abstract.cfm?uri=oe-16-6-4029 (visited on 06/08/2026).

[86] Guang S. He et al. "Three-photon-absorption-induced fluorescence and optical limiting effects in an organic compound". en. In: *Optics Letters* 20.14 (July 1995), p. 1524. ISSN: 0146-9592, 1539-4794. DOI: 10.1364/OL.20.001524. URL: https://opg.optica.org/abstract.cfm?URI=ol-20-14-1524 (visited on 06/19/2025).

[87] Khmaies Guesmi et al. "Dual-color deep-tissue three-photon microscopy with a multiband infrared laser". en. In: *Light: Science & Applications* 7.1 (June 2018), p. 12. ISSN: 2047-7538. DOI: 10.1038/s41377-018-0012-2. URL: https://www.nature.com/articles/s41377-018-0012-2 (visited on 06/08/2026).

[88] Yusaku Hontani, Fei Xia, and Chris Xu. "Multicolor three-photon fluorescence imaging with single-wavelength excitation deep in mouse brain". en. In: *Science Advances* 7.12 (Mar. 2021), eabf3531. ISSN: 2375-2548. DOI: 10.1126/sciadv.abf3531. URL: https://www.science.org/doi/10.1126/sciadv.abf3531 (visited on 06/19/2025).

[89] Li-Chung Cheng et al. "Measurements of multiphoton action cross sections for multiphoton microscopy". en. In: *Biomedical Optics Express* 5.10 (Oct. 2014), p. 3427. ISSN: 2156-7085, 2156-7085. DOI: 10.1364/BOE.5.003427. URL: https://opg.optica.org/boe/abstract.cfm?uri=boe-5-10-3427 (visited on 03/16/2022).

[90] Joseph R. Lakowicz. *Topics in Fluorescence Spectroscopy: Volume 5: Nonlinear and Two-Photon-Induced Fluorescence*. eng. Topics in Fluorescence Spectroscopy 5. Boston, MA: Kluwer Academic Publishers, 2002. ISBN: 978-0-306-45553-7 978-0-306-47070-7. DOI: 10.1007/b115592.

[91] M L Landsman et al. "Light-absorbing properties, stability, and spectral stabilization of indocyanine green". In: *J Appl Physiol* (Apr. 1976). DOI: 10.1152/jappl.1976.40.4.575.

[92] Martin Kauert, Martin Frenz, and Jaro Rička. "Absolute measurement of molecular two-photon absorption cross-sections using a fluorescence saturation technique". en. In: ed. by Ammasi Periasamy and Peter T. C. So. San

Jose, CA, Feb. 2006, 60891S. DOI: 10.1117/12.645576. URL: http://proceedings.spiedigitallibrary.org/proceeding.aspx?doi=10.1117/12.645576 (visited on 07/01/2025).

[93] J. J. Chapman et al. "Measurement of focusing properties for high numerical aperture optics using an automated submicron beamprofiler". en. In: *Review of Scientific Instruments* 79.9 (Sept. 2008). arXiv:0709.1004 [physics], p. 095106. ISSN: 0034-6748, 1089-7623. DOI: 10.1063/1.2991112. URL: http://arxiv.org/abs/0709.1004 (visited on 07/01/2025).

[94] Tomoyuki Horikiri et al. "Higher order coherence of exciton-polariton condensates". en. In: *Physical Review B* 81.3 (Jan. 2010). arXiv:0910.2978 [cond-mat], p. 033307. ISSN: 1098-0121, 1550-235X. DOI: 10.1103/PhysRevB.81.033307. URL: http://arxiv.org/abs/0910.2978 (visited on 07/01/2025).

[95] Giedre Astrauskaite. "Remote focusing to follow action potential transmurally in acute rabbit cardiac slices". English. PhD thesis. Glasgow: University of Glasgow, Jan. 2025.

[96] Zhen Ma et al. "Self-organizing human cardiac microchambers mediated by geometric confinement". en. In: *Nature Communications* 6.1 (July 2015), p. 7413. ISSN: 2041-1723. DOI: 10.1038/ncomms8413. URL: https://www.nature.com/articles/ncomms8413 (visited on 06/08/2026).

[97] Plansky Hoang et al. "Generation of spatial-patterned early-developing cardiac organoids using human pluripotent stem cells". en. In: *Nature Protocols* 13.4 (Apr. 2018), pp. 723–737. ISSN: 1754-2189, 1750-2799. DOI: 10.1038/nprot.2018.006. URL: https://www.nature.com/articles/nprot.2018.006 (visited on 06/08/2026).

[98] Plansky Hoang et al. "Size-Modulated Mesoderm-Endoderm Divergence and Myocardial Cavitation in Micropatterned Cardioids". en. In: *Advanced Science* 13.30 (May 2026), e15661. ISSN: 2198-3844, 2198-3844. DOI: 10.1002/advs.202515661. URL: https://advanced.onlinelibrary.wiley.com/doi/10.1002/advs.202515661 (visited on 06/08/2026).

[99] Zhongya Qin et al. "Deep tissue multi-photon imaging using adaptive optics with direct focus sensing and shaping". en. In: *Nature Biotechnology* 40.11 (Nov. 2022), pp. 1663–1671. ISSN: 1087-0156, 1546-1696. DOI: 10.1038/s41587-022-01343-w. URL: https://www.nature.com/articles/s41587-022-01343-w (visited on 09/10/2025).

[100] Seul-Gi Lee et al. "Generation of human iPSCs derived heart organoids structurally and functionally similar to heart". en. In: *Biomaterials* 290 (Nov. 2022), p. 121860. ISSN: 01429612. DOI: 10.1016/j.biomaterials.2022.121860. URL: https://linkinghub.elsevier.com/retrieve/pii/S0142961222005002 (visited on 09/10/2025).

[101] Yoshimasa Suzuki et al. "Scattering reduced imaging of spheroids via refractive index estimation and shift-variant deconvolution". en. In: *Biomedical Optics Express* 16.8 (Aug. 2025), p. 3437. ISSN: 2156-7085, 2156-7085. DOI: 10.1364/BOE.569674. URL: https://opg.optica.org/abstract.cfm?URI=boe-16-8-3437 (visited on 11/16/2025).

[102] Herve Hugonnet et al. "Pupil phase series: a fast, accurate, and energy-conserving model for forward and inverse light scattering in thick biological samples". en. In: *Optics Express* 33.16 (Aug. 2025), p. 34255. ISSN: 1094-4087. DOI: 10.1364/OE.568019. URL: https://opg.optica.org/abstract.cfm?URI=oe-33-16-34255 (visited on 06/08/2026).

[103] Huai-Ching Hsieh et al. "Imaging 3D cell cultures with optical microscopy". en. In: *Nature Methods* 22.6 (June 2025), pp. 1167–1190. ISSN: 1548-7091, 1548-7105. DOI: 10.1038/s41592-025-02647-w. URL: https://www.nature.com/articles/s41592-025-02647-w (visited on 11/16/2025).

[104] Tingting Yu et al. "On-chip clearing for live imaging of 3D cell cultures". en. In: *Biomedical Optics Express* 14.6 (June 2023), p. 3003. ISSN: 2156-7085, 2156-7085. DOI: 10.1364/BOE.489219. URL: https://opg.optica.org/abstract.cfm?URI=boe-14-6-3003 (visited on 11/16/2025).

[105] Sarah De Beuckeleer et al. "An agarose fluidic chip for high-throughput *in toto* organoid imaging". en. In: *Lab on a Chip* 25.2 (2025), pp. 235–252. ISSN: 1473-0197, 1473-0189. DOI: 10.1039/D4LC00459K. URL: https://xlink.rsc.org/?DOI=D4LC00459K (visited on 11/16/2025).

A: OPA Layout

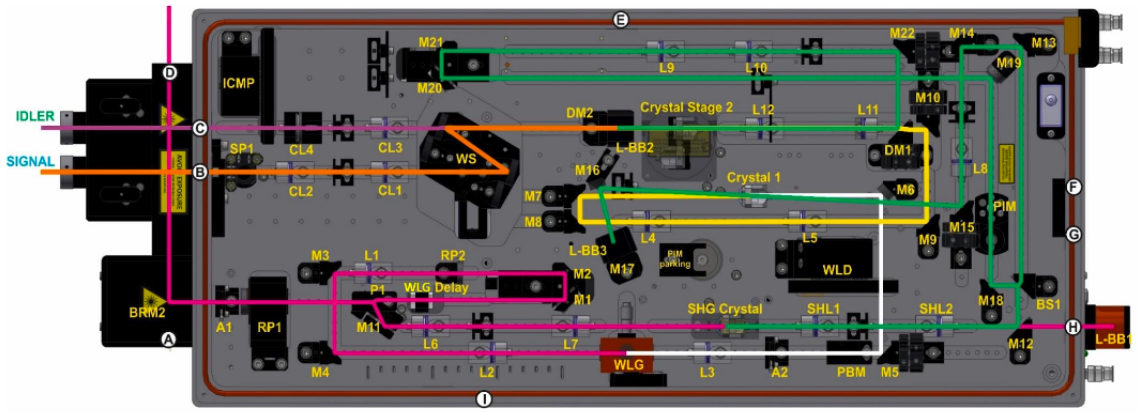

Figure F.65: Schematic layout of the Orpheus-F optical parametric amplifier (OPA) from Light Conversion. A – iris aperture, BB – beam blocker, BS – beam splitter, BRM – beam routing mirror, CL – collimating lens, Crystal 1 – 1st amplification stage crystal, Crystal Stage 2 – 2nd amplification stage crystal, DM – dichroic mirror, ICMP – Idler compressor, L – lens, M – mirror, P – polariser, PBM – pump blocking mirror, PIM – pump interception mirror, RP – rotator of polarization, SHG Crystal – harmonic generation crystal, SP – spectrometer mirror, WLG Delay – temporal delay compensator, WLD – temporal dispersion medium, WLG – white light generation substrate, WS – wavelength separator

B Optical Losses

Following are manufacturers data sheets for the optical components used in the calculation of optical losses in Chapter 4.5.

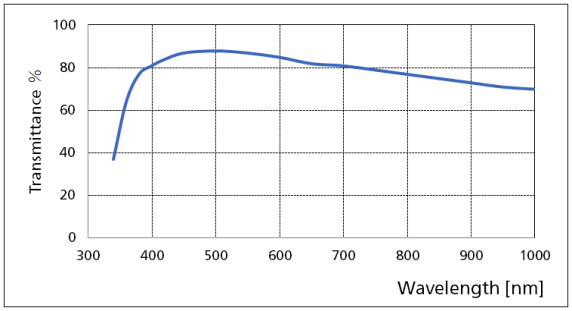

Figure F.66: Transmission of Nikon N40XW-PF

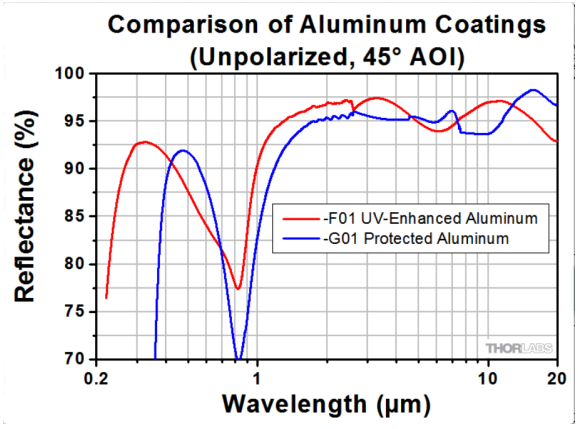

Figure F.67: Silver Mirror Reflection at 45°

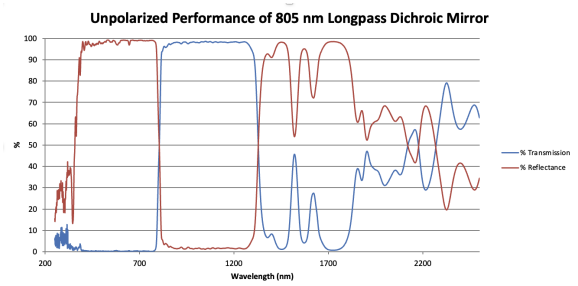

Figure F.68: D_1 Loss

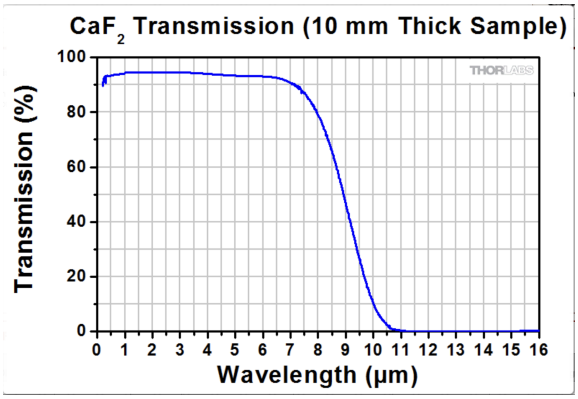

Figure F.69: Uncoated Lens Loss

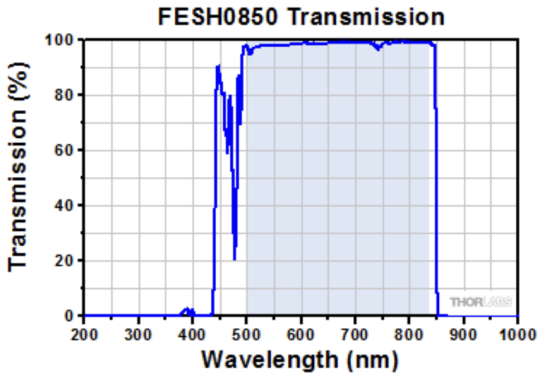

Figure F.70: F_0 Losses

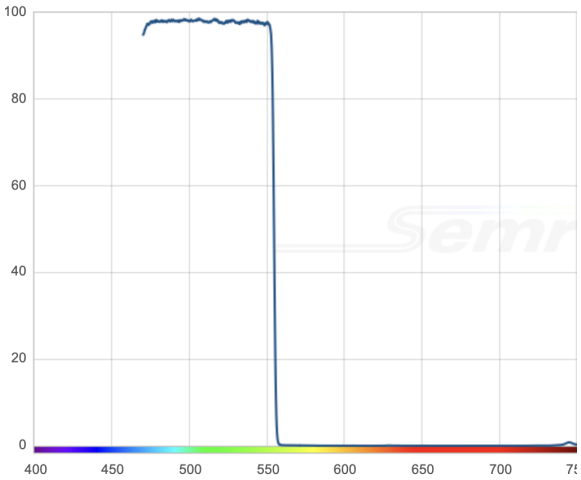

Figure F.71: Dichroic 1 losses

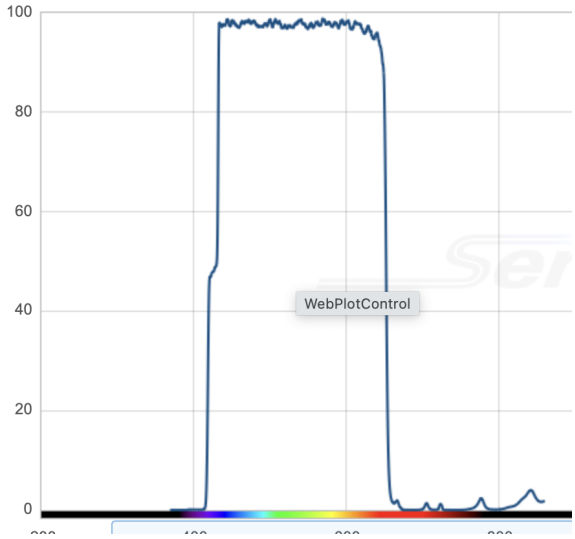

Figure F.72: Dichroic 2 losses

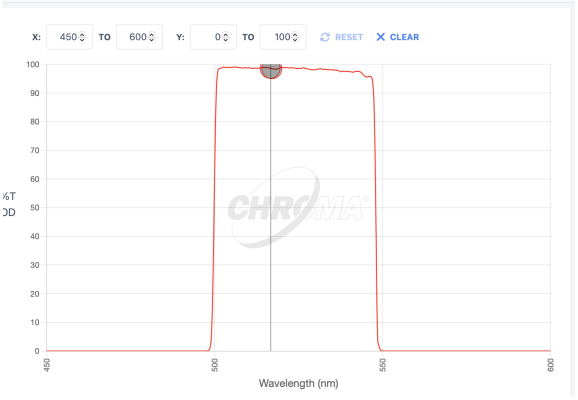

Figure F.73: Filter 1 Losses

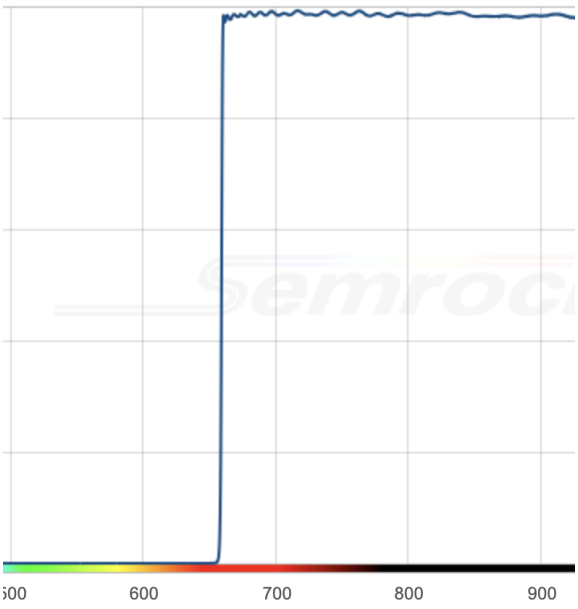

Figure F.74: Filter 3 Losses